



SCUOLA DOTTORALE
IN SCIENZE
MATEMATICHE E FISICHE
XXVI CICLO

Department of Physics

***Dielectric measurements of
Europa's and Mars' ice shell:
implication for radar exploration***

By

Barbara Cosciotti

Tutor

Dott.ssa Elena Pettinelli

Coordinatore:

Prof. Roberto Raimondi

TABLE OF CONTENTS

TABLE OF CONTENTS	3
LIST OF FIGURE	8
Acknowledgements	17
<u>I. INTRODUCTION</u>	19
1.1 MOTIVATION AND GOALS	21
1.2 BACKGROUND	22
<u>II. EVOLUTION AND INTERIOR OF ICY GALILEAN SATELLITES</u>	25
2.1 EVOLUTION OF SATELLITES INTERIORS	25
2.1.1 INTRODUCTION	25
2.1.2 SATELLITES IN RESONANCE: STRONG THERMAL/ORBITAL-DYNAMICAL COUPLING	27
2.1.3 IO, EUROPA, GANYMEDE: THE LAPLACE RESONANCE	28
2.2 GEOPHYSICS STRUCTURE: EUROPA AND GANYMEDE	30
2.2.1 EUROPA	30
2.2.2 GANYMEDE	36
2.3 COMPOSITION OF THE UPPER LAYERS OF THE ICY GALILEAN SATELLITES	40
2.4 GEOLOGY: SURFACE APPEARANCE AND PROCESSES	44
2.4.1 EUROPA	44
2.4.2 GANYMEDE	48
<u>III. MARS</u>	52

3.1	BACKGROUND	52
3.2	GENERAL CHARACTERISTICS	52
3.3	VOLCANISM	54
3.4	TECTONICS	56
3.5	WEATHER AND CLIMATE	59
3.6	WATER, ICE, AND PERMAFROST	63
3.7	MISSIONS	65
3.8	THE ATMOSPHERIC AND SURFACE TEMPERATURE	68
3.9	THE GROUND ICE IN THE REGOLITH	73
3.10	THE PRESENT CLIMATE ON MARS	75
3.10.1	GLOBAL CIRCULATION	75
3.10.2	STABILITY OF H ₂ O	78
3.10.3	POLAR LAYERED DEPOSITS	80
3.10.4	DUST CYCLE	82
3.11	TERRESTRIAL ANALOGUES FOR MARTIAN GROUND ICE	87
IV.	<u>DIELECTRIC PROPERTIES OF ICE MATERIALS</u>	89
4.1	INTRODUCTION	89
4.2	THEORETICAL RECALLS	90
4.3	WAVE PROPAGATION	98
4.4	DIELECTRIC PROPERTIES OF PURE WATER ICE	100
4.5	EFFECT OF IMPURITY IN WATER ICE	106
4.6	STATIC CONDUCTIVITY	108
4.7	HIGH FREQUENCIES CONDUCTIVITY	109
4.8	DIELECTRIC RESPONSE UP TO 1 GHz (IMAGINARY, REAL PART VS IMPURITY)	113

4.9	CONDUCTIVITY	114
4.10	REAL PART	115
4.11	ANISOTROPY	116
4.12	ROCK IMPURITIES	117
4.13	DENSITY	119
<u>V.</u>	<u>EXPERIMENTAL SET-UP</u>	<u>121</u>
5.1	LABORATORY MEASUREMENTS: THE EXISTING FACILITY	121
5.2	LIQUID NITROGEN CRYOSTAT	122
5.3	LCR METERS: AGILENT HP4284A/HP4285A	126
5.4	ZEROING CALIBRATION	128
5.5	MEASUREMENT OF THE ELECTRIC PERMITTIVITY	129
5.5.1	THEORY OF CAPACITIVE CELL DIELECTRIC SPECTROSCOPY	132
<u>VI.</u>	<u>DIELECTRIC MEASUREMENTS AND RADAR ATTENUATION</u>	
	<u>ESTIMATION OF ICE/BASALT SAND MIXTURES AS MARTIAN POLAR</u>	
	<u>CAPS ANALOGUES.</u>	<u>136</u>
6.1	ABSTRACT	136
6.2	INTRODUCTION	137
6.3	METHODS	140
6.4	RESULTS AND DISCUSSIONS	143
6.4.1	PURE WATER ICE	143
6.4.2	DRY BASALTIC SAND	146
6.4.3	11.3% AND 43% ICE/BASALT SAND MIXTURES	148
6.5	FINAL REMARKS	153

VII. DIELECTRIC MEASUREMENTS OF SALINE ICES UP TO 200K 155

7.1 DIELECTRIC MEASUREMENTS OF $MgSO_4 \cdot 7H_2O$-ICE AT DIFFERENT TEMPERATURES AND CONCENTRATIONS	156
7.2 DIELECTRIC MEASUREMENTS OF Na_2SO_4-ICE AT DIFFERENT TEMPERATURES AND DIFFERENT CONCENTRATIONS	161
7.3 FIT WITH DEBYE MODEL	165
7.4 ATTENUATION IN DB/KM FOR DIFFERENT SALT CONCENTRATION IN ICE AND FIT UP TO 50 MHz	166

**VIII. DIELECTRIC MEASUREMENTS OF SALINE ICES UP TO 100K
168**

8.1 INTRODUCTION	168
8.2 EUTECTIC FREEZE CRYSTALLIZATION	169
8.3 DIELECTRIC MEASUREMENTS OF $MgSO_4$-ICE AND Na_2SO_4-ICE AT EUTECTIC CONCENTRATION	170

**IX. THERMAL MODELS AND ELECTROMAGNETIC ATTENUATION
175**

9.1 EUROPA - INTERIOR STRUCTURE AND DYNAMICS OF THE ICE SHELL	175
9.2 GANYMEDE - INTERIOR STRUCTURE OF THE ICE SHELL	179
9.3 THERMAL CONDUCTIVITY	180
9.3.1 THERMAL CONDUCTIVITY OF ICE I_H	181
9.3.2 THERMAL CONDUCTIVITY OF SALTS	185
9.3.3 THERMAL CONDUCTIVITY OF AMMONIA	187
9.3.4 THERMAL CONDUCTIVITY OF DUST	188

9.3.5	THERMAL CONDUCTIVITY OF CARBON DIOXIDE	188
X.	CONCLUSIONS	190
10.1	FUTURE WORKS	193
	BIBLIOGRAPHY	197

LIST OF FIGURE

- Figure I** SHARAD Radargram of north polar plateau of Mars taken at an altitude of 300 km. The upper panel shows SHARAD data degraded in resolution from 10 m in ice to the RIME resolution of 30 m in ice. Layers seen on Mars are likely due to variations in insoluble impurities like dust. The lower panel is shaded relief topography from the Mars Orbiter Laser Altimeter (MOLA), with the nadir ground track shown as a white line. Numerous features are visible in radar sounding data at this resolution, as noted by the arrows. Maximum penetration in this observation is 2 km, at the far left. 20
- Figure II** A portrait of the icy satellites of Jupiter, with their size shown to scale. At the right is Callisto, the farthest from Jupiter, with its dark silicate veneer. With minimal endogenic activity, this surface shows at this scale the record of cratering bombardment. To the left of Callisto, at the center of the montage, is Ganymede, with 1/3 of its surface similar to Callisto's, and 2/3 consisting of younger, bright grooved terrain, strongly modified by extensional tectonic processing. To the left of Ganymede is Europa, with global scale lineaments testifying to a complex and active tectonic history, and dark splotches marking thermally driven chaotic terrain. Craters are few on Europa, indicating that this surface has continually been reprocessed by tectonics and chaos formation until very recently and may still be active. One crater, Pwyll, has a large system of bright ejecta rays, evident in this image. The tiny, elongated satellite Amalthea at the far left is the closest to Jupiter and the smallest of the group. Relatively recently recognized to be icy, Amalthea challenges models of the origin of the Jupiter system. 25
- Figure III** Two examples of resonances in the outer solar system involving internal heating of satellites. Rotational energy of the primary planet and angular momentum are transferred to the innermost satellite due to tidal torques. Because of the resonance coupling, energy and angular momentum are distributed among the satellites locked in resonance. Part of the energy is dissipated as heat in the satellites' interiors due to tidal flexing. This affects mainly the inner satellites close to the primary, in the first case Io and, to a lesser extent, Europa, and in the second example Enceladus (sizes and distances not to scale)..... 27

Figure IV The tide on Europa (at the bottom) is shown schematically at four points (from left to right) in its orbit. The black bulges represent Europa's stretched shape. Jupiter is the small circle (obviously the giant planet is not to scale) near the top. The frame of reference used here is locked to the body of Europa, so Jupiter always remains on the same side. The eccentricity of the orbit produces small variations in the distance and direction of Jupiter relative to the body of Europa, which appears in this reference frame as epicycl motion. The size and orientation of the bulges qualitatively indicate the variation in the tidal distortion of the body. 33

Figure V Cycloidal crack patterns (chains of arcs), are ubiquitous on Europa, usually displayed in the form of double ridges lining the sides of the cracks. This image from the Voyager mission in 1979 shows beautiful, but typical, examples of cycloidal ridges, including Cilicia, Delphi and Sidon Flexus. Arcs are typically about 100 km long, and many cycloids comprise a dozen arcs or more. Older cycloids have been sliced and diced by subsequent tectonic and thermal processing, and thus may only appear as short arcuate features or isolated cusps. 34

Figure VI The bright grooved terrain on Ganymede contrasts with the dark ancient terrain in this much high resolution. The greater crater density on the dark terrain is evident, as is the predominantly tectonic character of the brighter terrain. This region is about 660 by 520 km in size with resolution about 1 km per pixel (JPL Image PIA 1617). 39

Figure VII A 300 km wide region on the surface of Europa at the intersection of two of the global-scale lineaments (which form the X just to the upper right of center in the disk of Europa shown in Figure II). The global lineaments here resolve into double dark lines called 'triple bands'. The dark area below the intersection is Conamara Chaos. The vertical white streaks are rays of ejecta from an impact crater 1000 km to the south. 45

Figure VIII The Conamara Chaos region on Europa at much higher resolution (~180 m/pixel) than in Figure XI, and with more advantageous lighting, shows morphological detail of the chaotic terrain, which fills is apparent. The double lines that dominate their appearance in Figure XI, are here only a diffuse darkening along the margins of these ridge systems. 46

Figure IX A mosaic of high-resolution images (54 m/pixel) within the Conamara Chaos region of Europa (Figure X). Within a lumpy matrix, rafts of displaced crust display fragments of the previous tectonic terrain. Subsequent to the formation of the chaotic

terrain, probably by melt through from below, the fluid matrix refroze and new double ridges have formed across the area and begun the process of tectonic resurfacing..... 46

Figure X The dark regions on Ganymede contain sets of furrows, which are often parallel to the borders with the bright grooved terrain as seem here. These dark-region furrows may have formed by surface extension, an incipient version of the kind of tectonic processing that produced the bright grooved terrain. Furrows in the dark regions also often display concentric patterns suggesting that they formed as rings around impact basins, similar to those of Valhalla on Callisto). In the foreground (lower left) is typical bright grooved terrain. Craters of various morphologies are displayed in this area. The area shown is about 450 km wide in a Voyager image (NASA/JPL PIA 2281)..... 48

Figure XI High-resolution image of bright, grooved terrain on Ganymede showing details of the extensional tectonics. This image, taken by the Galileo spacecraft, shows an area 35 km wide at a resolution of 74 m/pixel (NASA/JPL PIA 0277). 49

Figure XII North polar stratigraphy from HiRISE imaging and SHARAD radar. (a) HiRISE false-color image PSP 008936 2660, at 144°E 86°N, showing typical exposures of layers in trough (downhill, left) also covered by radargram. (b) Radargram from SHARAD orbit 5192 with associated ground track. Time-to-depth conversion assumed a subsurface permittivity of three. Reproduced from Phillips et al. (2008) with permission from AAAS. Location of trough shown in (a) is indicated. (c) HiRISE false-color image PSP 001593 2635, at 119°E 83.4°N, showing scarp with transition in layering from smooth (i), to polygonally fractured (ii), to the sand-rich basal unit (iii). 60

Figure XIII Topographic maps of Mars based on data from the Mars Orbiter Laser Altimeter (MOLA). The colour bar indicates the topographic height in kilometers above the areoid (the equipotential surface which is equivalent to the “mean sea level” on Earth). The latitude and longitude refer to an areocentric coordinate convention with east longitude positive. Image credit: MOLA Science Team. Lower panel: Mercator projection map covering the latitudes between 70°S (indicated by minus sign) and 70°N. The Martian dichotomy is clearly seen with the distinct division between the low-lying smooth young plains of the northern hemisphere and the cratered highlands in the South. Prominent features seen are the deep canyon system Valles Marineris (10-20°S, 265-325°E); the impact basin Hellas (45°S, 70°E); and the volcanic highlands Tharsis (equator, 220-300°E) with the largest volcano in the Solar System Olympus Mons to the northwest (18°N, 225°E). Upper right: Polar stereographic map centered around the

north pole. The light blue and green area is the north polar ice cap, which lies several km higher than the surrounding smooth terrain. The north polar cap is cut through by a deep gorge named Chasma Boreale. Around the edges of the polar cap a spiral pattern is seen which consists of flat plateaus and steeper scarps. The center of the ice cap is very smooth and almost devoid of craters indicating a very young surface. Upper left: Polar stereographic map centered around the south pole. The south polar ice cap and the polar layered deposits are seen as the red area surrounded by orange. Note that the spiral structures close to the pole are similar to the features on the north polar cap. The grey area indicates insufficient data. 61

Figure XIV The Mars Orbiter Camera (MOC) has since 1999 daily recorded images of the weather patterns of the planet. The Figure shows six different views composed of 24 images of Mars acquired on February 14, 2003, when it was in the middle of the summer on the northern hemisphere. Water ice clouds can be seen around the equator and the lower latitudes, and orographically induced water ice clouds can be seen hanging over the highest points in the topography, which are the large volcanoes in the Tharsis and Elysium regions (upper left and center and lower right). The north polar ice cap is fully exposed in the northern hemisphere, whereas the southern polar regions are covered by a seasonal layer of CO₂ frost. The frost extends itself furthest to the north in the Hellas Basin, where the lower topography and therefore higher atmospheric pressure in the basin allows the CO₂ to freeze at slightly higher temperatures than elsewhere in the southern hemisphere. Image credit: NASA/JPL/Malin Space Science Systems. 62

Figure XV Left: The north polar ice cap in the northern summer time. The white areas are residual water ice that remains through the summer season. The nearly circular band of dark material surrounding the cap consists mainly of sand dunes formed and shaped by wind. The north polar cap is approximately 1100 kilometers across. 63

Figure XVI Layers seen in a slope of the north polar ice cap at 81.5°N in late northern spring. The image is taken by the Mars Orbiter Camera (MOC) and covers an area of approximately 3 km in width. The layers consist of H₂O and CO₂ ice and dust. The brightest areas in the image are covered by frost. Image credit: NASA/JPL/Malin Space Science Systems. 65

Figure XVII Illustration of the seasonal variation in the zonally averaged surface pressure relative to the annual average as a function of latitude (horizontal axis) and time of the year (see legend for season numbers). 69

Figure XVIII: Atmospheric pressure data for the Viking dust scenario from MCD. The horizontal axis represents the latitude [degrees] and the vertical axis the altitude above the Martian surface [km]; note that the vertical scale is non-linear. The colour bar shows the atmospheric pressure [Pa]. The number above each plot indicates the season number, each of which lasts 30_Ls. The white contour lines represent pressures of 0.01, 0.1, 1, 10, and 100 Pa (pressures decreasing with altitude). 70

Figure XIX: Zonally averaged annual mean atmospheric temperature data from the MCD, the colour bar indicates the temperature in [K]. The horizontal axis shows the latitude [$^{\circ}$] and the vertical axis the altitude [km] on a non-linear scale..... 71

Figure XX: Zonally averaged diurnal mean atmospheric temperature data from the MCD, the colour bar indicates the temperature in [K]. The horizontal axis shows the latitude [$^{\circ}$] and the vertical axis the altitude [km] on a non-linear scale..... 72

Figure XXI: Zonally averaged diurnal mean surface temperature data from MCD, the colour bar indicates the temperature in [K]. The horizontal axis show the season number and the vertical axis the latitude [$^{\circ}$]. 73

Figure XXII Ground Ice percentages from the MGS Neutron Spectrometer. The colour bars show the values of ground ice estimated from water-equivalent-hydrogen in mass-%. Notice the different scales for the polar- (upper panel) and low-latitude plots (lower panel). For the latter two, the scale is saturated for values greater than 10%. The globes each show a part of the Martian surface. UL: The north pole region down to equator. The 0°meridian is pointing from the pole to the left. UR: The south pole region down to equator. The 0°meridian is pointing from the pole to the left. LL: The eastern hemisphere. The 0°meridian is located along the left edge of the globe. LR: The western hemisphere. The 0° meridian is located along the right edge of the globe..... 74

Figure XXIII: This series of pictures captures the seasonal retreat of Mars' north polar cap. (NASA)..... 76

Figure XXIV:A dust storm on Mars (top) and on Earth (bottom). Even though there are many differences between the two atmospheres, similarities in the dynamics can be observed.(NASA/JPL/MSSS) 78

Figure XXV: Phase diagram of H₂O showing the dependency of pressure and temperature on H₂O. The typical regions of pressure and temperature for Earth, Mars and Venus is

shown. It can be seen that under present Martian pressure conditions, water is usually only stable in solid or in vapor form..... 79

Figure XXVI: Left: The North polar layered deposits in October 2006 as seen from the Mars Color Imager instrument aboard NASA's MRO. (NASA/JPL/MSSS). **Right:** The residual CO₂ ice on the South polar layered deposits (NASA/JPL) 80

Figure XXVII: Global Dust Storm seen from the Hubble Space Telescope. Within 3 months, the storm extended from pole to pole. (NASA) 83

Figure XXVIII: Dust devil on the floor of Gusev crater, taken by the Spirit Navcam. This dust devil is about 1 km from the rover and is estimated to be at least 95 m high. (NASA/JPL)..... 84

Figure XXIX Dust devil streaks on the surface around (5.3°S, 343°W) as observed by the MGS MOC camera. The picture is about 3 km across. (NASA/JPL/MSSS) 85

Figure XXX: Ice table in Beacon Valley, Antarctica. The ice is covered by 15 cm of sandy soil. From Mellon et al. (2004). 87

Figure XXXI The time response, in a generic dielectric, of the various polarization processes when a step function excitation field E is applied..... 94

Figure XXXII Real and imaginary parts of the effective permittivity vs. frequency 96

Figure XXXIII The behaviour of the effective conductivity, real and imaginary part of permittivity in function of temperature and frequency..... 98

Figure XXXIV 101

Figure XXXV The real and imaginary parts of the permittivity for ice, ϵ'_{ICE} and ϵ''_{ICE} and for water, ϵ'_{WATER} and ϵ''_{WATER} 105

Figure XXXVI Scheme of Cryostat 122

Figure XXXVII Scheme of capacitive cell 124

Figure XXXVIII The capacitive cell 124

Figure XXXIX Left: Equivalent electric circuit of a LCR meter; **Right** Scheme of capacitive cell..... 125

Figure XL Equivalent electric circuit of a LCR meter 126

Figure XLI Vectorial currents diagram in a capacitive cell 130

Figure XLII 132

Figure XLIII Air Capacitance C_0 134

Figure XLIV Loss Tangent 134

Figure XLV Imaginary Part of permittivity measured on pure water ice 143

Figure XLVI Real Part of permittivity measured on pure water ice.....	143
Figure XLVII Attenuation on pure water ice	144
Figure XLVIII Real Part of permittivity measured on dry sand	146
Figure XLIX Imaginary Part of permittivity measured on dry sand.....	147
Figure L Attenuation measured on dry sand	147
Figure LI Real part of permittivity of the 11.3% and ice/ ice/grains mixture at different temperatures	148
Figure LII Real part of permittivity of the 43% ice/ ice/grains mixture at different temperatures	148
Figure LIII Imaginary part of permittivity measured on 11.3% ice/grains mixture at different temperatures.....	149
Figure LIV Imaginary part of permittivity measured on 43% ice/grains mixture at different temperatures.....	150
Figure LV Attenuation measured on 11.3% ice/grains mixture at different temperatures.	150
Figure LVI Attenuation measured on 43% ice/grains mixture at different temperatures	151
Figure LVII Comparison between measurements performed on the 11.3% mixture with the HP4285A LCR meter (75kHz-30MHz) and the asymptotic curve calculated using equation (LIII).....	152
Figure LVIII Comparison between measurements of attenuation performed on the different ice/basalt sand mixture with the HP4285A LCR meter (75kHz-30MHz) and the asymptotic curve calculated using equation (LIII).....	154
Figure LIX the capacitive cell in the polystyrene box containing CO ₂ -ice	155
Figure LX Real part of permittivity at six different temperatures of: a) Pure ice, b) C1, c) C4, d) C7.....	157
Figure LXI Imaginary part of permittivity at six different temperatures of: a) Pure ice, b) C1, c) C4, d) C7	158
Figure LXII Real part of permittivity at five different concentrations at four different temperatures	159
Figure LXIII Imaginary part of permittivity at five different concentrations at four different temperatures.....	160

Figure LXIV Real part of permittivity at six different temperatures of: a) Pure ice, b) C1, c) C4, d) C7	161
Figure LXV Imaginary part of permittivity at six different temperatures of: a) Pure ice, b) C1, c) C4, d) C7	162
Figure LXVI Real part of permittivity at five different concentrations at four different temperatures	163
Figure LXVII Imaginary part of permittivity at five different concentrations at four different temperatures.....	164
Figure LXVIII Fit with Debye Model of real part of permittivity at C ₁ concentration.....	165
Figure LXIX Electromagnetic Attenuation of both salts at C1 concentration.....	166
Figure LXX Fit of Attenuation up to 50 MHz of both salts at lower temperature of about 200 K.....	167
Figure LXXI Phase diagram of a binary salt-water mixture	169
Figure LXXII a) Real part of permittivity, b)Imaginary part, c) Conductivity	172
Figure LXXIII a) Real part of permittivity, b)Imaginary part, c) Attenuation.....	174
Figure LXXIV Structures and temperature profiles for two possible configurations of the ice shell of Europa. The heat generated in the interior of the planet might be shed by simple conduction through a relatively thin ice shell directly overlying a subsurface ocean (A), or transported equally well through a much thicker ice shell containing of an actively convecting layer (B). Because of the large viscosity near the surface, the ice shell in B develops a stagnant lid at the surface; the convective motions are confined to a sublayer of the ice shell. The states (A) and (B) could have very similar heat fluxes [Mitri and Showman, 2005].....	176
Figure LXXV Temperature-dependent thermal conductivity fit obtained by different authors for ice I _h	183
Figure LXXVI Effect of the thermal conductivity model on the thermal profile for a pure conductive lid.....	184
Figure LXXVII Thermal profile of Europa considering ice I _h , epsomite and the eutectic mixture of ice and epsomite [Prieto-Balesteros and Kargel, 2005].....	186
Figure LXXVIII k(T) of epsomite and mirabilite [Prieto-Balesteros and Kargel, 2005] compared to the ice I _h	186
Figure LXXIX Scheme of implemented experimental setup	194
Figure LXXX Plume at 10 km.....	195

Acknowledgements

I would first like to thank my tutor, Elena Pettinelli, for leading me through my adventures in graduate school, for offering sage perspectives on academia and for sharing his enthusiasm for solving the mysteries of the natural world. Ed gave me an excellent foundation in Dielectric Spettroscopy, taught me scientific humility and the value of solving small problems first.

I also owe an incredible amount to Prof. Francesco Bella, who taught me the value of toughness and professionalism; he took me further than I ever thought possible and I hope to honor his vision.

Giuliano Vannaroni taught me precision in many senses, led my first laboratory experience and also suggested the love for experimental physics that changed the course of my graduate career.

Many collaborators inside of the University of Roma Tre also supported my graduate studies and helped clarify the broader value of my research, particularly Elisabetta, Sebastian, Federico, Carlotta, Matteo, and the laboratory technicians: Francesco and Claudio.

I would also like to thank my mother and father for their unwavering support of my plans to keep moving in science, despite the many difficulties.

Francesca and Valter for their unfailing presence, they provided the drive and emotional foundation that has sent my mind and body to many remote places.

There are many graduate students whose friendship I cherish; their support during my graduate career has been invaluable to my soul and has led to many happy memories of my time in Mathematics and Physics Department: Francesca, Alessio and Irene, reserve special mention as such friends.

A final thanks to Emanuela and Alessandra: the ONLY FRIENDS!

I. INTRODUCTION

The aim of this thesis is the development and application of non-invasive electromagnetic techniques designed to estimate the electromagnetic parameters of materials of geophysical interest fundamental to the future study of planetary subsoils. In particular, the work has been focused on the study of the behavior of impure ice, which is of interest both in natural terrestrial and planetary precisely.

The first recognition of the Jupiter system by the Voyager spacecraft, suggested the possibility of an ocean of liquid water beneath the ice shell of two of Jupiter's moons, Ganymede and Europa. Recent high-resolution images of Ganymede by the Galileo spacecraft are consistent with this interpretation, and suggest that in some locations, the liquid water may lie a few kilometers deep into the ground in Europe.

JUICE - JUpiter ICy moons Explorer - is the first large-class mission in ESA's Cosmic Vision 2015-2025 program. Planned for launch in 2022 and arrival at Jupiter in 2030, it will spend at least three years making detailed observations of the giant gaseous planet Jupiter and three of its largest moons, Ganymede, Callisto and Europa.

JUICE mission will investigate the potentially habitable zones in the Galilean icy satellites: Ganymede, Europa and Callisto. The overall science objectives of the JUICE mission for the icy satellites are to (i) characterize Ganymede as a planetary object and possible habitat, (ii) explore Europa's recently active zones, and (iii) study Callisto as a remnant of the early Jovian system. The proposed *Radar for Icy Moon Exploration* (RIME) is a radar sounder (referred to as Ice Penetrating

INTRODUCTION

Radar (IPR in the JUICE AO documents) optimized for the penetration of the icy moons, Ganymede, Europa and Callisto, up to a depth of 9 km. Because of the unique capability of investigating subsurface structures remotely, radar sounders have been used to investigate extraterrestrial bodies such as Mars and the Moon (Picardi et al., et al.). Currently there are two such radars at Mars. The Mars Advanced Radar for Subsurface and Ionosphere Sounding (MARSIS, et al.) is an orbital radar sounder on-board ESA's Mars Express S/C that is optimized for deep penetration of the Martian (SHARAD, et al.) subsurface. The SHallow RADar (SHARAD; Seu et al., 2007) on-board NASA's Mars Reconnaissance Orbiter is optimized for high vertical resolution with shallow penetration of Mars. Figure I presents a radargram acquired by SHARAD at Planum Boreum (north polar plateau) of Mars.

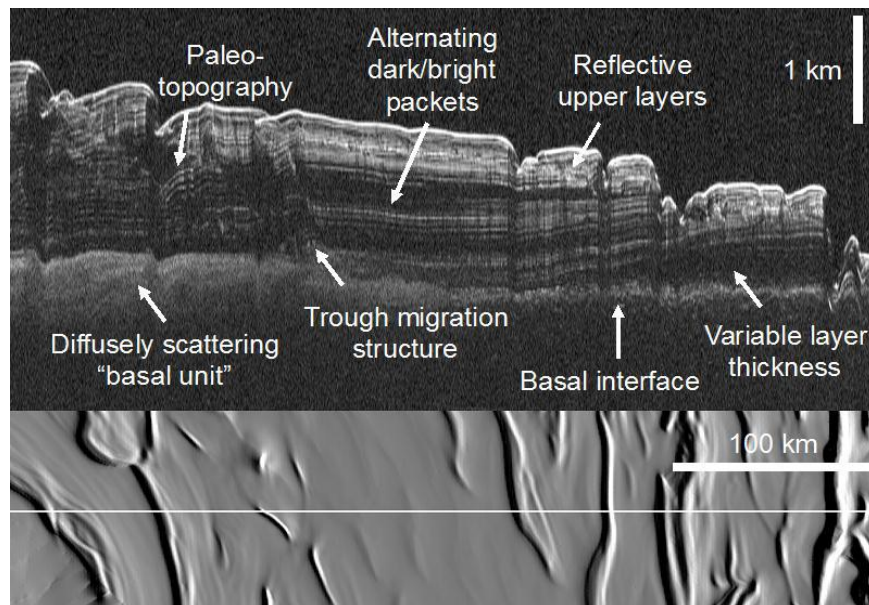


Figure I SHARAD Radargram of north polar plateau of Mars taken at an altitude of 300 km. The upper panel shows SHARAD data degraded in resolution from 10 m in ice to the RIME resolution of 30 m in ice. Layers seen on Mars are likely due to variations in insoluble impurities like dust. The lower panel is shaded relief topography from the Mars Orbiter Laser Altimeter (MOLA), with the nadir ground track shown as a white line. Numerous features are visible in radar sounding data at this resolution, as noted by the arrows. Maximum penetration in this observation is 2 km, at the far left.

Therefore, the use of such techniques could demonstrate the presence of an ocean water in the subsurface of both satellites. The achievement of this objective depends on the electromagnetic properties of the ice layer, or by the presence of any impurities in the ice itself and the temperature gradient, as well as by the wavelength of the radar. The proposed RIME instrument will exploit the substantial heritage developed in the two successful planetary radar missions on Mars by acquiring for the first time direct measurements of the subsurface of the Galilean icy moons. The JUICE mission is unique as it is the first mission to Jupiter and the outer Solar System that includes instrumentation capable of performing direct subsurface measurements. Due to its distinctive capabilities, RIME can address a large number of fundamental and unique science objectives.

1.1 Motivation and goals

The main goal of this dissertation is the electromagnetic characterization of Europa's and Martian analogues for estimating the performance of the radar sounders used to investigate the subsoils. It has provided an intense laboratory work aimed at evaluating the effects of scattering and the electromagnetic properties of ice mixtures, simulating the subsurface of Mars and Europa, on the attenuation of the radar signal. Such a study is critical for the determination of specific RIME and to determine its performance in terms of maximum penetration depth, spatial resolution, and detection capability of interfaces to weak electromagnetic contrast.

In the first part of the dissertation, my work is focused on the dielectric parameters of several Martian icy mixture simulants. I performed the

INTRODUCTION

measurements of the complex permittivity, in a wide range of temperature (100K-250K) and frequency (10KHz-30MHz), on pure water ice, dry basalt sand and ice/basalt mixtures with different sand volume fractions.

Instead in the second part I focus on the determination of complex permittivity, conductivity and consequently electromagnetic attenuation as function of frequency (10KHz-30MHz) and of temperature (100K-250K); in particular I carried out measurements of dielectric properties of **pure** and **saline** ice (mixing $\text{MgSO}_4 \cdot 7\text{H}_2\text{O}$ or $\text{Na}_2\text{SO}_4 \cdot 10\text{H}_2\text{O}$ with bidistilled water) both in time and frequency domain.

1.2 Background

There are strong reasons for a continued focus on the icy satellites. I have seen that all three icy Galilean satellites probably have liquid water layers, and one, Europa, almost certainly has an ocean just below the surface. Naturally, liquid water raises the possibility of extraterrestrial life. On Ganymede and Callisto, and on Europa as well if the ice is so thick that the ocean is isolated below, life would face an inhospitable setting.

The ecosystem would be isolated from both oxygen (Gaidos, et al., 1999) and from sunlight. The possibility of life would require alternative biochemistries. Models based on hypothetical metabolic chemical pathways, such as methanogenesis, have been developed assuming hydrothermal activity and the delivery of plausible endogenic oxidants into the ocean (McCollom, 1999), (Zolotov, et al., 2003 2004). Even with the freedom to model deep-sea conditions unconstrained by observations, some theoretical considerations have suggested that life

INTRODUCTION

would be very limited if it could exist at all (Chyba, 2000), (Chyba, et al., 2001).

On Europa, however, the surface geology suggests linkages between the ocean and the surface, possibly including dynamic flow of liquid to (or close to) the surface. Equally crucial is that the surface of the ice is bombarded by energetic charged particles from Jupiter's magnetosphere e.g. (Cooper, et al., 2001). Organisms within a few centimeters of the surface would be killed by the radiation, but the radiolysis would likely produce a suite of chemical products including oxidants (such as oxygen and hydrogen peroxide) that likely get mixed into the ice e.g (Chyba, et al., 2001).

Cometary material landing on the surface may also deposit a suite of organic and other substances, potentially useful for life. Moreover, enough sunlight could penetrate a few meters to drive subsurface photosynthesis. Relatively warm sea water periodically reaching the surface could conceivably support a rich ecology, both in the crust and in the ocean. A biosphere on Europa, if any, probably extends from deep in the ocean up to within a few centimeters of the surface.

A critical issue for life in the ocean is the rate of delivery of oxidants from the surface. Estimates of the rate depend on the thickness of the oxygenated layer near the surface, the concentration of oxidants within it, and the rate at which the layer finds its way into the ocean. (Chyba, et al., 2001) identified the importance of 'gardening' by small impactors to bury the forming oxidants (Hand, et al., 2007) refined that model by incorporating laboratory data on the radiolysis process and using an improved gardening model. Assuming a characteristic frequency with which the oxygenated layer gets deposited in the ocean, by unspecified means, they calculated the average delivery rate of oxidants into the

INTRODUCTION

ocean. With a frequency assumed comparable to the crater age of Europa's surface, the delivery rate would be sufficient for a flourishing marine ecosystem. When actual geological resurfacing processes are taken into account, delivery rates may be adequate to have saturated the ocean with the radiolytic oxidants, unless it has been stabilized by biological consumption (Greenberg, 2009). Such possibilities make further investigation of the icy satellites especially exciting and urgent. On Europa, life, or its remains, may well be accessible close to the surface. In preparation for such a venture, comparative studies of all icy satellites will be essential. But even if extraterrestrial life were out of the question, the remarkable properties and processes on these complex worlds make them worthy of continuing exploration.

Planetary geology and geophysics have largely consisted of 'comparative planetology', a discipline that applies lessons learned on some planets to new information about others. This approach has been reasonably successful when dealing with rocky bodies for which I have a closely studied archetype, the Earth. Icy satellites pose greater challenges. Some terrestrial analogs are useful: some rock processes may be analogous to solid state processes in ice; Arctic and Antarctic ice geology may have features similar to those on icy satellites; glacier studies provide constraints on material behavior. However, the conditions on icy satellites are so alien that such comparisons require great caution. I do not understand how ice behaves in the deep interiors of planetary bodies or even what the conditions are there. Similarly, surface morphologies have formed at temperatures unknown on Earth and in materials whose properties and detailed compositions are uncertain. Continuing research will depend on application of fundamental concepts of physics, as well as consideration of planetary analogs.

II. EVOLUTION AND INTERIOR OF ICY GALILEAN SATELLITES

2.1 Evolution of satellites interiors

2.1.1 Introduction

The icy satellites of Jupiter, Callisto, Ganymede, Europa and Amalthea have diverse and remarkable characteristics. Their initial compositions were determined by conditions in the circum-Jovian nebula, just as the planets' initial properties were governed by their formation within the circumsolar nebula.

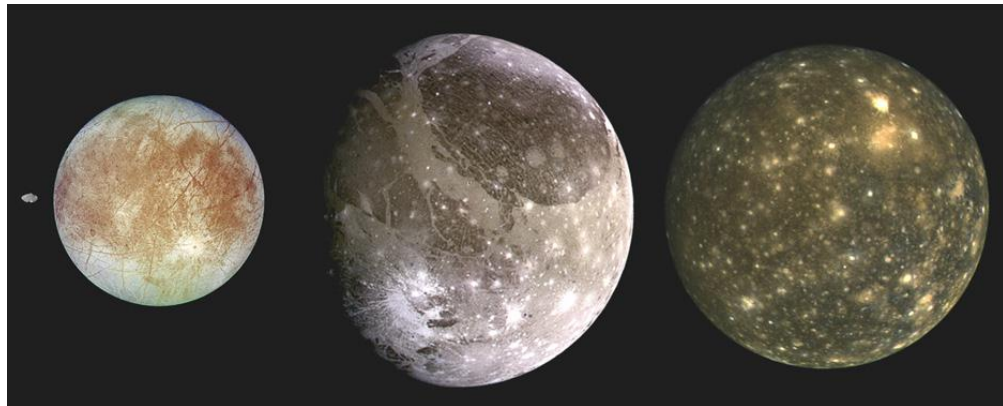


Figure II *A portrait of the icy satellites of Jupiter, with their size shown to scale. At the right is Callisto, the farthest from Jupiter, with its dark silicate veneer. With minimal endogenic activity, this surface shows at this scale the record of cratering bombardment. To the left of Callisto, at the center of the montage, is Ganymede, with 1/3 of its surface similar to Callisto's, and 2/3 consisting of younger, bright grooved terrain, strongly modified by extensional tectonic processing. To the left of Ganymede is Europa, with global scale lineaments testifying to a complex and active tectonic history, and dark splotches marking thermally driven chaotic terrain. Craters are few on Europa, indicating that this surface has continually been reprocessed by tectonics and chaos formation until very recently and may still be active. One crater, Pwyll, has a large system of bright ejecta rays, evident in this image. The tiny, elongated satellite Amalthea at the far left is the closest to Jupiter and the smallest of the group. Relatively recently recognized to be icy, Amalthea challenges models of the origin of the Jupiter system.*

The satellites subsequently evolved under the complex interplay of orbital and geophysical processes, especially the effects of orbital resonances, tides, internal differentiation and heat.

The history and character of the satellites can be inferred from consideration of the formation of planets and the satellites, from studies of their plausible orbital evolution, from measurements of geophysical properties, especially gravitational and magnetic fields, from observations of the compositions and geological structure of their surfaces and from theoretical modeling of the processes that connect these lines of evidence.

The three large icy satellites probably contain significant liquid water: Europa has a deep liquid water ocean under a thin surface layer of ice; Ganymede and Callisto likely have relatively thin liquid water layers deep below their surfaces.

Models of formation are challenged by the surprising properties of the outermost and innermost of the group: Callisto is partially differentiated, with rock and ice mixed through much of its interior; and tiny Amalthea also appears to be largely composed of ice. Each of the four moons is fascinating in its own right, and the ensemble provides a powerful set of constraints on the processes that led to their formation and evolution.

2.1.2 Satellites in Resonance:

Strong Thermal/Orbital-Dynamical Coupling

Resonances can play an important role in the evolution of satellites. Orbital periods of satellites in resonance are commensurable and their mutual gravitational perturbations at conjunction (where perturbations are near maximum) occur periodically at the same orbital phase. Perturbations to the satellites' orbital evolution are therefore significantly stronger compared with the non-resonant (stochastic) case

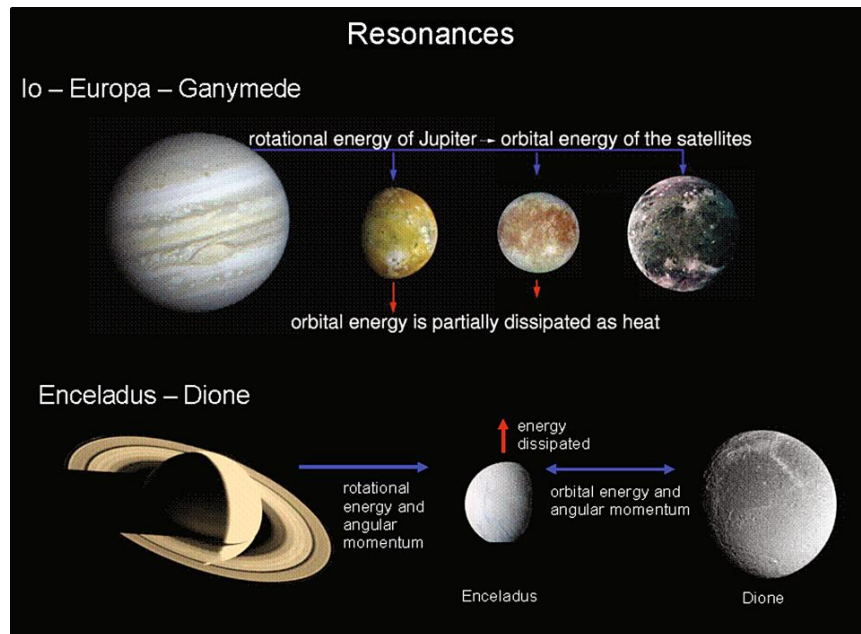


Figure III Two examples of resonances in the outer solar system involving internal heating of satellites. Rotational energy of the primary planet and angular momentum are transferred to the innermost satellite due to tidal torques. Because of the resonance coupling, energy and angular momentum are distributed among the satellites locked in resonance. Part of the energy is dissipated as heat in the satellites' interiors due to tidal flexing. This affects mainly the inner satellites close to the primary, in the first case Io and, to a lesser extent, Europa, and in the second example Enceladus (sizes and distances not to scale)

(Greenberg, et al., 1982, 1986) for a general description. The main implication for the evolution of satellites is that the orbital eccentricities are forced and maintained as long as a resonance is stable, i.e., on

geological timescales if the coupling is strong. Because the global tidal heating rate (due to tidal interaction with the primary) depends on the eccentricity squared, long-term internal heat production is strongly linked to the occurrence of resonances. In some cases when the primary is close—for instance, Io and Jupiter—this type of tidal heating can significantly exceed the heat production due to radiogenic heating. In addition to the high eccentricities associated with stable resonant equilibrium configurations, orbital eccentricities can vary considerably when the satellites pass through resonances or when oscillatory states (strongly varying orbital and thermal states) occur. Oscillatory behavior results from the disequilibrium of eccentricity forcing in a resonance and involves eccentricity damping due to tidal dissipation in the satellite. Mean motion resonances and tidal heating play an important role in the Jupiter system, mainly for Io and Europa, and in the Saturn system in the case of Enceladus (*Figure III*). Both examples are discussed below.

2.1.3 Io, Europa, Ganymede: the Laplace Resonance

The three inner Galilean satellites are locked in various resonances. For the thermal-orbital evolution the 2:1 Io–Europa mean-motion resonance and the 2:1 Europa–Ganymede mean motion resonance are the most important ones. Conjunctions of Io and Europa are locked to Io’s perijove (resonance angle librating about 0°) and to Europa’s apojove (resonance angle librating about 180°). Conjunctions of Europa and Ganymede are locked to Europa’s perijove (resonance angle librating about 0°) but to neither apsis of Ganymede (resonance angle circulating through 360°). The combination of the two 2:1 resonances yields the libration of the Laplace angle $l_1 - 3l_2 + 2l_3$ about 180° . The l_i ($i = 1, 2, 3$)

are the mean longitudes of Io, Europa, and Ganymede, respectively. This implies that whenever Europa and Ganymede are in conjunction, Io is on the opposite side of Jupiter. The Laplace configuration is stable and, after differentiating the mean longitudes with respect to time $\frac{dl_i}{dt} = n_i$ is usually expressed by:

$$n_1 - 3n_2 + 2n_3 = 0$$

Equation 1

Where the n_i are the mean motions of Io, Europa and Ganymede, respectively. This three body coupling is called the Laplace resonance, named after Pierre Simon de Laplace, who first demonstrated the stability of the orbital commensurability on theoretical grounds. Detailed reviews of the dynamics of the Galilean satellite system are given by (Greenberg, et al., 1982, 1986). The forced eccentricities associated with the above mentioned 2:1 resonances are 0.0041, 0.0101 and 0.0006 for Io, Europa and Ganymede, respectively. In the case of Europa the eccentricity is forced by both the 2:1 resonance with its inner neighbor Io and the 2:1 resonance with its outer neighbor Ganymede. Whereas the free eccentricities are negligible for Io and Europa (order of 10^{-5}), the free eccentricity of 0.0015 is the major contribution to the eccentricity of Ganymede. The free eccentricity is the remnant of the initial eccentricity after satellite formation (or after an unusual event, e.g., a major impact or a former resonance passage), which decreases with time due to tidal dissipation in the satellite. However, (Showman, et al., 1997) have shown that an impactor capable of creating Ganymede's free eccentricity would have to have had a mass 102 to 103 times greater than the mass of the impactor that formed Gilgamesh, the largest impact basin on Ganymede. The free eccentricity

is not associated with any resonance and can be regarded as the eccentricity that would persist if all the other satellites in the system were removed. Because of their forced eccentricities and their vicinity to Jupiter, Io and Europa are tidally heated on geological timescales up to the present.

2.2 Geophysics structure: Europa and Ganymede

Our knowledge of the bulk structure and composition of these satellites (*Table 1*) comes from observations of their size from images, of their mass and moments of inertia from their gravitational effects on spacecraft and on one another, and from our understanding of the types of materials likely to have condensed from the gaseous nebula surrounding the early Jupiter (Schubert, et al., 2004).

In addition, from spacecraft based magnetometer measurements, I can infer the states of iron cores that generate satellites' magnetic fields and of electrically conducting layers (probably salty liquid water) that modify Jupiter's magnetic field.

2.2.1 Europa

Table 2. Physical properties of the icy satellites of Jupiter.

Satellite	Discovery year	Radius R (km)	Density (water = 1)	Moment of inertia C/MR^2	H ₂ O (ice + liquid)	Liquid ocean	Rock	Iron (+FeS)
Amalthea	1882	$125 \times 73 \times 64$	0.86 ± 0.1		Large fraction		Mixed with ice?	
Europa	1610	1565 ± 8	2.99 ± 0.05	0.346 ± 0.005	Outer ~ 150 km	Most of the H ₂ O	Mantle below H ₂ O	Core radius is 200–700 km
Ganymede	1610	2631 ± 2	1.942 ± 0.005	0.312 ± 0.003	Outer ~ 900 km	Layer below ~ 100 km of ice	Mantle below H ₂ O	Core radius is 650–900 km
Callisto	1610	2410 ± 2	1.834 ± 0.003	0.355 ± 0.004	Mixed with variable amount of rock to depth of ~ 1000 km	Layer below ~ 100 km of ice	Mixed with ice in outer ~ 1000 km, mixed with iron below	Mixed with rock inside radius ~ 1200 km

Table 1 Physical properties of the icy satellites of Jupiter

Europa, with a radius of 1565 km, has a density of $2.99 \pm 0.05 \text{ g cm}^{-3}$, much greater than water (density 1 g cm^{-3} , by definition) or ice which is a few per cent less dense than liquid water (Schubert, et al., 2004). From its measured moment of inertia (*Table I*) I know that internal heating by radioactivity and tidal friction must have differentiated the internal composition by density and the H₂O of Europa is confined to an outer layer of thickness $<170 \text{ km}$. The gravity constraints would allow the low-density portion to include a substantial layer of hydrated silicates (i.e. clays) below the water, in which case the H₂O layer could be as thin as 80 km. On the other hand, geochemical considerations argue against the expectation of much clay. Thus most estimates for the thickness of the H₂O layer are $\sim 150 \text{ km}$.

The most significant characteristic of Europa's interior is the state of this thick H₂O layer. It is nearly all liquid, constituting a global ocean with roughly twice the liquid water of all of the Earth's oceans combined, and covered with only a relatively thin outer crust of ice. The ocean is maintained as a liquid due to the action of tides, which in turn depend on the orbital eccentricity of Europa, which in turn is maintained by the Laplace resonance. The resonance, and how it forces the orbital eccentricity is discussed in section 2.1.2.

If Europa were on a circular orbit, tides would elongate its figure along an axis aligned with Jupiter. If the rotation were initially non-synchronous with the orbital period, the orientation of the tidal distortion would have continually been reoriented relative to the body of the satellite. Due to energy dissipation in the material of the satellite, this response would have lagged slightly behind the tide-raising potential, yielding an asymmetry of the tidal Figure relative to the direction of Jupiter, and thus a torque, which would have slowed the spin to synchronous in well less than a million years. Afterwards, the only effect of tides would be to maintain a constant tidal elongation,

fixed relative to the body. Any other geophysical effects would be negligible. Europa's orbital eccentricity changes the story completely.

The tides on its body change over the course of each 85 h orbital period. Even with the rotation nearly synchronous (Hoppa, et al., 1999a,1999b), keeping one face toward Jupiter, the magnitude and orientation of the tidal distortion changes throughout each orbital period. As shown in *Figure IV*, the tide-raising gravitational effect is at a maximum at pericenter, when Europa is closest to Jupiter, and a minimum at apocenter, when it is farthest away. In between, the direction of Jupiter relative to the body of Europa is shifted slightly. The body of Europa must continually remold itself in order to conform to the shape driven by the tide. The true proportions of the geometry are not shown in *Figure III*. Europa's radius is about 1560 km and it averages a distance of 671 000 km from Jupiter, whose radius is about 71 500 km. The average height of each tidal bulge on Europa is about 500 m. Europa's orbital eccentricity is 0.01, so the elliptical epicycle traced out by Jupiter relative to Europa (shown in *Figure VI*) has dimensions 13400 km by 26800 km and Europa's distance from Jupiter varies by less than 1%. That small variation in distance means that the orbit is nearly circular, but the variation is enough to drive dramatic effects on Europa.

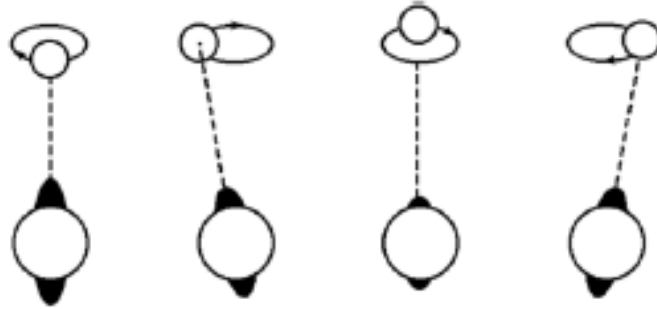


Figure IV The tide on Europa (at the bottom) is shown schematically at four points (from left to right) in its orbit. The black bulges represent Europa's stretched shape. Jupiter is the small circle (obviously the giant planet is not to scale) near the top. The frame of reference used here is locked to the body of Europa, so Jupiter always remains on the same side. The eccentricity of the orbit produces small variations in the distance and direction of Jupiter relative to the body of Europa, which appears in this reference frame as epicyclidal motion. The size and orientation of the bulges qualitatively indicate the variation in the tidal distortion of the body.

The amplitude of the tidal potential, and thus the elongation of the satellite's figure, is proportional to a^{-3} . Thus the height of the tide is found to vary by $3e$ times the mean tidal distortion. For Europa with $e = 0.01$, the amplitude of the tidal variation is about 30 m. That result assumes that the value of h_2 is the same for the rapidly varying diurnal tide as it is for the nearly constant primary tide. The elongation of the tidal figure of the satellite also depends on the internal physical properties, such as the effective rigidity of the satellite as a whole, as well as on the distance from Jupiter. The 'Love number' h_2 characterizes the effect of these physical properties on the shape of the tidal distortion. Because the 85 h timescale for the change in the tide is so short, the physical properties of the materials involved (viscosity, as well as rigidity) may play a role in limiting the amplitude of variation of tidal deformation. How can I estimate the value of h_2 for this dynamic situation? Computed results from proprietary codes are available for only a few interior models. They indicate however that, even with the rapid, continual change in the tidal potential over the course of beach

day on Europa, the outer surface can conform to the shape dictated by that tidal potential (Yoder, et al., 1996), (Moore, et al., 2000), (Hurford, 2005).

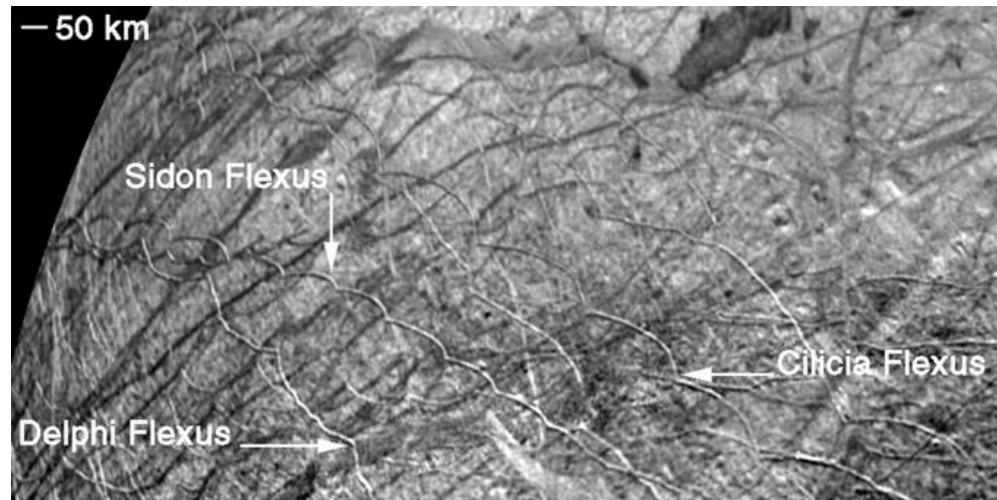


Figure V Cycloidal crack patterns (chains of arcs), are ubiquitous on Europa, usually displayed in the form of double ridges lining the sides of the cracks. This image from the Voyager mission in 1979 shows beautiful, but typical, examples of cycloidal ridges, including Cilicia, Delphi and Sidon Flexus. Arcs are typically about 100 km long, and many cycloids comprise a dozen arcs or more. Older cycloids have been sliced and diced by subsequent tectonic and thermal processing, and thus may only appear as short arcuate features or isolated cusps.

Therefore, the value of the Love number h_2 for the diurnal tide should be reasonably close to the value (~ 1.2) that it would have for the primary (nearly constant) component of the tide. So as long as Europa's water is largely liquid, the estimate of 30m for the amplitude of the tidal variation is probably reasonable.

The tidal variation is fairly independent of whether the ice crust is very thin or several tens of kilometer thick, as long as most of the water under the ice is liquid. Only if the water is nearly all frozen does the tidal amplitude drop significantly, and then it can drop by an order of magnitude. When spacecraft return to Europa, they will likely be equipped with altimeters capable of measuring the amplitude of this tidal variation, which would complement measurement of the

gravitational effects of the tidal shape on the spacecraft's motions. In principle, these measurements could help constrain internal properties, such as the thickness of the ice (Europa Science Definition Team 2008). However, the fact that tidal amplitude is relatively insensitive to the ice thickness, if the thickness is less than a few tens of kilometers, is somewhat discouraging, because determining the thickness of the ice is a crucial issue. Unfortunately, other uncertainties in the details of internal structure and materials probably will swamp out the effect of ice thickness on tidal variation. Measurements of tides will tell us whether there is an ocean, but I would need very precise measurements and improved interior models if there is to be any hope of using this approach to determine the thickness of the ice. The continual remolding of the figure of Europa entails friction and so generates heat, enough to keep the water layer in the liquid state, with only a relatively thin outer shell of ice (Peale, et al., 1979), (Squyres, et al., 1983), (O'Brien, et al., 2002). The first observational evidence that most of the water is liquid came from interpretation of characteristic cycloidal crack patterns (*Figure V*), which could be explained by tidal stress, but only if a thick fluid layer allowed sufficient amplitude for the tides (Hoppa, et al., 1999a,1999b). However, strictly speaking, that evidence really only applied to the time that the cracks were formed, which although very recent in geological terms (less than ~1 million years ago) could not definitively address the presence of the ocean now. Evidence for the existence of the ocean more recently, at least up to the end of the 20th century, came from the Galileo spacecraft's magnetometer, which showed variations in Jupiter's magnetic field that could be explained by an ocean within 200 km of the surface of Europa (Khurana, et al., 1998), (Kivelson, et al., 2000), (Zimmer, et al., 2000).

In fact the ocean comes quite close to the surface, as indicated by a variety of geological features. These features are best explained by

linkage to the ocean below (Greenberg, et al., 2002) (Greenberg, 2005) (Greenberg, 2008). The ice shell is probably permeable due to ever-changing tectonic and thermal connections, suggesting ice thinner than ~10 km, but with thickness varying with time and place. Uncertainties about the amount of internal heating and the heat transport processes through the ice have frustrated geophysical modeling of the ice thickness from that perspective. However, a more recent examination of the Galileo magnetometer data gives a best-fit to the ice thickness of about 4 km (Hand, et al., 2007).

In any case, the bulk of the H₂O on Europa probably forms a deep liquid water ocean just below the ice. Below the ocean lies the rocky 'mantle' and the iron core. Estimates of the size of the core depend on assumptions about the amount of iron sulfide included, so the core radius could be as small as 200 km or as large as 700 km (Schubert, et al., 2004). Because the Galileo magnetometer found no internally generated magnetic field, the core must be solid or, if it has a liquid layer (consistent with the tidal heating implied by the liquid water ocean), it must not be convecting (Schilling, et al., 2004). In its bulk structure, Europa could hardly be called an icy satellite. By volume, it is 2/3 rocky mantle plus core. Moreover, with most of its water in liquid form, only about 1% of Europa's volume is ice. However, in terms of its surface appearance, which provides most of our observational data, Europa is an icy satellite (Greenberg, 2005, 2008).

2.2.2 Ganymede

Ganymede's moment of inertia value is low enough that, like Europa, it implies complete interior differentiation into separate layers of water, rock and iron. Of the total radius of 2410 km, the outer layer of H₂O is about 900 km thick, the interior core is 650–900 km in radius and in

between is the rocky mantle (Schubert, et al., 2004). Early heating by radioactivity and by dissipation during accretional impacts was probably adequate to explain the complete differentiation, but tidal heating due to the orbital resonance with Europa and Io may have been a factor as discussed in previous section. Ganymede is the only Galilean satellite with a magnetic field, which has a strength at the surface of about 1/10 of that of the Earth (Kivelson, et al., 2002). To generate this field, the core is generally believed to be currently molten. If it were not, the only other possibility would be that the satellite retains remnant magnetism from an earlier time when the core acted as a dynamo. However, Cray and Bagenal (1998) showed that only the outer portion of the rocky mantle would be cool enough to retain magnetism, probably too thin a layer to contain enough magnetic minerals to support the observed field. Problems also remain with modeling the core dynamo, because adequate convection is needed. Hauck *et al* (2006) suggested that as the inner core gradually solidifies, concentrations of sulfur in the remaining liquid can yield compositionally driven convection, but it remains uncertain whether that mechanism is quantitatively viable. More recently, Bland *et al* (2008) argued that, without rapid enough heat removal out through the rocky mantle, there would not be enough of a temperature gradient to drive convection in the core. That requirement means that the mantle itself would need to convect heat outward. Bland *et al* suggest that the heat for the necessary mantle convection came during a period of formation of the Laplace resonance when Ganymede had a larger forced eccentricity and thus underwent significant tidal heating, according to a scenario suggested by Showman and Malhotra (1997) and Showman et al (1997).

Uncertainties in that orbital evolution scenario is discussed in previous section. Moreover, Bland et al acknowledge that more work is needed on

possible rheologies before their thermal model can be convincing. Thus the source of Ganymede's magnetic field remains an open question.

In addition to the internally generated magnetic field, the Galileo spacecraft's magnetometer detected variations in the Jovian magnetic field in the neighborhood of Ganymede that can plausibly be explained by an electromagnetic induction in a conducting layer, suggesting (as for Europa) a layer of liquid salty water. However, in contrast to Europa, the conducting layer must be well below the surface. Accordingly, observations of the surface geology do not show any signs of interaction with the liquid layer.

Interior models of ice properties at depth are consistent with the possibility of a liquid layer (Spohn, et al., 2003), (Schubert, et al., 2004). As is well known, the melting temperature of water decreases slightly with modest pressure, but as the pressure increases further, the melting point rises (Chizov, 1993). For Ganymede, the minimum melting temperature would be at 150 km below the surface, assuming pure water. Thus any liquid would be around that depth, with ice layers above and below it. Assuming a reasonable heat flux, if the outer ice is conductive, the equilibrium thickness of ice above the liquid layer would be about 100 km. In that case, the liquid layer would be quite thick, extending from depth 100 km down past the minimum-melting-point depth of 150 km. On the other hand, if the outer layer of ice is convecting, it conveys heat more efficiently so its equilibrium thickness is greater, leaving space for only a few kilometers of liquid at most. Salt in the water changes the story only slightly. Ammonia, which is another plausible substance (Kargel, 1992) could make a very big difference: an ammonia-water layer could be 200– 300 km thick and as close to the surface as 70 km (Sotin, et al., 1998). Without knowledge of the interior heating rate, the thermal history, the actual composition of the solute or the mode of heat transport (convection versus conduction), these

figures are all speculative. Even so, they do demonstrate the plausibility of a fluid layer within the ice as an explanation for the magnetic field variation (Spohn, et al., 2003).

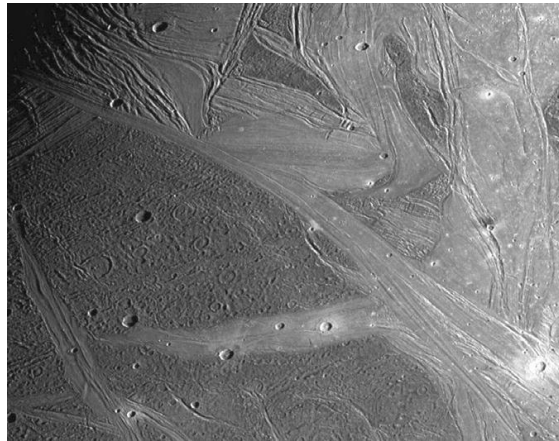


Figure VI *The bright grooved terrain on Ganymede contrasts with the dark ancient terrain in this much high resolution. The greater crater density on the dark terrain is evident, as is the predominantly tectonic character of the brighter terrain. This region is about 660 by 520 km in size with resolution about 1 km per pixel (JPL Image PIA 1617).*

Even with the liquid layer buried too deep to have a direct influence, the surface of Ganymede displays the effects of substantial geological activity and variability. Only about 1/3 of the surface is dark and heavily cratered, with relatively little evidence of endogenic activity since formation of the satellite (Shoemaker, et al., 1982), (Pappalardo, et al., 2004). The crater record here indicates a surface age of >4 Byr. The darkening may result from silicate or other impurities that remained in the cold icy outer crust, even while the interior underwent heat-driven differentiation. Sublimation of ice may have further concentrated dark material in a thin layer near the surface. In considering the low albedo of this terrain, it is important to bear in mind that even a relatively small concentration of dark material dispersed through ice can absorb a surprisingly large amount of light.

The remaining 2/3 of the surface has been converted into relatively bright terrain characterized by complex sets of roughly parallel grooves (Golombek, 1982), (Shoemaker, et al., 1982). The surface here seems to have been stretched, and thus heavily faulted, exposing the brighter ice from below (*Figure V*). In addition, this modified terrain shows evidence of volcanic resurfacing, a process often called cryovolcanism, because on Ganymede liquid water flows out and over ice, rather than molten lava flowing over rock.

The crater record on the bright two-thirds of the surface confirms that it is younger than the old, dark, heavily cratered one-third. The nominal age of the reprocessed portion is about 2 billion years (Zahnle, et al., 2003) a figure that suggests that global-scale endogenic processes occurred long after formation of the Jovian satellites system, but then turned off very long ago. This timing appears to be a major constraint on the evolution of the Jovian system. However, the crater based age is so uncertain that the resurfacing could have been associated with the initial formation of the satellite, rather than a subsequent heating event. The range of uncertainty also admits the possibility that the surface is relatively recent.

However, in contrast to Europa's surface which may still be undergoing continual renewal, Ganymede's has probably been relatively unchanged for at least 1/2 billion years and perhaps for as long as 4 billion years.

2.3 Composition of the upper layers of the icy Galilean satellites

Although it has been known since the early spectroscopic measurements from Earth that the surface of Europa, Ganymede and Callisto is predominantly constituted by water ice, detailed evidence of

the presence and nature of other species could be obtained only with the Galileo mission. Such compounds may either originate within the satellite itself, or be implanted by exogenic processes. Endogenic species may in turn either be in place since the original formation of the satellite, or they may have been created by chemical processing in the interior, and emplaced at the surface by endogenic processes such as cryovolcanism or extensional tectonics (*Tobie et al., 2010*).

Exogenic species include charged particles trapped in Jupiter's magnetosphere and implanted in the surfaces of all four Galilean satellites. Additional material may be brought by comets, meteorites or micrometeorites, while Europa receives also matter ejected from Io. Exchanges of material between the interior and the surface are also taking place on Io and Europa, while it seems that the current internal activity of Ganymede is limited, and that of Callisto is practically absent (*Sohl et al., 2010*). The main source of energy driving internal activity of the Galilean moons is the same, namely the tidal forces caused by their resonating elliptical orbits, but its intensity decreases with increasing distance from Jupiter. This results in the unceasing volcanic activity of the innermost satellite, Io, and in the increasing ice crust thickness and uncertainty on the presence of a subsurface ocean in moving from Europa to Ganymede and Callisto. The dissipation of tidal energy heating the Galilean moons results not only in a global geologic activity, but allows also chemical processes creating a number of compounds that have been detected and mapped through observations by recent spacecraft missions.

On Europa, spectra collected by the NIMS experiment have been interpreted as indicative of the presence of hydrate compounds, concentrated in visually dark and reddish regions. Some authors (e.g., *McCord et al., 1998, 1999; Dalton, 2003; Dalton et al., 2005*) hypothesize that such material is made of hydrated salt minerals enriched in Mg and

Na sulphates, formed by the crystallization of brines erupted from the subsurface ocean. Alternatively, it has been proposed that contaminants of the mostly water ice surface consist of hydrated sulphuric acid ($H_2SO_4 \cdot nH_2O$), formed by the radiolysis of water and of a sulphur-bearing species, or by the decomposition of sulphate salts [Carlson *et al.*, 1999]. More recently, Orlando *et al.* [2005] and Dalton [2007] found a better match for Europa spectra in mixtures of sulphuric acid hydrates together with hydrated salts. Other non-water-ice species, like CO_2 and H_2O_2 , were also detected in the leading hemisphere at equatorial to mid-latitudes.

On Ganymede, the composition of the non-water-ice material ranges from heavily hydrated at high latitudes, similar to that on Europa, to only slightly hydrated compounds [McCord *et al.*, 2001]. Galileo data and ground-based spectra allowed the identification of carbon dioxide, sulphur dioxide, molecular oxygen, ozone and possibly cyanogen, hydrogen sulphate and various organic species [e.g., McCord *et al.*, 1998]. The organic material could be formed in situ as a co-product of radiolysis and chemical reactions within the contaminated icy crust, and from exogenic material falling onto Ganymede's surface.

The surface composition of Callisto is thought to be broadly similar to its bulk composition, because of its less evolved state compared to the other Galilean moons. Non water-ice compounds include Mg- and Fe-bearing hydrated silicates, CO_2 , SO_2 , and possibly ammonia and various organic compounds (Moore *et al.*, 2004; Showman and Malhotra, 1999), with abundances greater than those reported on Ganymede and Europa. Other chemical species are predicted to be present because of models or experiments on the formation and evolution of these satellites. These species include aliphatic hydrocarbons, heavily hydrated and/or hydroxylated minerals and tholins (Dalton *et al.*, 2010).

Table II, adapted from (Dalton 2010), summarizes the discussion of the previous paragraphs.

Satellite	Temperature	Known Compounds	Expected Compounds
Europa	86-132 K	H ₂ O, SO ₂ , CO ₂ , H ₂ O ₂ , O ₂ , hydrates of H ₂ SO ₄ , MgSO ₄ and Na ₂ SO ₄	heavily hydrated and/or hydroxylated minerals, tholins
Ganymede	90-160 K	H ₂ O, SO ₂ , CO ₂ , O ₂ , O ₃	aliphatic hydrocarbons, heavily hydrated and/or hydroxylated minerals, tholins
Callisto	80-158 K	H ₂ O, SO ₂ , CO ₂ , O ₂ , silicates	aliphatic hydrocarbons, heavily hydrated and/or hydroxylated minerals, tholins

Table II Major compounds identified on the three icy Galilean satellites, and those predicted by models or experiments. Table adapted from Dalton [2010], data taken from Carlson et al. [1996, 2005, 2009], Dalton [2007], Hanel et al. [1979], Hibbits et al. [2000], Moore et al. [2007], Orton et al. [1996], Roush [2001], Spencer et al. [1999].

2.4 Geology: surface appearance and processes

2.4.1 Europa

The dramatic continual resurfacing of the ice shell of Europa has produced two main types of geological terrain: tectonic and 'chaotic', representing the tidal effects of stress and of thermal processing, respectively (Greenberg, et al., 2002) , (Greenberg, 2008). On a global scale these features are recognizable as lineaments and splotches marked by slight darkening, probably representing deposition of oceanic substances through cracks or melt zones.

Few craters are visible because of the recent resurfacing. At higher resolution (*Figure VII*), the global-scale lineaments resolve into double dark lines, usually called 'triple bands' (counting the space between the dark bands), shown crossing in this image. Here I also see the archetypical patch of chaotic terrain, which is the dark splotch below the intersecting triple bands. At still higher resolution (*Figure VIII*), and with a lighting angle that is more revealing of topography, I see that the global-scale lineaments actually consist of complexes of multiple sets of roughly parallel double ridges. The double dark lines that define the triple bands are simply a diffuse subtle darkening along the margins of the ridge complexes, and not structural features at all. Global-scale lineament patterns correlate roughly with tidal tension patterns.

Tectonic terrain is dominated by double ridges, whose central grooves mark cracks in the crust. The densely ridged terrain lies in the northern part of *Figure VII*. The ridges may form as cracks initiated by tidal stress are continually worked by periodic tides that squeeze up crushed ice and slush. Many crack features follow the cycloidal patterns predicted for tidal stress (*Figure V*), with chains comprising as many as a dozen arcs, each arc typically ~100 km long.

Large plates of the ice shell, often hundreds of kilometers across have undergone major displacement, including dilation of cracks, which has allowed infilling from below, and strikeslip (shear) displacement.

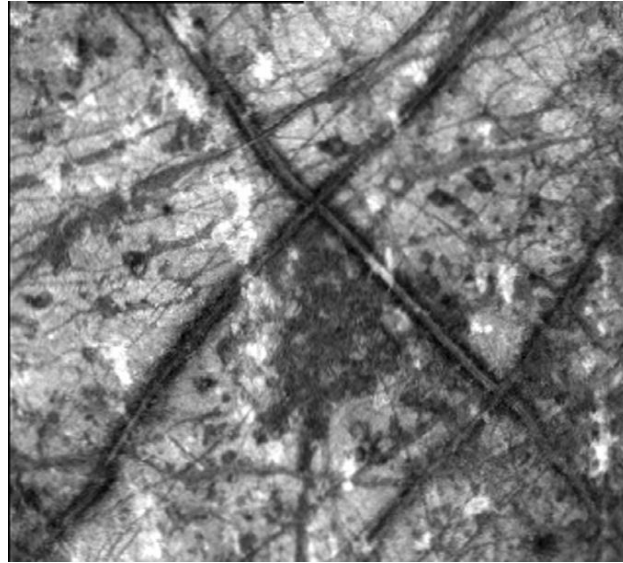


Figure VII A 300 km wide region on the surface of Europa at the intersection of two of the global-scale lineaments (which form the X just to the upper right of center in the disk of Europa shown in Figure II). The global lineaments here resolve into double dark lines called 'triple bands'. The dark area below the intersection is Conamara Chaos. The vertical white streaks are rays of ejecta from an impact crater 1000 km to the south.

The strike-slip is probably driven by diurnal tides, and the ubiquitous displacement is facilitated by the low viscosity of the underlying liquid ocean. Because the tectonic patterns can be fit to the predictions of tidal-stress theory, evidence has been developed for non-synchronous rotation (which further enhances tidal stress), and for polar wander in which the icy shell slips around relative to the spin orientation of the satellite.

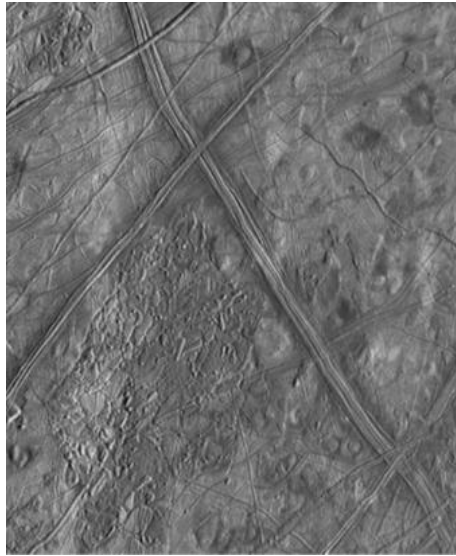


Figure VIII *The Conamara Chaos region on Europa at much higher resolution (~180 m/pixel) than in Figure XI, and with more advantageous lighting, shows morphological detail of the chaotic terrain, which fills is apparent. The double lines that dominate their appearance in Figure XI, are here only a diffuse darkening along the margins of these ridge systems.*

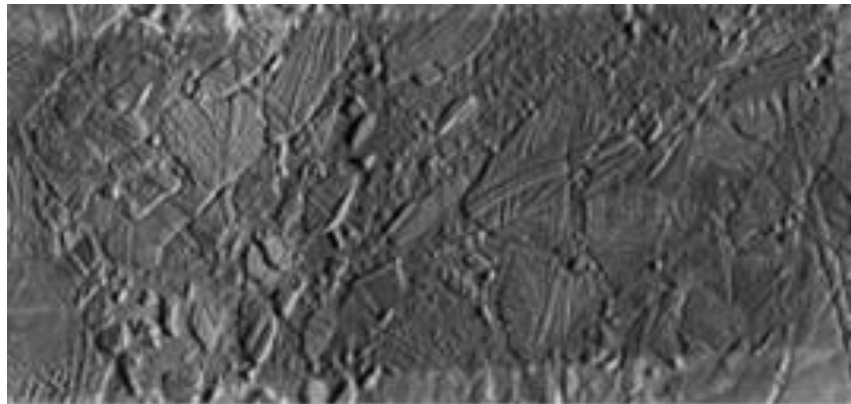


Figure IX *A mosaic of high-resolution images (54 m/pixel) within the Conamara Chaos region of Europa (Figure X). Within a lumpy matrix, rafts of displaced crust display fragments of the previous tectonic terrain. Subsequent to the formation of the chaotic terrain, probably by melt through from below, the fluid matrix refroze and new double ridges have formed across the area and begun the process of tectonic resurfacing*

Nearly half of the surface of Europa comprises chaotic terrain, where the surface has been disrupted, with rafts of older terrain displaced within a lumpy matrix (*Figure IX*).

Chaos likely represents melt through, perhaps from the ocean below, followed shortly by refreezing. Only modest concentrations of tidal heat are needed to melt through the ice (O'Brien, et al., 2002).

While creation of chaotic terrain destroys older surfaces, chaotic terrain in turn can be destroyed by subsequent tectonics.

The history of Europa has been an on-going interplay of resurfacing, by tectonics and by chaos formation, with each destroying what was there before, and with each seemingly involving breakthrough of the ocean to the surface (Greenberg, 2005, 2008).

2.4.2 Ganymede

The darker 1/3 of Ganymede's surface is enriched in impurities, probably predominantly hydrated silicates, which avoided the internal differentiation and may have been accreted late in the formation of the satellite (Pappalardo, et al., 2004). This older terrain is relatively heavily cratered and also includes other impact features: palimpsests and concentric furrows. Palimpsests are round, subtly brightened patches where the topography of an impact feature has evidently relaxed away. Furrows ~10 km wide and typically spaced ~50 km apart are generally part of large circular systems that record large early impacts. Other groups of furrows in the dark terrain may be extensional features, like graben, and sometimes are oriented parallel to the borders with the younger brighter terrain (*Figure X*).

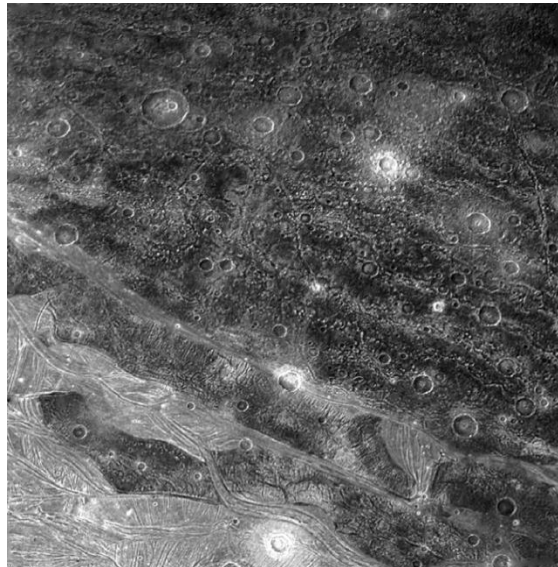


Figure X *The dark regions on Ganymede contain sets of furrows, which are often parallel to the borders with the bright grooved terrain as seen here. These dark-region furrows may have formed by surface extension, an incipient version of the kind of tectonic processing that produced the bright grooved terrain. Furrows in the dark regions also often display concentric patterns suggesting that they formed as rings around impact basins, similar to those of Valhalla on Callisto). In the foreground (lower left) is typical bright grooved terrain. Craters of various morphologies are displayed in this area. The area shown is about 450 km wide in a Voyager image (NASA/JPL PIA 2281).*

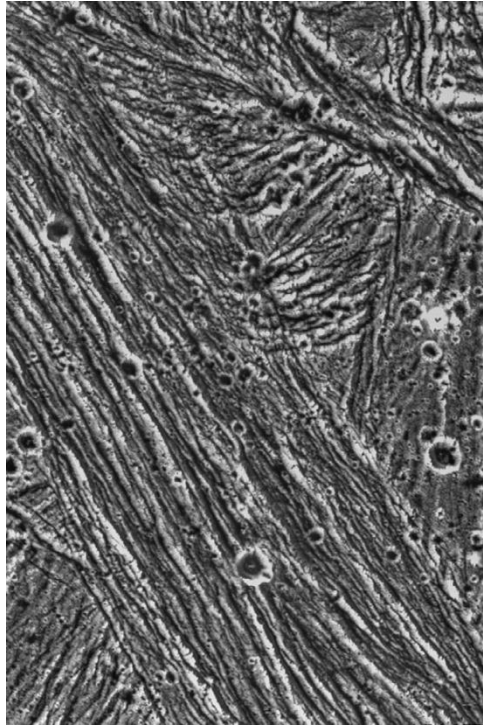


Figure XI *High-resolution image of bright, grooved terrain on Ganymede showing details of the extensional tectonics. This image, taken by the Galileo spacecraft, shows an area 35 km wide at a resolution of 74 m/pixel (NASA/JPL PIA 0277).*

The brighter terrain comprises bands of roughly parallel grooves that have cut across the darker terrain, and cover 2/3 of the surface. This terrain (in the bright parts of *Figure IX* and in *Figure X*) appears to be the result of surface extension, probably more mature versions of the extensional furrows on the dark terrain (Golombek, 1982), (Pappalardo, et al., 2004). The extension of Ganymede's icy surface is very different from that on Europa. On Europa, dilational bands formed where cracks have opened tens of kilometer wide, allowing infilling by new material, all due to the mobility provided by the near surface ocean. Terrains on opposite sides match and can be reconstructed by removing the band material. On Ganymede, the old terrain on opposite sides of the bright grooved terrain cannot be matched. The material in between is generally

not newly emplaced, but rather old surface that has been modified by the stretching. The grooves and furrows that characterize the brighter terrain probably result from various extensional tectonic processes. They appear to have two characteristic scales, even in the same bright band. Voyager images (e.g. *Figure X*) revealed a typical spacing ~ 10 km and topographic amplitudes of up to 500 m, while the higher resolution from Galileo imaging (e.g. *Figure XI*) showed a superimposed periodicity typically ~ 1 km with amplitudes of ~ 200 m. Most models envision the extension starting with the longer wavelength furrowing, like what is seen on the dark terrain, either due to periodic graben formation (similar what formed the basin-and-range terrain in the US southwest) or by extensional necking of the lithosphere (the cold, brittle-elastic upper portion of the ice). The shorter wavelength grooves may have followed by finer scale tilt-block faulting. There is considerable literature addressing these possibilities, most recently the numerical modeling of the necking instabilities by (Bland, et al., 2007). The idea is that, as a brittle elastic upper layer is pulled under tension, any perturbation in the thickness of the layer becomes more susceptible to further stretching and thinning. Models show that this instability can lead to periodic groove formation, although questions remain as to whether the mechanism could produce amplitudes as great as what is observed. The brightening of this extensional terrain relative to the older dark terrain is in part due to exposure of the purer ice just below the surface by the faulting. In addition, liquid water may have oozed to the surface ('cryovolcanism') to some degree in these regions (Schenk, et al., 2001), (Schubert, et al., 2004), (Showman, et al., 2004) demonstrated that topography like the grooves could create subsurface pressure gradients, which would force any liquid to the surface, if there were a partial melt within ~ 10 km of the surface. That model requires that

Ganymede was sufficiently heated at one time, perhaps due to a past state of the Laplace resonance (as discussed in previous section).

The dominance of extensional geology on a global scale seems to require that Ganymede has expanded significantly since the formation of the old, dark terrain.

The most plausible explanation for such global expansion follows from Ganymede's icy composition and the internal differentiation: when the lower density ice rose up from the deep interior, the release of pressure allowed substantial expansion.

Thus, whenever the surface modification occurred, the first major internal heating must have occurred at about the same time, an important constraint on models of formation and orbital evolution. These events may have been either long after Ganymede's formation as indicated by the nominal crater age or early in the lifetime of the satellite as permitted by crater-age uncertainty.

Ganymede's dark terrain has also undergone 'mass wasting' (downslope movement of surface materials) as evidenced by landslide morphologies (Moore, et al., 1999), exposure of brighter material on slopes and accumulation of darker material in topographic lows (Oberst, et al., 1999).

Sublimation has also modified the dark terrain, seeming to have concentrated darker material as ice sublimates off sunfacing slopes with frost deposits forming preferentially on the opposite slopes. Diffuse polar brightening can be explained by such frost deposition near the poles.

III. MARS

3.1 Background

Even though there is little water on the surface of Mars today, the landscape shows abundant evidence of erosional features created by liquid water, indicating a warmer and wetter climate in the past than at present (Carr, 1996). At present there are minute amounts of water in the atmosphere, and liquid water is unstable at the surface. Ice has only been detected with certainty at the poles, however, it is most likely also present in the ground at high latitudes. Despite the sparse amount of water compared to past times, there is an active water cycle on Mars even today. Spacecraft have observed the formation of ice clouds and water frost on the surface and have measured the atmospheric water vapor content, which shows seasonal and spatial changes in the atmospheric water distribution through the Martian year.

3.2 General characteristics

Mars and Earth are the two planets in the Solar System which are the most alike in climatic aspects. They are both terrestrial i.e. they consist of rock and metal, and the gravity on the surface of Mars is $0.38 \cdot g$ compared Earth $\left(g = 9.82 \frac{m}{s^2} \right)$. Mars rotates at approximately the same rate as Earth (a Martian day called a sol is 24.66 Earth hours), and its orbit around the Sun takes 669 sols, which is a little less than two Earth years. The obliquity of the two planets (the inclination of the rotational axis to the ecliptica) is very similar; 25° for Mars compared to 23.5° for Earth. However, the eccentricity of Mars' orbit is greater than that of

MARS

Earth, which results in a greater difference between the maximum solar insolation on the northern and southern hemisphere. At present Mars is closest to the Sun at the end of southern spring, so southern summers are shorter but warmer than those in the north (Carr, 1996).

Atmospheric motion on the two planets is governed by the same laws of physics, yet there are still some differences in the circulation on Mars, which can be explained by the differences between Earth and Mars as described below.

Atmospheric composition: Mars' atmosphere consists predominantly of CO₂ with some noble and trace gasses.

Temperature: Mars is colder than Earth due to two primary reasons.

1) The larger distance to the Sun causes the surface of Mars to receive less solar radiation and 2) the less dense atmosphere causes a smaller greenhouse warming. During winter time the atmosphere will become so cold that the atmospheric CO₂ will condense on the surface in the polar region, which induces a mass driven flow of air towards the winter hemisphere.

Topography: Mars has a greater variation in its topography. The highest point, the highest volcano in the solar system, is Olympus Mons at 26 km above the areoid, and the huge impact basin Hellas forms the lowest point at 8.2 km below the areoid. Mars has a distinct dichotomy, the average altitude of the southern highlands being several km higher than the smooth northern hemisphere, which only has few craters.

See *Figure XIII* for a topographic map of Mars.

Airborne Dust: Mars has recurring huge dust storms, which sometimes cover the whole planet, the largest ones occur during the southern summer. The airborne dust affects the radiative transfer in the atmosphere significantly, which leads to a huge potential for feedback processes between the dust distribution and the general circulation.

MARS

No liquid water: Mars has no liquid water on the surface today due to two causes. 1) The low atmospheric pressure (which is usually just below the triple point of water, which is given by $T = 273.16 \text{ K}$ and $P = 611.73 \text{ Pa}$. 2) The low surface temperature, which is usually below the freezing point of water, although the temperature does sometimes rise above it. The lack of an ocean simplifies the climate dynamics and possible mechanisms of lateral heat transport on Mars compared to Earth.

3.3 Volcanism

The Northern Hemisphere is also characterized by an extended volcanism, by the sign of a past extended tectonic activity, that was generating the largest rift in the solar System named "Valles Marineris". The extended volcanism produced large volcanoes, arranged in sequences, as seen on the Earth in the Hawaiian islands.

The volcanic features on Mars are very similar in shape, but not in dimensions, to those found on Earth, and they probably formed by similar processes. Martian volcanism extended for a large time-span and the volcanoes were generated on terrains of variable ages. Numerous volcanic landforms can be found in the older cratered highlands and in the younger volcanic plains surrounding them. However, the most impressive volcanic landforms are associated with the extensive, hotspot-related uplifts of Tharsis and Elysium plateaus. The large scale of the Tharsis shield volcanoes suggests that they formed from massive eruptions of fluid basalt over prolonged periods of time. Similar eruptions on Earth are associated with flood basalt provinces and mantle hotspots. However, on Earth the source region for hotspot volcanism moves in respect to the crust, due to the plate tectonics. On

MARS

Mars an extensive plate tectonics never developed, and I speak now, about a “one-plate” tectonics. Therefore, the Martian surface remains above the plume source so that huge volumes of lava will erupt from a single central vent over many millions of years of activity. A single shield volcano of enormous volume is then generated. The most spectacular volcanic features on Mars are the isolated, giant basaltic shield volcanoes called Montes. The largest of these are four giant shield volcanoes associated with Tharsis uplifted region. The largest of the four is Olympus Mons, the largest volcano in the solar system, with a base diameter of 600 km and 25 km of relief from the summit to the plains surrounding it abrupt basalt scarp. Smaller volcanoes are called Tholi and Peterae characterized by smaller volcanic vents. A Tholus volcano is an isolated mountain with a central crater, and a Patera volcano is dominated by an irregular or complex caldera with scalloped edges, surrounded by very gentle slopes.

At present, the processes that gave rise to the volcanism are not any more active. Only locally, and at small scale, volcanism could be still present. This is very important for the search of life, since the presence of hydrothermal volcanism, some micro-organism could survive.

Geomorphic features visible in orbital images obtained during the Viking missions of the late as well as the infrared spectral data obtained from the floors of rifted basins, or on Mars are suggestive of hydrothermal activity. OMEGA (the IR Mapping Spectrometer of Mars Express) data have permitted to identify deposits of sulphates, indicative of past hydrothermal processes on Mars. Another evidence for hydrothermal activity on Mars derives from studies of SNC meteorites, objects believed to have come from Mars. SNC meteorites comprise a geochemically and isotopically related group of objects that have bulk compositions similar to terrestrial basalts (Newsom et al. 1999). In these meteorites, are present minerals of primary hydrous, including amphiboles and micas

contained within glassy of primary igneous origin, as well as post-crystallization minor, sulfates, carbonates, halides and ferric oxides formed through interactions with late-stage aqueous solutions.

3.4 Tectonics

The formation of large volcanic edifices has produced also a large tectonic activity. This was probably produced by mantle processes such as solid-state mantle convection. Because of the large-scale up-warping at Tharsis, fracture systems either radial or concentric to the Tharsis bulge have been identified. This is a network of interconnected grabens centred on the non-volcanic part of the Tharsis uplift and next to the western edge of the Valles Marineris. It is clear that the older, north-trending fractures were overlaid by the younger, more chaotic system. Lithospheric deformation models show that loading over the scale of Tharsis (large relative to the radius of the planet) produces the concentric extensional stresses around the periphery and the radial compressional stresses closer in that are needed to explain the radial grabens and rifts and concentric wrinkle ridges. According to Golombek (2005) models based on present day gravity and topography can explain the observed distribution and strain of radial and concentric tectonic features, implying that the basic lithospheric structure of Tharsis has probably changed little since 3.7 Ga. This Tharsis load appears to have produced a flexural moat around it, which shows up most dramatically as a negative gravity ring (ibid). Many ancient fluvial valley networks, which likely formed during an early wetter and likely warmer period on Mars, flowed down the present largescale topographic gradient, further arguing that Tharsis loading was very early. If the load is composed of magmatic products as suggested by fine layers within Valles Marineris,

MARS

water released with the magma would be equivalent to a global layer up to 100 m thick, which might have enabled the early warm and wet Martian climate (Golombek et al. (2001), Golombek (2005)). The largest tectonic feature on Mars is Valles Marineris. Recently a new interpretation of Valles Marineris origin has been proposed by Montgomery et al. (2009). They conclude that the generally linear chasmata of Valles Marineris reflect extension, collapse, and excavation along fractures radial to Tharsis, either forming or reactivated as part of one lateral margin of the Thaumasia gravity-spreading system. The compressional mountain belt defined by the Coprates Rise and Thaumasia Highlands forms the toe of the “mega-slide”. Topographic observations and previous structural analyses reveal evidence for a failed volcanic plume below Syria Planum that could have provided further thermal energy and topographic potential for initiating regional deformation, (ibid). Higher heat flow during Noachian time, or geothermal heating due to burial by Tharsis-derived volcanic rocks, would have contributed to flow of salt deposits, as well as formation of groundwater from melting ice and dewatering of hydrous salts. According with these authors (Montgomery et al. 2009) connection of overpressured groundwater from aquifers near the base of the detachment through the cryosphere to the Martian surface created the outflow channels of Echus, Coprates, and Juventae chasmata at relatively uniform source elevations along the northern margin of the “megaslides”, where regional groundwater flow would have been directed toward the surface. This hypothesis provides a unifying framework to explain the relationships between the rise of the Tharsis volcanic province, deformation of the Thaumasia Plateau, and the formation of Valles Marineris and associated outflow channels (Montgomery et al. 2009). Valles Marineris underwent a complex evolution, due to erosion processes. The Valles Marineris walls in the Tharsis region of Mars have

MARS

a relief up to 11 km in the central parts of a 4000-km-long system of troughs that lie just south of the Martian equator. Lucchitta (1979) attributes the present configuration of the Valles Marineris walls to erosional scarp retreat, recognizing two major types of walls (Lucchitta et al. 1992): spur-and-gully morphology, landslide scars, and small-scale talus slopes. Gullying probably implies some kind of vertical erosion and longitudinal waste transport by fluids or viscous interstitial material, probably ice Lucchitta (1979), related to the widening of the Central Valles Marineris troughs during the late Hesperian (Lucchitta et al. 1992), and to the emplacement of interior layered deposits.

The relative age of different parts of the Martian surface was estimated through crater counting, as older surfaces have been exposed longer to meteoric bombardment and have thus a higher crater density. Three broad epochs have been identified in the planet's geologic timescale, which were named after places on Mars that belong to those time periods. The precise timing of these periods is not known because there are several competing models describing the rate of meteor fall on Mars (see e.g. Hartmann & Neukum (2001)), so the dates are approximate. From oldest to youngest, these periods are the Noachian epoch (named after Noachis Terra), in which the oldest extant surfaces of Mars formed between 4.6 and 3.5 billion years ago; the Hesperian epoch (named after Hesperia Planum), marked by the formation of extensive lava plains 3.5 to 1.8 billion years ago; and the Amazonian epoch (named after Amazonis Planitia), from 1.8 billion years ago 1.8 to present.

3.5 Weather and Climate

In the northern and southern hemispheres CO₂ begins to condense out of the atmosphere at high latitudes in autumn as the temperatures drop below the freezing point of CO₂. The CO₂ forms a snow cover on top of the perennial ice cap and the surrounding terrain. Throughout the period of deposition, the frost line migrates from the polar regions towards the equator and reaches mid-latitudes in late winter (James, et al., 1992). During the northern spring the CO₂ seasonal cap covering the north polar ice cap recedes, and the perennial H₂O cap emerges gradually until the last CO₂ is gone (Cantor, et al., 2001). In the southern hemisphere the CO₂ does not disappear completely but continues to cover the south polar ice cap. However, recently H₂O has been observed in gaps in the CO₂ cover, which indicates interannual variation in the coverage of the CO₂ snow. The timing of the recession of the CO₂ cap varies, which is a sign of interannual variability in the annual cycles of the volatiles in the atmosphere i.e. CO₂ and H₂O. (Cantor, et al., 1998), (James, et al., 2001), (Cantor, et al., 2001), (Calvin, et al., 2004). Global dust storms have been observed to occur repeatedly, but not every year (Kahn, et al., 1992). The global dust storms seemingly result from growth and coalescence of several local dust storms. They rapidly grow due to a positive dynamic feedback involving the intensification of winds due to heating of dust suspended in the atmosphere, and raising of more dust by the intensified winds (Zurek, et al., 1992). All of the observed global dust storms and the largest local ones have occurred during southern spring and summer, and originate in the south subtropical regions of Mars (Zurek, et al., 1992). The SHARAD subsurface sounding radar on MRO, endowed with a tenfold-better resolution compared to MARSIS, provided evidence that Mars' climate undergoes dramatic periodic changes and may now be in a warming trend (Phillips et al.

2008). This can be seen in *Figure XII*, showing a radar cross-section of Mars' north polar ice cap acquired by SHARAD: ice layering shows rhythmic cycling between bundles of dust-containing layers and interspersed clean ice, reflecting changes in environmental conditions during deposition. The driving force for the climate changes appears to be the large variations in Mars planetary motions. As with Earth, Mars' orbit is eccentric, its rotational axis precesses, and especially, its obliquity (axial tilt) oscillates. At low obliquity, less sunlight falls on polar regions, which accumulate snow. At high obliquity the poles receive more sunlight and the equator less, so snow migrates to equatorial regions. At present the obliquity of Mars is calculated to be roughly 25° and decreasing, indicating that in (geologicly) recent times the axial tilt was substantially larger and ice would be expected near the equator.

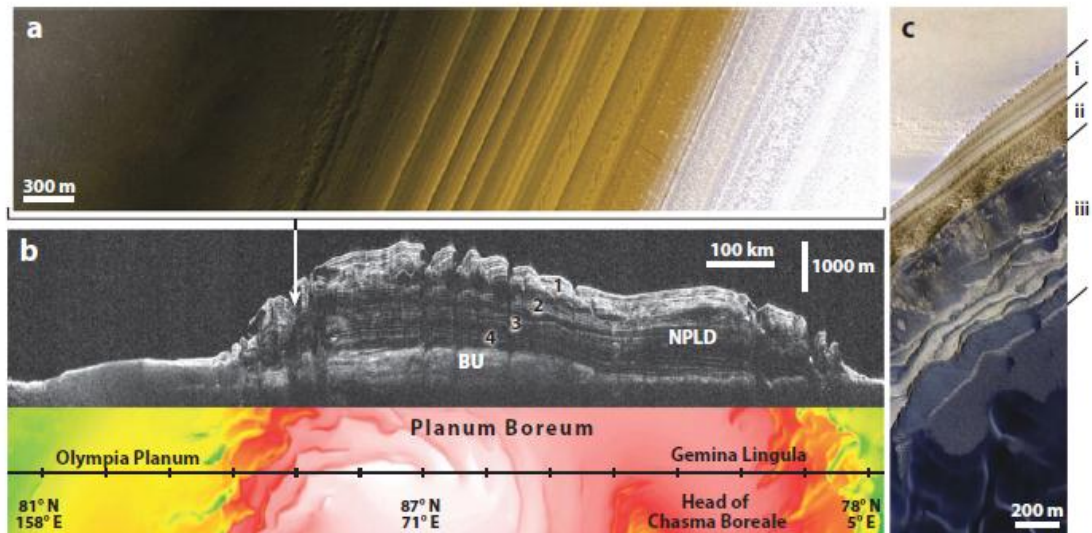


Figure XII North polar stratigraphy from HiRISE imaging and SHARAD radar. (a) HiRISE false-color image PSP 008936 2660, at $144^\circ\text{E } 86^\circ\text{N}$, showing typical exposures of layers in trough (downhill, left) also covered by radargram. (b) Radargram from SHARAD orbit 5192 with associated ground track. Time-to-depth conversion assumed a subsurface permittivity of three. Reproduced from Phillips et al. (2008) with permission from AAAS. Location of trough shown in (a) is indicated. (c) HiRISE false-color image PSP 001593 2635, at $119^\circ\text{E } 83.4^\circ\text{N}$, showing scarp with transition in layering from smooth (i), to polygonally fractured (ii), to the sand-rich basal unit (iii).

MARS

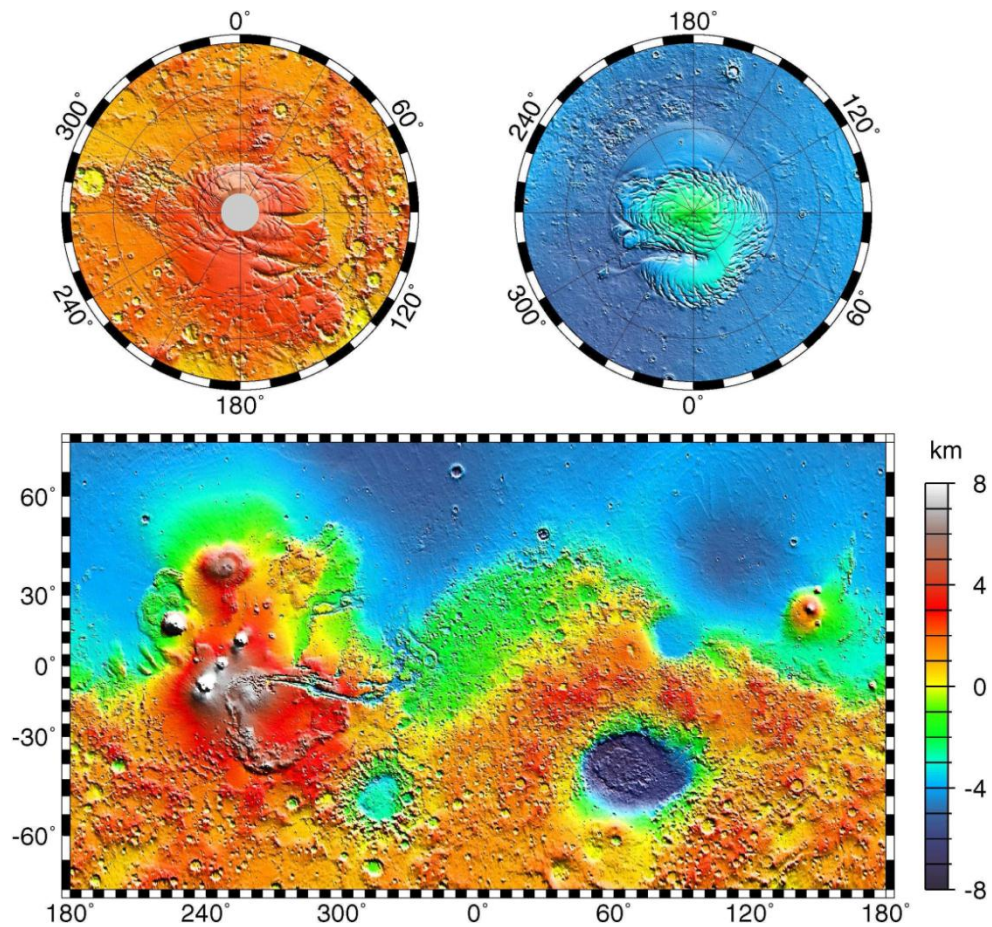


Figure XIII Topographic maps of Mars based on data from the Mars Orbiter Laser Altimeter (MOLA). The colour bar indicates the topographic height in kilometers above the areoid (the equipotential surface which is equivalent to the “mean sea level” on Earth). The latitude and longitude refer to an areocentric coordinate convention with east longitude positive. Image credit: MOLA Science Team. Lower panel: Mercator projection map covering the latitudes between 70°S (indicated by minus sign) and 70°N. The Martian dichotomy is clearly seen with the distinct division between the low-lying smooth young plains of the northern hemisphere and the cratered highlands in the South. Prominent features seen are the deep canyon system Valles Marineris (10-20°S, 265-325°E); the impact basin Hellas (45°S, 70°E); and the volcanic highlands Tharsis (equator, 220-300°E) with the largest volcano in the Solar System Olympus Mons to the northwest (18°N, 225°E). Upper right: Polar stereographic map centered around the north pole. The light blue and green area is the north polar ice cap, which lies several km higher than the surrounding smooth terrain. The north polar cap is cut through by a deep gorge named Chasma Boreale. Around the edges of the polar cap a spiral pattern is seen which consists of flat plateaus and steeper scarps. The center of the ice cap is very smooth and almost devoid of craters indicating a very young surface. Upper left: Polar stereographic map centered around the south pole. The south polar ice cap and the polar layered deposits are seen as the red area surrounded by orange. Note that the spiral structures close to the pole are similar to the features on the north polar cap. The grey area indicates insufficient data.

MARS

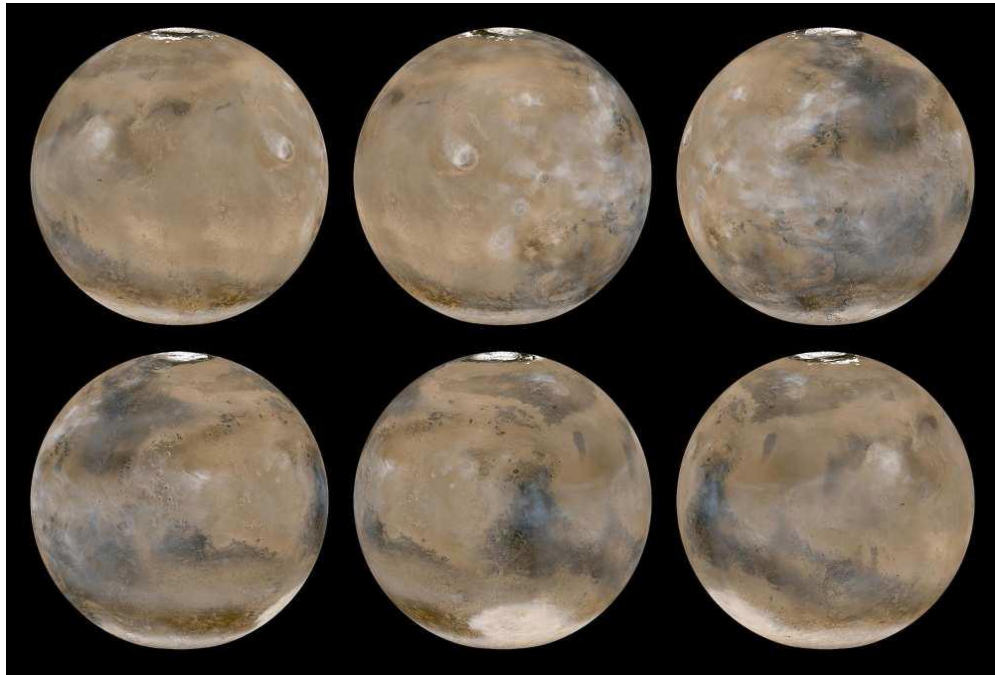


Figure XIV *The Mars Orbiter Camera (MOC) has since 1999 daily recorded images of the weather patterns of the planet. The Figure shows six different views composed of 24 images of Mars acquired on February 14, 2003, when it was in the middle of the summer on the northern hemisphere. Water ice clouds can be seen around the equator and the lower latitudes, and orographically induced water ice clouds can be seen hanging over the highest points in the topography, which are the large volcanoes in the Tharsis and Elysium regions (upper left and center and lower right). The north polar ice cap is fully exposed in the northern hemisphere, whereas the southern polar regions are covered by a seasonal layer of CO₂ frost. The frost extends itself furthest to the north in the Hellas Basin, where the lower topography and therefore higher atmospheric pressure in the basin allows the CO₂ to freeze at slightly higher temperatures than elsewhere in the southern hemisphere. Image credit: NASA/JPL/Malin Space Science Systems.*

3.6 Water, Ice, and Permafrost

The atmospheric water vapor varies geographically and in time. An example of water ice clouds can be seen in *Figure XIV*. Both the Viking Mission's Mars Atmospheric Water Detector (MAWD) and Mars Global Surveyor's Thermal Emission Spectrometer (TES) observed the Martian atmospheric water abundance through the Martian seasonal cycle. The MAWD data exists for a period of one Mars year and TES for three years. A repeating dominant feature in the atmospheric water distribution is a large peak in the concentration at high northern latitudes in the northern summer, when the permanent H₂O ice cap is exposed to the atmosphere. This also shows that the northern ice cap is an active water reservoir in the present Martian water cycle.

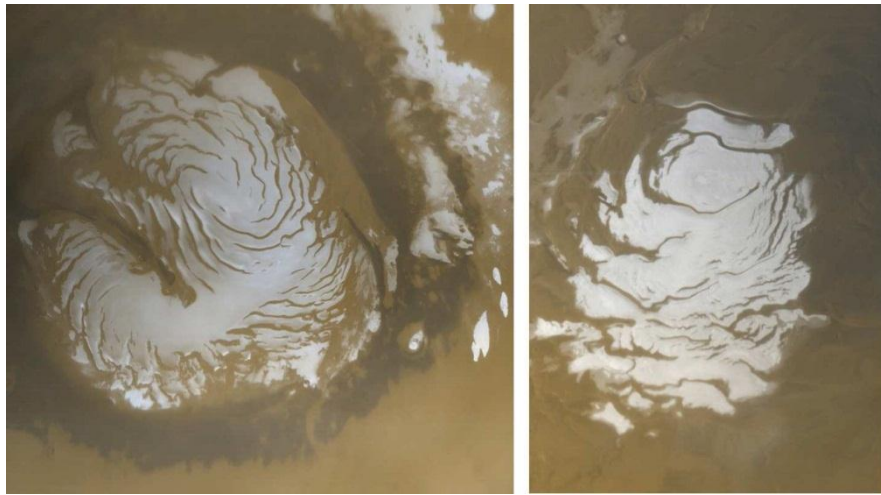


Figure XV Left: *The north polar ice cap in the northern summer time. The white areas are residual water ice that remains through the summer season. The nearly circular band of dark material surrounding the cap consists mainly of sand dunes formed and shaped by wind. The north polar cap is approximately 1100 kilometers across..*

Right: *The south polar ice cap in the southern summer time. The image shows the south polar cap at its minimum extent. Even though it is summer, observations made by the Viking orbiters have shown that the south polar cap remains cold enough for the CO₂ frost to remain. Recent observations however have shown that gaps in the CO₂ frost occur in some years allowing the H₂O ice below to be detected [Bibring et al., 2004]. Image credit: NASA/JPL/Malin Space Science Systems.*

A somewhat smaller peak in the concentration is seen in the southern summer, which can be explained by two possible reasons. 1) The signal in the water vapor may be obscured in the measurements by the heavy planet-encircling dust storms. 2) The southern ice cap may be completely or partly covered by a layer of CO₂ frost, which inhibits evaporation. However, both earth based and satellite measurements have shown that the ice cap may be episodically exposed, and a peak of high water concentration can be present in the atmosphere at the south pole. Studies of the MAWD and TES data indicate that there is a net transport of water from the north to the south during northern summer, which is not balanced by a similar northward transport at other seasons (Jakosky, et al.). The north polar ice cap of Mars (*Figure XV*) is one of the largest reservoirs of water at present. It contains layers of H₂O and CO₂ ice and dust, as seen in *Figure XVI* which reflect the climate changes of the past. The elevation of its highest point relative to its surroundings is 2950 ± 200 m and it covers an area of $1.04 \cdot 10^6$ km² (Zuber, et al., 1998). The large areas at the top of the ice cap are smooth and fresh-looking, indicating an active resurfacing process such as a presently occurring net deposition. The MOLA instrument on board Mars Global Surveyor measured the topography of the northern ice cap, and it was calculated by Nye et al (Nye, et al., 2000) that it could not consist of CO₂ ice, as this would have made it flatter, due to the differences in the rheology of H₂O and CO₂ ice.

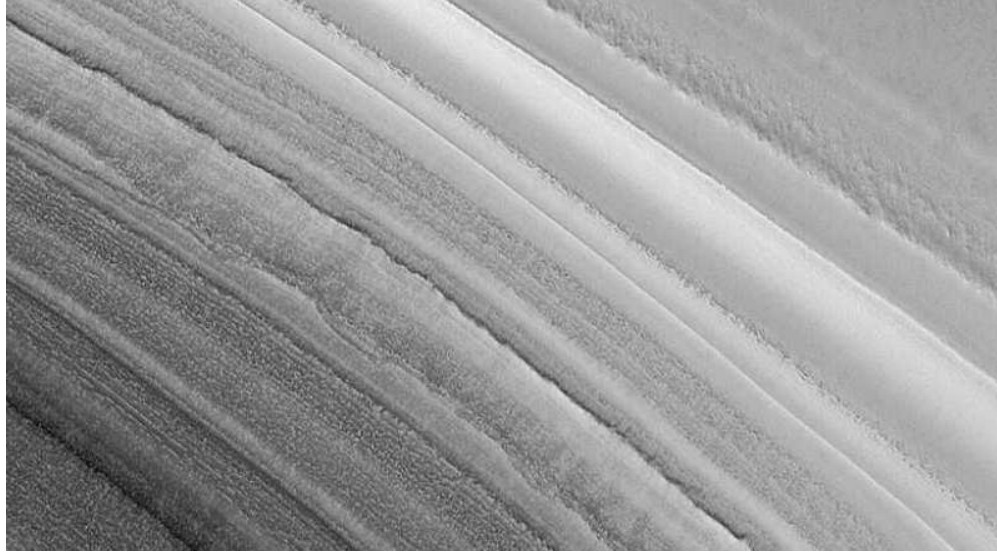


Figure XVI Layers seen in a slope of the north polar ice cap at 81.5_N in late northern spring. The image is taken by the Mars Orbiter Camera (MOC) and covers an area of approximately 3 km in width. The layers consist of H₂O and CO₂ ice and dust. The brightest areas in the image are covered by frost. Image credit: NASA/JPL/Malin Space Science Systems.

3.7 Missions

Past Missions

Modern exploration of Mars began with the Mariner 4 mission in 1965 and was followed by Mariner 6 and 7, which all indicated a cold, dry, and dead planet. This picture changed with the arrival of Mariner 9 in November 1971 as the first artificial satellite of Mars. The mission revealed the geological diversity of the planet and revived the interest for its biological potential (Carr, 1996). Between 1971 and 1973, the Soviet Union sent the missions Mars 2-7, where only Mars 5 lasted long enough to send back high quality data and pictures.

The next major step was the Viking mission, which consisted of two spacecraft, each comprising an orbiter and a lander which all arrived in

MARS

1976. The primary goal of the mission was to look for signs of life. The two landers conducted three biology experiments designed to detect possible signs of biological activity, but found no evidence for this. They returned data on the organic and inorganic chemistry of the soil, the composition of the atmosphere, and the local meteorology. The orbiters systematically photographed the surface, mapped its thermal properties, and measured the water content of the atmosphere in space and time. The Viking mission was planned to last 90 days, but the landers continued to transmit data back to Earth until 1980 and 1982, respectively, and the orbiters until 1978 and 1980 [NASA's Mars Exploration Program, 2005].

After the Viking Missions a series of missions was launched, but only a small amount of data came out of the attempts. In 1988 the Phobos 1 and 2 missions were launched with the aim of studying Mars' satellite Phobos, but both were lost during the mission. However, some data of thermal and spectral properties of the Martian surface and on the erosion of the upper Martian atmosphere by the solar wind resulted from the mission (Carr, 1996).

In 1997 the Mars Pathfinder landed on Mars, carrying the small Sojourner Rover. During the mission scientific studies were made of the geology and geomorphology, mineralogy and geochemistry, magnetic properties, and surface material properties [JPL Mars Pathfinder, 2005]. The atmosphere and local meteorology was also studied through measurements of the varying temperature, pressure and near-surface wind. In order to get more precise data for studies of the rotational and orbital dynamics, the rotation of Mars was measured via the radio communication signals between Pathfinder and Earth.

In 1999 two spacecraft, Mars Climate Orbiter and Mars Polar Lander, were lost on arrival. The orbiter was supposed to study the weather and atmosphere and work as a communication relay for the lander. The

lander should have studied surface meteorology as well as examined samples collected from the surface for water content and chemistry analyses [NASA's Mars Exploration Program, 2005].

Current Missions

Currently there are four satellites orbiting Mars and two rovers driving on the surface of the planet, which is an unprecedented high number of missions occurring simultaneously .

Mars Global Surveyor has been orbiting Mars since 1997 and has delivered several groundbreaking new findings from its low-altitude near polar orbit. The mission has studied the entire Martian atmosphere, surface and interior. The Mars Orbital Camera (MOC) has taken high-resolution images of gullies and debris flows, suggesting that occasional sources of liquid water were once present at or near the surface of the planet. The Mars Orbiter Laser Altimeter (MOLA) has provided highly accurate topography data. Particularly the elevation measurements of the North Polar Ice Cap have led to new information regarding the structure, volume and extent, as well as the composition of the ice cap.

The 2001 Mars Odyssey spacecraft has provided measurements of thermal and radiative properties of the surface materials, enabling the creation of maps of minerals and chemical elements.

In January 2004 two robotic rovers landed on opposite sides of the planet. since then, Spirit and Opportunity have travelled several km across the Martian landscape studying the geology and making atmospheric observations. The rovers have made detailed microscopic images of rocks and soil and measured their elemental and mineralogical composition by use of four different spectrometers. On a robotic arm they carry a special rock abrasion tool allowing studies of the interiors of the rocks found on the surface. Bright patches of soil have been found to consist of evaporative minerals indicating deposition

MARS

in an aqueous environment. Another indication that Mars had surface water in the past is the finding of layered rocks which may be sediments from running water in the past.

Mars Express arrived at Mars in 2003 and has since then been conducting investigations about the geology, atmosphere, surface environment, the history of water and potential for life on Mars. The mission is in particular dedicated to the search for sub-surface water from orbit.

The most recent spacecraft in orbit around Mars is the Mars Reconnaissance Orbiter, which arrived in March 2006. It carries a camera with the highest resolution so far, which will provide detailed images of the surface with the purpose of learning more about the planet as well as providing context for the rovers and determine whether future possible landing sites are smooth and safe. Studies will also be made of the transport of water and dust in the atmosphere, which will provide more insight into the climate dynamics on Mars.

3.8 The Atmospheric and Surface Temperature

The temperature on both the surface of a planet and the atmosphere is ultimately determined by the heating from the sun and the cooling to space. Heating takes place as a result of absorption of visible sunlight in the atmosphere and in the ground.

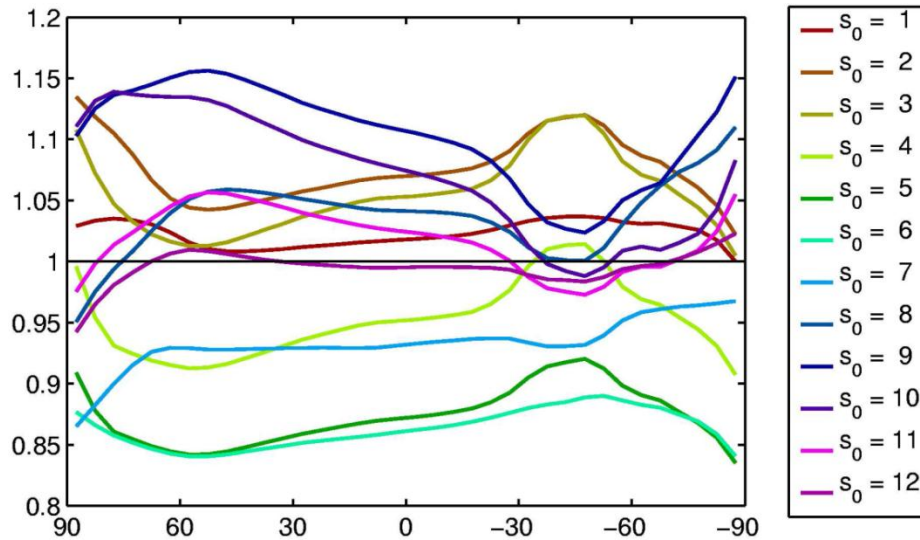


Figure XVII Illustration of the seasonal variation in the zonally averaged surface pressure relative to the annual average as a function of latitude (horizontal axis) and time of the year (see legend for season numbers).

Cooling is caused by direct infrared cooling of the surface and indirect infrared cooling from the atmosphere on Mars mainly in the 15 μm band in CO_2 . To a first order the cooling is relatively uniform with latitude but the heating is a strong function of latitude, leading to a net heating in the equatorial region and a net cooling in the polar regions which can be seen in the annual average atmospheric temperatures in *Figure XIX*. Due to atmospheric exchange of heat and energy across latitudes, the temperature difference between the high and low latitudes observed on Mars are much smaller than if the atmosphere was static and transport did not occur.

In the GCMs, which are the basis for the MCD the radiative transfer takes into account the effects of the presence of CO_2 gas and mineral dust suspended in the air at both solar and infrared wavelengths (Forget, et al., 1999). The radiative effects of water vapor and water ice particles were neglected because of the low vapor column abundance and the limited occurrence of water ice clouds in space and time. The

effect of CO₂ condensation and sublimation is included in the calculation of the energy balance. CO₂ condenses when the local temperature drops below the condensation temperature and releases the corresponding latent heat, and can conversely sublimate when it is heated. The sedimenting CO₂ ice particles can thus sublimate when they reach warmer atmospheric layers as they descend to the ground.

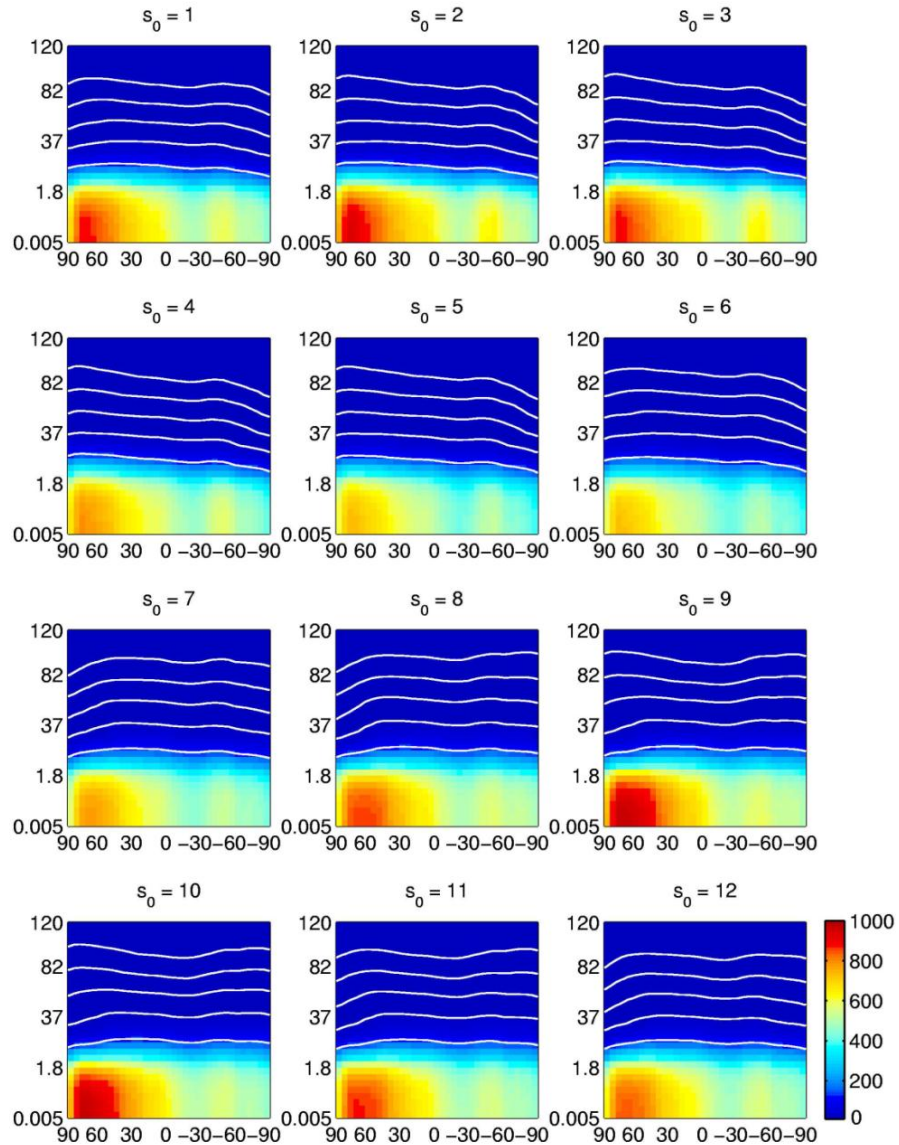


Figure XVIII: Atmospheric pressure data for the Viking dust scenario from MCD. The horizontal axis represents the latitude [degrees] and the vertical axis the altitude above the Martian surface [km]; note that the vertical scale is non-linear. The colour bar shows the atmospheric pressure [Pa]. The number above each plot indicates the season number, each of which lasts 30_Ls. The white contour lines represent pressures of 0.01, 0.1, 1, 10, and 100 Pa (pressures decreasing with altitude).

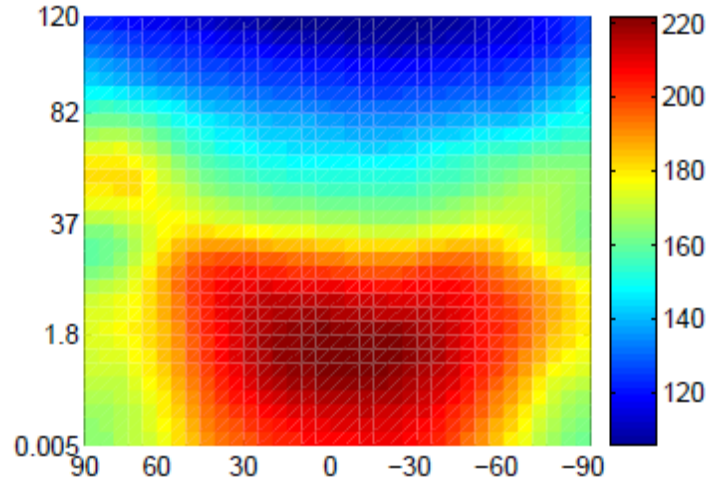


Figure XIX: Zonally averaged annual mean atmospheric temperature data from the MCD, the colour bar indicates the temperature in [K]. The horizontal axis shows the latitude [$^{\circ}$] and the vertical axis the altitude [km] on a non-linear scale.

In *Figure XX* the diurnally averaged atmospheric temperature is shown as a function of latitude, altitude, and time of the year. The heating at north polar high altitudes due to convergence of air during the northern winter is clearly seen. It can also be seen that the seasonal coverage of CO₂ frost on the surface causes cold temperatures in the lower atmosphere above the polar regions until the frost has disappeared by early northern summer ($s_0 = 2; 3$) and early southern summer ($s_0 = 8; 9$). The calculated surface temperature is governed by the balance of the incoming fluxes of energy and heat (solar insolation, thermal radiation from the atmosphere and the surface itself, and turbulent fluxes) and the thermal conduction in the soil (Forget, et al., 1999).

In the GCMs the thermal conduction in the soil was parameterized by a 11-layer soil model (Hourdin, et al., 1993) with a vertically homogeneous soil and a spatially varying thermal inertia and albedo based on Viking IRTM observations.

MARS

The zonally averaged mean diurnal surface temperature $T_s(\phi;L_s)$ is shown in *Figure XXI*. The effect of the eccentricity of Mars' orbit is seen in the difference in the peak summer temperature on the two hemispheres.

A rapid increase in the polar surface temperature can be seen after the disappearance of the seasonal CO_2 frost at the beginning of the summer on both hemispheres. The atmospheric and surface temperatures have been extracted from the MCD, averaged and stored for later use.

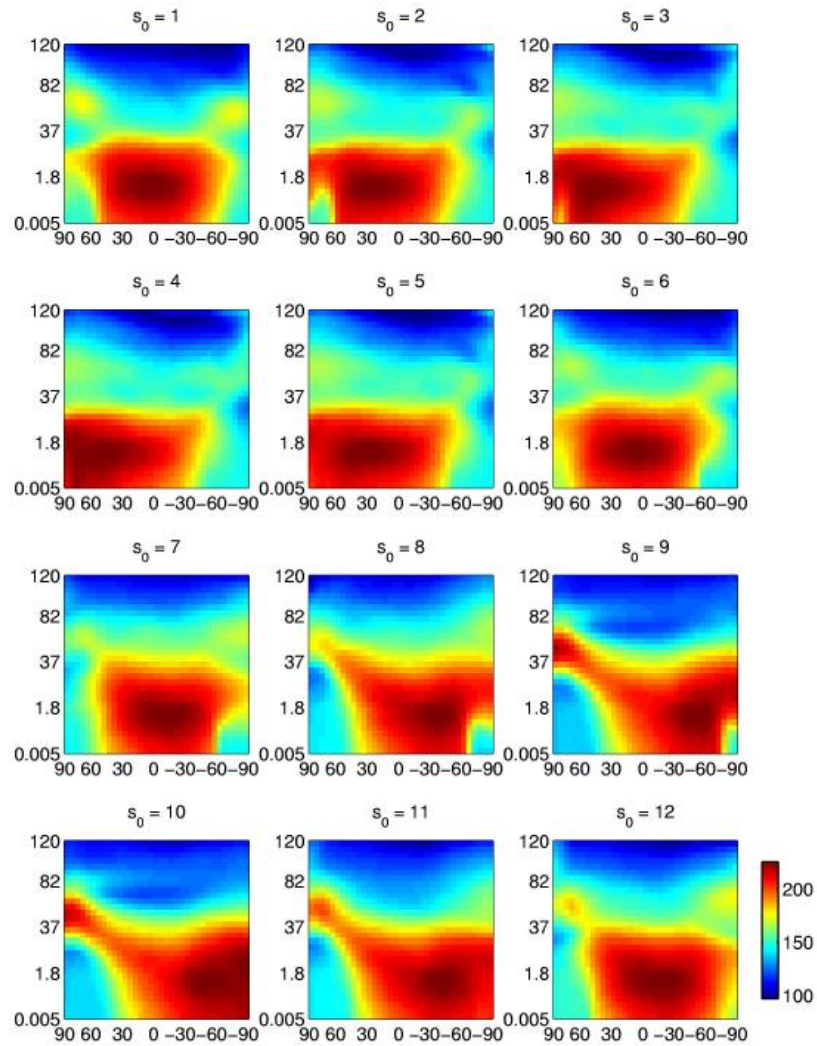


Figure XX: Zonally averaged diurnal mean atmospheric temperature data from the MCD, the colour bar indicates the temperature in [K]. The horizontal axis shows the latitude [$^{\circ}$] and the vertical axis the altitude [km] on a non-linear scale.

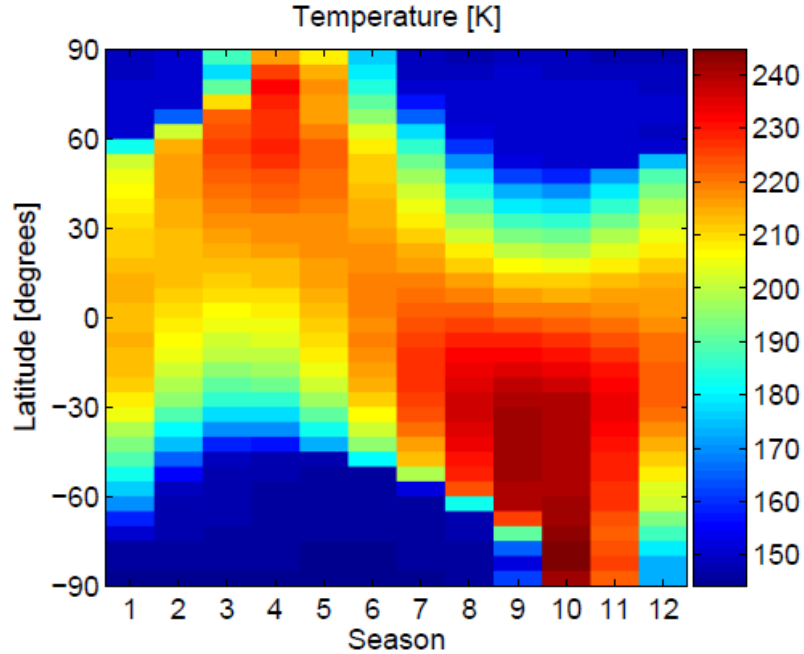


Figure XXI: Zonally averaged diurnal mean surface temperature data from MCD, the colour bar indicates the temperature in [K]. The horizontal axis show the season number and the vertical axis the latitude [°].

3.9 The Ground Ice in the Regolith

The Mars Odyssey Gamma Ray Spectrometer suite of instruments has detected the water content of the near subsurface on Mars (Feldman, et al., 2002), (Mitrofanov, et al., 2002), (Boynton, et al., 2002), (Mitrofanov, et al., 2003). The original data set consisted of binned values in a grid that is resolved in 5° in latitude and has a varying resolution in longitude in terms of degrees but quite similar in terms of length. If the binning had been equally spaced in longitude, the grid would be too narrow to allow for a statistically valid number of data points in the binning of data. The data is a combined set of summertime measurements at both northern (Feldman, et al., 2004) and southern high latitudes as well as

MARS

the average of the whole data set at mid to equatorial latitudes. This is needed because during the winter the CO₂ frost cover obscures the measurements, wherefore the map in *Figure XXII* is not representative for a single time shot of Mars, but represents what the neutron detector would measure in a frost-free situation.

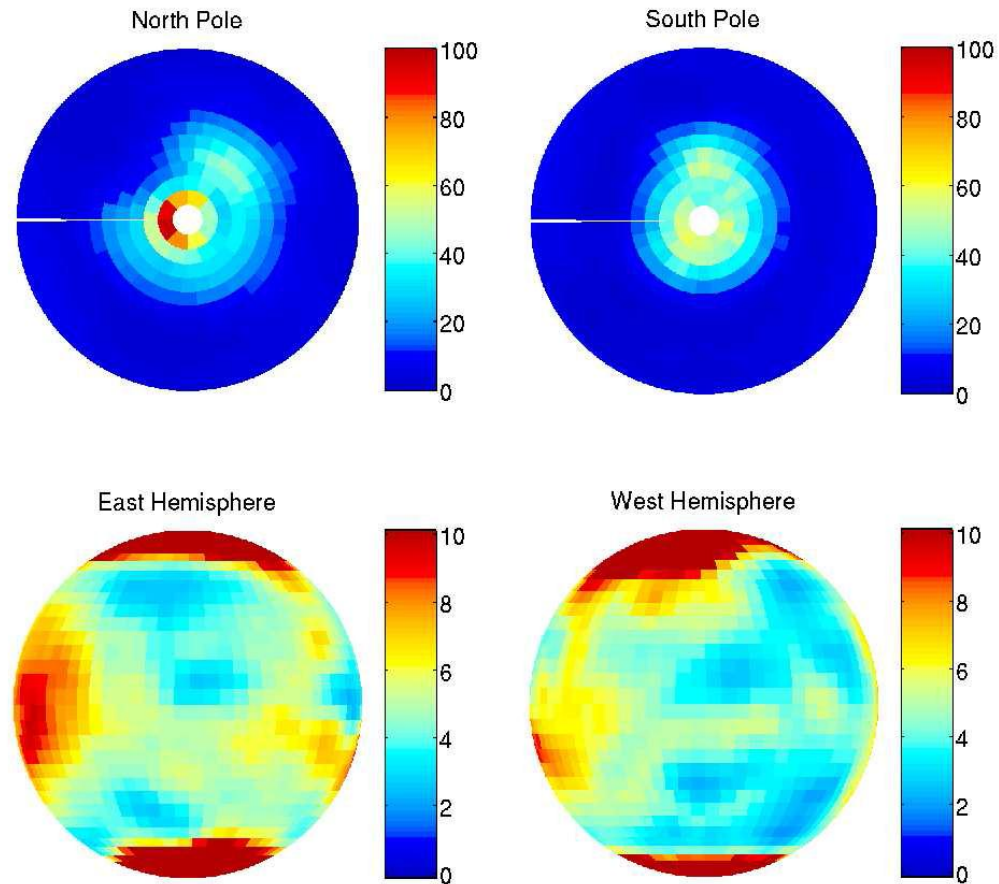


Figure XXII Ground Ice percentages from the MGS Neutron Spectrometer. The colour bars show the values of ground ice estimated from water-equivalent-hydrogen in mass-%. Notice the different scales for the polar- (upper panel) and low-latitude plots (lower panel). For the latter two, the scale is saturated for values greater than 10%. The globes each show a part of the Martian surface. UL: The north pole region down to equator. The 0°meridian is pointing from the pole to the left. UR: The south pole region down to equator. The 0°meridian is pointing from the pole to the left. LL: The eastern hemisphere. The 0°meridian is located along the left edge of the globe. LR: The western hemisphere. The 0°meridian is located along the right edge of the globe.

3.10 The present climate on Mars

The investigations of the last 40 years of Mars exploration have painted a picture of a more dynamical climate than previously thought. The seasonal variations on Mars are, compared to the other planets in the solar system, much like the variations on Earth.

One Martian day (sol) is 88775 seconds compared to 86400 seconds on Earth and one Martian year is 669 sols, equivalent to around 2 Earth years.

In this section, I will describe the dynamics of the present Martian climate.

3.10.1 Global circulation

The Martian atmosphere consists mostly of CO₂ with a total atmospheric pressure around 700 Pa, depending on altitude and season. This is about 0.6% of Earth's atmosphere. The atmosphere of Mars is relatively thin, and pressure on the surface varies from around 30 Pa on Olympus Mons's peak to over 1,155 Pa in the depths of Hellas Planitia, with a mean surface level pressure of 600 Pa, compared to Earth's sea level average of 101.3 kPa. However, the scale height of the atmosphere is about 11 kilometers, somewhat higher than Earth's 7 kilometers. The atmosphere on Mars consists of 95% carbon dioxide, 3% nitrogen, 1.6% argon (Owen 1992).

The Martian lapse rate and Planetary Rossby number are much different than the terrestrial values due to the different composition and dynamics of the atmosphere.

Because of the large seasonal temperature variations, the CO₂ condenses out of the atmosphere in the respective hemispheric winter seasons and forms a seasonal CO₂ layer in the polar regions.

This phenomenon can be seen on *Figure XXIII*.

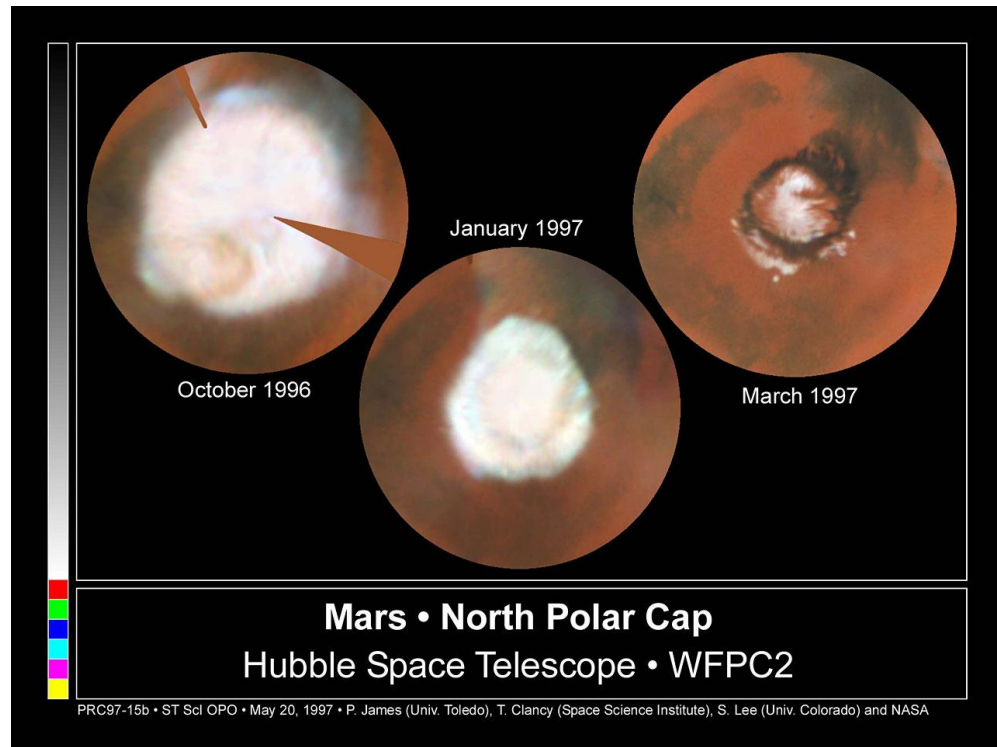


Figure XXIII: *This series of pictures captures the seasonal retreat of Mars' north polar cap. (NASA)*

Due to this, the atmospheric pressure varies around 20% (Kieffer, et al., 1992). Water vapor is present in the atmosphere with a typical partial pressure of 0.1 Pa. The atmospheric water content varies with the seasonal supply and removal from the polar caps, exchange with adsorbed and condensed water in the regolith, and the changes in the global wind pattern (Kieffer, et al., 1992). On Earth, a relatively dense atmosphere maintains a greenhouse effect which alters the global mean temperature. Furthermore, a global ocean acts as a temperature buffer because of the vast amounts of water with high specific heat capacity. On Mars, seasonal changes in insolation occur more drastically and abrupt because of the low density atmosphere with low heat capacity and the lack of an ocean. Thus, the diurnal and seasonal temperature variations are much larger than on Earth. The maximum diurnal near-surface

MARS

atmospheric temperature range is around 30 K on Earth and 60 K on Mars. The daily averages of surface air temperature during the seasons range up to 90 K in the polar regions on Mars (Kieffer, et al., 1992), but only around 50 K on Earth.

On Mars, the global circulation is much different that on Earth. On Mars, strong zonal mean mid-latitude winds increase with height to strong jet streams at an altitude of 30 km. These are eastward in all seasons except midsummer where they are westward in the tropics and mid-latitudes.

On Earth, the zonal mean winds are weaker and they occur on lower latitudes and altitudes (Leovy, et al., 1973). These differences are associated with the larger temperature gradient on Mars which occur because of the lack of a global ocean as well as the much shorter radiative time scale (Leovy, 2001). An important part of the low-latitude meridional circulation on Earth is the Hadley circulation.

On Mars, similar Hadley circulation occurs, but the cells are much stronger and the branches are much further away from equator. Because of the large seasonal differences in insolation, the Hadley circulation is stronger during northern winter than southern winter (Haberle, et al., 1993).

Furthermore, other systems such as mid-latitudinal planetary waves and smaller weather systems near the edges of the polar caps exist in the Martian atmosphere (see

Figure XXIV) as well as thermal tides and Kelvin waves also contribute to the dynamical atmospheric circulation (Leovy, 2001).



Figure XXIV: A dust storm on Mars (top) and on Earth (bottom). Even though there are many differences between the two atmospheres, similarities in the dynamics can be observed. (NASA/JPL/MSSS)

3.10.2 Stability of H₂O

Stability of H₂O on Mars is strongly influenced by a combination of low temperatures and a low atmospheric pressure. *Figure XXV* shows the phase diagram of H₂O.

The typical regions of temperature and pressure for Earth, Mars and Venus are shown. It can be seen that under the present Martian climate, water is usually only stable in solid or in vapor form and exists mainly without a transient liquid phase. On Earth, H₂O occurs in all phases whereas on Venus, H₂O only exists in the vapor phase because of the high pressure and temperature.

Furthermore, due to the low atmospheric pressure, the boiling point of water on most of Mars is 2-7 K above the melting point (Hecht, 2002). In contrast, liquid water on Earth exist in a range of 100 K at sea level. It

MARS

has to be noted that this only accounts for pure water, and not e.g. acidic or salty water.

Non-pure water will act in a different way, e.g. salty water has a lower freezing point than pure water.

Studies in stability of liquid water on Mars conclude that ice is metastable on the surface (Hecht, 2002).

This means that liquid water is evaporating or freezing slowly compared to the rate of which it flows across the surface.

Thus, water from a melting ice deposit could flow in contemporary times before freezing and evaporating under the proper conditions.

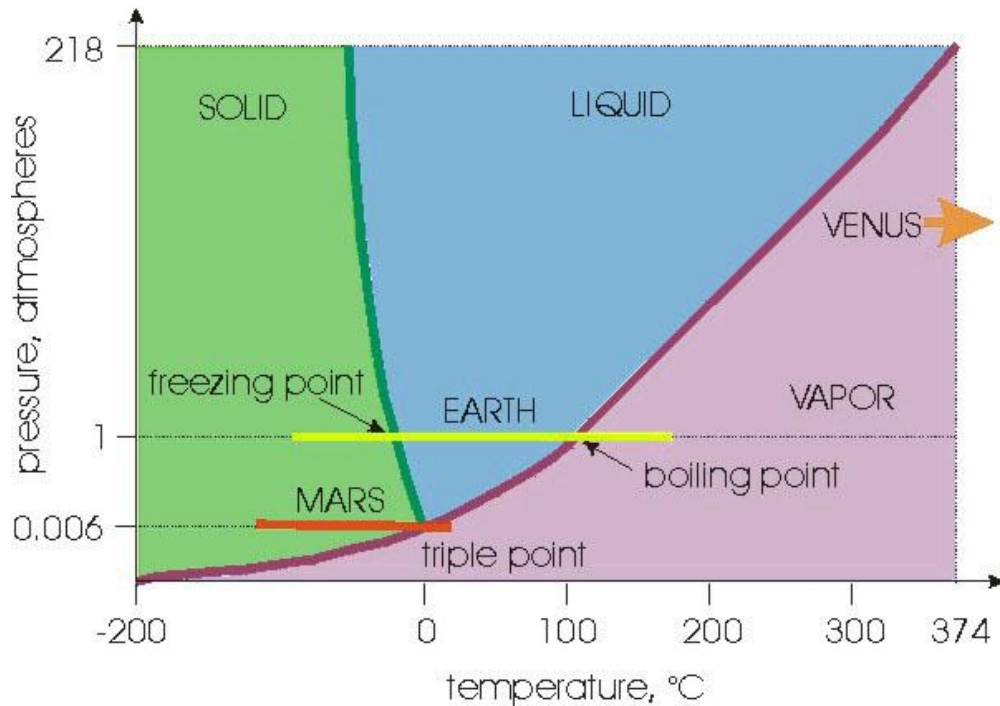


Figure XXV: Phase diagram of H₂O showing the dependency of pressure and temperature on H₂O. The typical regions of pressure and temperature for Earth, Mars and Venus is shown. It can be seen that under present Martian pressure conditions, water is usually only stable in solid or in vapor form.

3.10.3 Polar Layered Deposits

In the current climate, the polar regions are the planet's largest cold trap. Thus, the polar regions currently contain the largest known H₂O reservoirs on the planet. The polar layered deposits (PLD) have a size of around 1000 km in the north and 1500 km in the south.

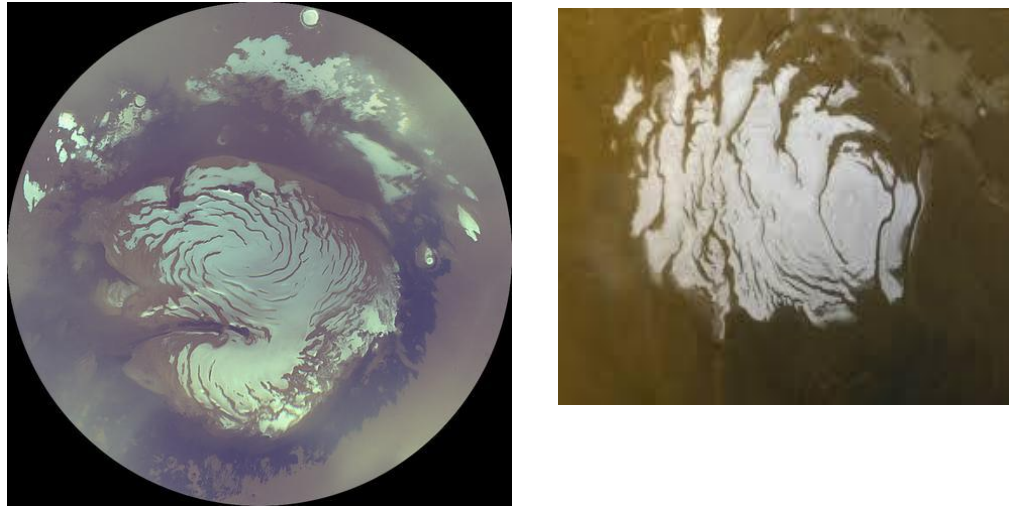


Figure XXVI: *Left:* The North polar layered deposits in October 2006 as seen from the Mars Color Imager instrument aboard NASA's MRO. (NASA/JPL/MSSS). *Right:* The residual CO₂ ice on the South polar layered deposits (NASA/JPL)

They consist of layers of H₂O dust and CO₂ deposited through millions of years (Hvidberg, 2005). The same sequence of layers have been observed several places on the north PLD (Fishbaugh, et al.) and the rhythmic layering of the PLD strongly suggest that climatic and orbital changes have influenced their formation (Murray, et al., 1972). Average deposition rates above the polar caps are thought to be in the order of 0.1-1 mm/year (Laskar, et al., 2002), but detailed knowledge about the mass balance of the PLD is still to be investigated. The same accounts for the possibility of ice flow in the PLD. This has been investigated by e.g. (Hvidberg, 2003) and (Fisher, 2000) and flow rates of 0.1-1 mm/year

have been proposed but it still remains unclear whether the PLD flow or not. Even though there are lots of significant differences between the northern and the southern polar deposits, most scientists agree on the following stratigraphy from the surface and downwards: (1) seasonal frost, (2) residual ice, (3) layered deposits, and (4) Martian surface.

Figure XXVI shows the residual caps in the north and south polar regions, respectively. The north cap has a counterclockwise spiralling pattern of troughs and scarps which exposes extensive layering, while the south residual cap has a clockwise pattern. The origin of these patterns is not fully understood, but investigations by e.g. (Howard, 2000), (Fisher, 1993) and (Hvidberg, 2003) indicate that katabatic winds or combinations of flow, sublimation and accumulation could be responsible for the distinctive pattern. The residual caps are very different between the two hemispheres. In the northern polar region, the residual ice is made of H₂O which covers and grades into the underlying layered deposits. The albedo of the residual ice is very high and is consistent with ice mixed with a small fraction of dust (Kieffer, et al., 1992) (Thomas et al., 2000). In the south polar region, the residual cap consists of a »8 m thick layer of CO₂ ice that only covers a small part of the underlying H₂O ice and layered deposits, which are covered by a mantle of one grained material, probably dust (Thomas et al., 2000), (Titus et al., 2003), (Vasavada et al., 2000). The results from Omega and MGS-TES confirm that the north PLD residual cap consists mainly of H₂O ice and that this giant water reservoir exchanges water vapor with the atmosphere. Every summer, a large amount of water vapor sublimates from the polar layered deposits, and increases the amount of water vapor in the atmosphere with one order of magnitude. During the fall and winter seasons, the water vapor condenses out of the atmosphere and into the cold traps in the ground ice deposits and the polar regions. In the south polar region, the amount of water vapor in the atmosphere

is much smaller during the summer period, indicating that the dust layer influences the sublimation rates of the underlying H₂O cap. The ages of the north and south polar layered deposits are probably also different. In the north, the PLD overlies a region thought to be around 2-3 Ga old. In the south, the PLD lies on much older ground, thought to be around 4 Ga old (Clifford, et al.).

Both the north PLD and the south PLD are covered by a seasonal cover of CO₂ in the winter season when the reduction in insolation causes the surface temperature to fall and CO₂ to condense (Leighton, et al., 1966).

This can be seen on *Figure XXIII* as described earlier, the pictures show the seasonal retreat of the CO₂ layer. In the northern hemisphere winter time, the CO₂ layer has condensed out of the atmosphere and covers most of the polar region, whereas in the northern summer time, the layer has evaporated back into the atmosphere again.

3.10.4 Dust cycle

The global distribution of dust and its redistribution through surface-atmosphere interactions are important factors in both the Martian geology and climate, and thus play an important role in moderating the global climate system.

The main parameters in the global dust circulation are dust storms and the more local dust devils. However, dust storms are seen both "locally" with sizes of 10⁴-10⁶ km² and on global scale.

Dust devils are usually on the order of tens of meters, but have been observed to be up to 1 km across and above 6 km in the vertical extent (Edgett, et al., 2000).



Figure XXVII: *Global Dust Storm seen from the Hubble Space Telescope. Within 3 months, the storm extended from pole to pole. (NASA)*

Figure XXVII shows the extent of a global dust storm seen by the Hubble Space Telescope. Within 3 months during 2001, the whole planet was covered in a global dust storm extending from pole to pole. The dust particles of sizes around $1\mu\text{m}$ can be lifted around 10-20 km in the vertical by a dust storm. Since it takes days to fall one kilometer for those particles, the decay time of a large dust storm is on the order of months (Pollack et al., 1979), (Smith, 2004) and the effects of dust storms seems to extend as high as 160 km (Keating et al., 1998). Pictures of dust devils and dust devil streaks on the surface can be seen on *Figure XXVIII* and *Figure XXIX*. Lifting of the dust occurs usually by either near-surface wind stress or by convective vortices. Thus, development of dust storms is connected with the local surface winds (e.g. anabatic and katabatic winds) and the global circulation. Since the global circulation has only little interannual variation, the dust storms are usually developed by variations in the local meteorology by different feedback processes (Montabone, et al., 2005). MGS has observed a tendency of dust storms and dust devils on the mid-latitudes on the edge of the

MARS

seasonal polar caps. The dust storms and dust devils also occur on lower latitudes. There seems to be a dusty storm season especially during northern winter around $L_s = 180-270^\circ$ when Mars is approaching perihelion, i.e. is closest to the Sun (Cantor, et al., 2001). These low-latitude storms seem to be generated by the strong seasonal Hadley convection, thermal tides, local wind patterns and local thermal convection (Leovy, et al., 1973). The atmospheric dust, raised by the local and global dust storms and dust devils, has a great impact on the current Martian climate in several different ways. The dust can act as nucleation centers for H_2O ice condensation, and when either hemisphere enters the fall season, these particles will receive an additional coating of frozen CO_2 .



Figure XXVIII: *Dust devil on the floor of Gusev crater, taken by the Spirit Navcam. This dust devil is about 1 km from the rover and is estimated to be at least 95 m high. (NASA/JPL)*



Figure XXIX *Dust devil streaks on the surface around (5.3°S, 343°W) as observed by the MGS MOC camera. The picture is about 3 km across. (NASA/JPL/MSSS)*

This makes the particles heavy enough to precipitate from the atmosphere, thus contributing to the growth of both the seasonal and permanent caps as well as frost on the ground (Pollack et al., 1979). Furthermore, dust in the atmosphere reduces the optical depth and modifies the heat transfer of visible and infrared radiation, thereby affecting the heating rates of both the atmosphere and the planetary surface. As an example, near perihelion where the atmosphere becomes very dusty (optical depth at visible wavelengths ≥ 1), the increased absorption of the solar radiation by the dust increases the mean temperature of around 15 K in the atmosphere (Smith, 2001). In addition, dust deposition and the removal of dust from the atmosphere influence the albedo of the surface and therefore also the daytime surface temperature as well as the local atmospheric convection

(Gierasch, et al., 1972); (Haberle, 1986); (Pankine, et al., 1999) (Basu et al., 2004). On top of the PLD, a thin (μm thick) seasonal layer of dust that extends from the periphery of the polar caps down to a latitude of 40°N/S has been observed. In some regions on Mars there is evidence that local winds remove and redistribute this dust layer (Arvidson, et al., 1983).

In the polar regions, the icy surfaces will experience a change in the albedo, which leads to changes in absorption of the solar radiation and sublimation rate of the PLD since the water vapor released from the surface has to travel through the dusty layer. When the dust is mixed within the PLD, the physical properties of the surface and interior are changed, and this changes the dynamics of the PLD. The size of the dust grains varies much. Remote sensing data by the MGS-TES instrument (Ruff, et al., 2002) as well as in-situ observations by the Sojourner rover and the Mars Exploration Rovers (Moore, 1999); (Herkenhoff, 2004) constrain the size of dust on the surface to fine sand to a range approximately from 1 to $100 \mu\text{m}$. It is clear that dust grains in the atmosphere can be even smaller. Thus, if the dust on the surface of the PLD comes from the atmosphere, it could be around the size of $0.1\text{-}1 \mu\text{m}$. On longer time scales, climatic variations can influence the dust cycle and the amount of material that is deposited and retained by the polar caps since the atmospheric circulation will be moderated. As an example, at low obliquity when the poles are at their oldest, large CO_2 ice caps should be able to persist throughout the year. In this climate scenario, atmospheric pressure may fall to such a low point that dust can no longer be elevated from the surface (Toon, et al., 1980); (Fanale, et al., 1986).

3.11 Terrestrial analogues for Martian ground ice

A possible terrestrial analog for ice covered by a dry layer of dust can be observed in The Dry Valleys in Antarctica. Here, a layer of dry, sandy and rocky soil overlays densely ice cemented soil.

It has been shown that vapor diffusion controls the ice table depth, but it is still unclear how old the ice is. Dating the volcanic ashes in the covering sediments indicate that the ice is more than 8 Myr old (Sugden, et al., 1995). Some thermodynamic modeling of ice sublimation through the sediment states that the ice is much younger with a sublimation rate of 1 m/10,000 years (Hindmarsch, et al., 1998) while other modeling results argue that the transport mechanisms could allow the ice to be stable under the sediments for time scales of millions of years (Schorghofer, 2005).



Figure XXX: Ice table in Beacon Valley, Antarctica. The ice is covered by 15 cm of sandy soil. From Mellon et al. (2004).

Figure XXX shows a picture of the ice in Beacon Valley, Antarctica. Here, a dense ice table is found beneath 15 cm of sandy dry soil. Since no large rocks are present, the ice table parallels the surface. Other pictures show that the presence of rocks will influence the subsurface temperatures, and result in a more complex ice table. It is clear that understanding the

MARS

dynamics and stability of the terrestrial ground ice would help understand the evolution of the Martian counterpart, and hence the evolution of the Martian climate.

IV. DIELECTRIC PROPERTIES OF ICE MATERIALS

4.1 Introduction

The transparency of ice and snow to high frequency radio waves (MHz range) was observed in Antarctica as early as 1933, even though the proof of such physical phenomenon was given in the 1950's when US air force pilots, landing on the Greenland ice sheets, were systematically reporting errors in aircraft altitude estimated by radar altimetry. This accidental observation brought Waite and Schmidt (1961) to demonstrate that a radar altimeter (the SCR 718 operating at 440 MHz) could measure the thickness of the polar glaciers, starting the era of radio-echo sounding (RES) systems (*Annan, 2002*). Few years before, (El-Said, et al., 1956) has attempted to detect the water table depth in soil desert using the interference between direct air transmitted signals and signals reflected from the top of the water table, showing that radio waves can also penetrate dry natural materials.

Nowadays I am well aware that, on Earth, ice (snow) and dry sand are more the exception than the rule in terms of radio wave absorption, because crustal rocks and soils are partially or totally saturated in water, which is usually a radio wave absorber, especially when it is rich in electrolytes. Deep penetration of high frequency radio waves, i.e. of the order of few km, have been extensively reported only in Arctic (*Oswald, et al., 2008*) and Antarctic regions. On the other hand, on rocky planets and Solar System icy bodies, the use of radio waves as sounding tool is

largely favourite by the extremely dry and cold conditions of their subsurface.

In order to understand the physical reason for the remarkable difference in electromagnetic behaviour between ice and all other geomaterials, the basic concept of electromagnetic properties should be reviewed. RIME, as any other Ground Penetrating Radar (GPR), uses radio waves to create an electromagnetic image of the structures buried in the ground; such an image is the result of the interaction between the waves and the different materials present at depth. In practice, the physical-chemical diversity of rocks, soils and ice translates into a different electromagnetic behaviour, which is controlled by the constitutive parameters of the materials, i.e. the complex dielectric permittivity and the complex magnetic permeability. For non-magnetic materials, as those expected in the crust of the Jovian icy satellites, the dominant parameter is the dielectric permittivity, which describes both polarization and conduction phenomena. The polarization arises when an external electric field is applied to a material producing a local redistribution of bound charges to new equilibrium positions. Such a rearrangement generates a storage of energy and, at macroscopic level, modifies the resultant electric field. The second effect is the electric conduction which, however, manifests itself only when free charge carriers are present. To quantify and describe those phenomena it's necessary to make some theoretical recalls.

4.2 Theoretical recalls

Every substance has characteristic electro-magnetic properties, like permittivity and electric conductivity as well as permeability.

The permittivity ε describes the propagation properties of electric fields in materials, while the conductivity σ gives information about a material's ability to conduct electric current, and the permeability μ is a degree of a material's magnetization, when an external electric or magnetic field is applied. The connection between electric and magnetic fields and charged sources as well as specific electric properties of the material are described by the Maxwell equations:

$$\vec{\nabla} \times \vec{H} = \frac{\partial \vec{D}}{\partial t} + \vec{J}$$

Equation II

$$\vec{\nabla} \times \vec{E} = -\frac{\partial \vec{B}}{\partial t}$$

Equation III

$$\vec{\nabla} \cdot \vec{B} = 0$$

Equation IV

$$\vec{\nabla} \cdot \vec{D} = \rho$$

Equation V

with $\vec{B} = \mu \vec{H}$, $\vec{D} = \varepsilon \vec{E}$ and $\vec{j} = \sigma \vec{E}$; \vec{B} is the magnetic induction, \vec{E} the magnetic field strength, the electric displacement, the electric field strength, the current density and ρ the charge density. The permittivity ε , the electric conductivity σ and the permeability μ are scalar if a medium is isotropic. They are constant if a medium is homogeneous. Otherwise they are tensors.

In the following, only the electric properties σ and ε will be discussed, since μ can be considered neglectable because the test materials are non magnetic. Now I can consider the total density current \vec{J}_T induced in a material when it is exposed to an external electric field:

$$J_T = J_c + J_d = \sigma_s E + \frac{\partial D}{\partial t}$$

Equation VI

Where J_c is the conduction current density, J_d the displacement current density, E the applied electric field, σ_s the static conductivity, $D = \epsilon_0 E + P = \epsilon_0 \epsilon_r E$ the dielectric displacement, P the polarization, $\epsilon_0 = 8.85 \times 10^{-12}$ F m⁻¹ and ϵ_r the relative permittivity, which is in general a complex quantity $\epsilon_r = \epsilon_r' - j\epsilon_r''$. If the applied electric field is monochromatic and a sinusoidal function of angular frequency ω , the total density current in the frequency domain can be written as follows:

$$\begin{aligned} J_T &= \sigma_s E + j\omega \epsilon_0 \epsilon_r E = \\ &= (\sigma_s + \omega \epsilon_0 \epsilon_r'') E + j\omega \epsilon_0 \epsilon_r' E = \\ &= \sigma_e E + j\omega \epsilon_0 \epsilon_r' E \end{aligned}$$

Equation VII

The quantity $\sigma_e = \sigma_s + \omega \epsilon_0 \epsilon_r'' = \sigma_s + \sigma_a$ is the effective conductivity (Balanis, 1989) and is given by two terms which describe the loss phenomena in the material. A first term σ_s accounting for the inelastic scattering of free charge carriers during their migration in the material, which is present at all frequencies (also at $\omega=0$); and a second term $\omega \epsilon_0 \epsilon_r''$ due to the friction in the polarization process, which linearly increases with ω and disappear at $\omega=0$. Moreover, the term $j\omega \epsilon_0 \epsilon_r'$ in Equation VII is the displacement current, directly linked to the polarization of the material.

Re-arranging Equation VII can define the effective complex dielectric permittivity:

$$\begin{aligned}
\varepsilon_e &= \varepsilon_e' - j\varepsilon_e'' = \\
&= \varepsilon_r' - j\left(\varepsilon_r'' + \frac{\sigma_s}{\omega\varepsilon_0}\right) = \\
&= \varepsilon_r' - j\frac{\sigma_e}{\omega\varepsilon_0}
\end{aligned}$$

Equation VIII

Whereas the ratio of the imaginary to the real parts gives the loss tangent:

$$\tan \delta = \frac{\varepsilon_r'' + \sigma_s / \omega\varepsilon_0}{\varepsilon_r'}$$

Equation IX

The polarization may be due to several distinct processes:

- i) the displacement of bound negative and positive charges in atoms and molecules (atomic or ionic polarization);
- ii) the orientation of existing dipoles toward the direction of the applied field (orientational polarization);
- iii) the separation of mobile charge carriers at interfaces of impurities or other defect boundaries (space charge polarization). In general, the time required for electronic and atomic polarization and depolarization is very short ($<10^{-12}$ s). This deformational polarization process is also referred to as the resonance process because it involves vibrating modes. Resonance of a vibrating system occurs when an excitation field oscillates at frequency close to the natural frequency of the system. The time required for orientational, hopping, or space charge polarization and depolarization is quite long and varies in a wide range, depending on the dielectric systems; such polarization processes are sometime referred to as relaxation processes because they involve a relaxation

time τ . A relaxation phenomenon occurs when a restoring action tends to bring the excited system back to its original equilibrium state.

Figure XXXI qualitatively describes the time response, in a generic dielectric, of the various polarization processes when a step function excitation field E is applied.

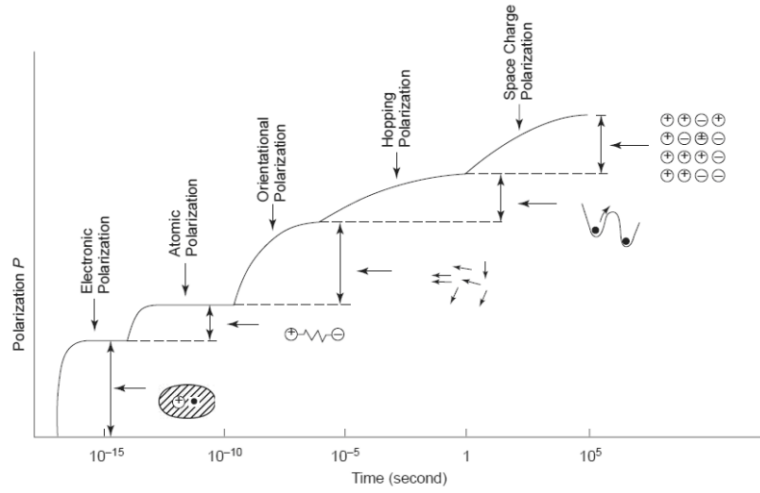


Figure XXXI The time response, in a generic dielectric, of the various polarization processes when a step function excitation field E is applied.

Because no geo-material is free of dielectric losses and therefore free of dispersion, it is however more interesting to look at the dielectric properties in the frequency domain. The most common mathematical model which better describes the spectral behaviour of a wide range of geo-materials is the Debye equation (Debye, et al., 1929):

$$\begin{aligned}\varepsilon_e(\omega) &= \varepsilon_\infty + \frac{(\varepsilon_s - \varepsilon_\infty)}{1 + j\omega/\omega_{rel}} - j\frac{\sigma_s}{\omega\varepsilon_0} \\ \varepsilon_e'(\omega) &= \varepsilon_\infty + \frac{(\varepsilon_s - \varepsilon_\infty)}{1 + (\omega/\omega_{rel})^2} \\ \varepsilon_e''(\omega) &= \frac{(\varepsilon_s - \varepsilon_\infty)\omega}{\omega_{rel} [1 + (\omega/\omega_{rel})^2]^2} + \frac{\sigma_s}{\omega\varepsilon_0}\end{aligned}$$

Equation X

Where $\omega_{rel} = 1/\tau$ is the relaxation angular frequency, and ε_s and ε_∞ are the static and the high frequency permittivities, respectively. *Equation X* refers to a material with only one relaxation frequency. With some algebraic manipulation, the effective conductivity in Equation VII can also be written as:

$$\sigma_e = \sigma_\infty - \sigma_s \frac{\omega^2}{\omega^2 + \omega_{rel}^2}$$

where the high frequency conductivity is:

$$\sigma_\infty = \sigma_s + \varepsilon_0 (\varepsilon_s - \varepsilon_\infty) \omega_{rel}$$

Equation XI

Figure XXXIII qualitatively shows the behaviour of the effective conductivity versus frequency, whereas. I can note that, at high frequency, i.e. for $\omega \gg \omega_{rel}$, the effective conductivity approaches σ_∞ , and the real and imaginary parts approach ε_∞ and $\sigma_\infty/\omega\varepsilon_0$, respectively.

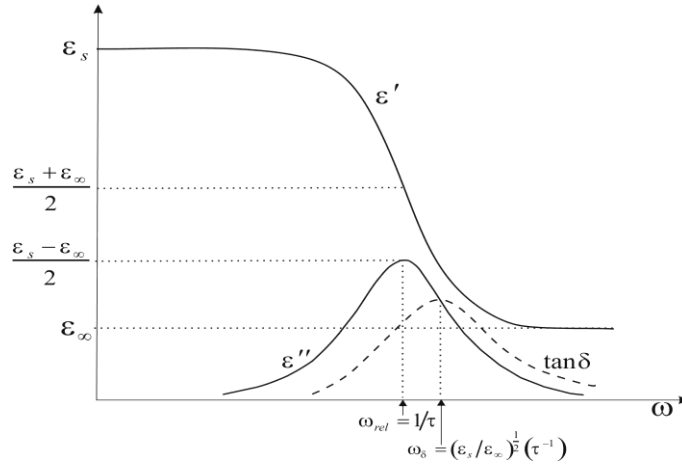


Figure XXXII Real and imaginary parts of the effective permittivity vs. frequency

The relaxation angular frequency depends on temperature according to:

$$\omega_{rel} = \omega_0 \exp\left(-E_{\omega_{rel}}/k_B T\right)$$

Equation XII

Where ω_0 is a constant, $E_{\omega_{rel}}$ is a quantity having the dimension of energy (often called the activation energy), k_B the Boltzmann constant and T is the temperature in Kelvin. Moreover, for dipolar materials [von Hippel, 1954] (Von Hippel, 1954) the difference between static and infinite permittivity depends on temperature, as follows:

$$\epsilon_s - \epsilon_\infty = \frac{A}{T}$$

Equation XIII

Where A is a constant and T is expressed in Kelvin.

Substituting and neglecting the static conductivity, the Debye relations can be re-written as:

$$\begin{aligned}\varepsilon_e'(\omega) &= \varepsilon_\infty + \frac{A/T}{1 + (\omega/\omega_0)^2 \exp(2E_{\omega_{rel}}/k_B T)} \\ \varepsilon_e''(\omega) &= \frac{(A/T)\omega \exp(E_{\omega_{rel}}/k_B T)}{\omega_0 \left[1 + (\omega/\omega_0)^2 \exp(2E_{\omega_{rel}}/k_B T) \right]}\end{aligned}$$

Equation XIV

Which shows that the real part of permittivity increases when the temperature decrease, whereas the peak of the imaginary part increases and moves leftwards (towards lower frequencies) (see *Figure XXXIII*) Finally, because the static conductivity depends on temperature according to Arrhenius equation, the behaviour of the effective conductivity vs. temperature is given by:

$$\sigma_e = \sigma_{s_0} \exp(-E_{\sigma_s}/k_B T) + \varepsilon_0 \frac{A}{T} \omega_0 \exp(-E_{\omega_{rel}}/k_B T) \frac{\omega^2 \exp(2E_{\omega_{rel}}/k_B T)}{\omega_0^2 + \omega^2 \exp(2E_{\omega_{rel}}/k_B T)}$$

Equation XV

Where σ_{s_0} is a constant and E_{σ_s} is the activation energy of free charge carriers.

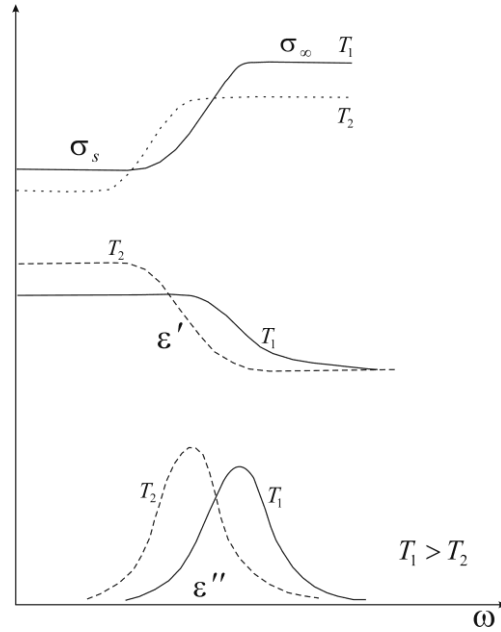


Figure XXXIII The behaviour of the effective conductivity, real and imaginary part of permittivity in function of temperature and frequency.

4.3 Wave propagation

The electromagnetic waves emitted by RIME antenna can be approximated to uniform plane waves, whose electric component can be expressed as:

$$E(t, z) = E_0 e^{j\omega t} e^{-\gamma z}$$

Equation XVI

Where $\gamma = j(\omega/c)\sqrt{\epsilon_e} = \alpha + j\beta$ is the propagation constant (for non-magnetic materials), E_0 is the amplitude, z is the direction of propagation, c is the speed of light in vacuum, and t is the time. The real part of the propagation constant is the attenuation factor:

$$\alpha = \frac{\omega}{c\sqrt{2}} \left[\sqrt{\varepsilon_e'^2 + \varepsilon_e''^2} - \varepsilon_e' \right]^{1/2} \approx \frac{\sigma_e}{2c\varepsilon_0\sqrt{\varepsilon_e'}}$$

Equation XVII

Where the approximation is valid for $\sigma_e \ll \varepsilon_e' \varepsilon_0 \omega$. Such quantity determines the maximum penetration depth of the radar waves. The parameter $\beta = \omega/v$ is the phase constant which accounts for the phase velocity:

$$v = \frac{c\sqrt{2}}{\left[\sqrt{\varepsilon_e'^2 + \varepsilon_e''^2} + \varepsilon_e' \right]^{1/2}} \approx \frac{c}{\sqrt{\varepsilon_e'}}$$

Equation XVIII

Such quantity allows to transform travel time in depth.

The electromagnetic image is the results of the reflections of the radar echoes from any dielectric contrast present in the subsurface. For “normally-incident” plane waves and perfectly flat interfaces, the amplitude of the reflected signal is proportional to Fresnel reflection coefficient:

$$R = \frac{\sqrt{\varepsilon_{e1}} - \sqrt{\varepsilon_{e2}}}{\sqrt{\varepsilon_{e1}} + \sqrt{\varepsilon_{e2}}}$$

Equation XIX

Where the subscripts refer to adjacent layers (or objects). In the case of low-loss materials, if the dielectric contrast is mainly due to the variation in real part of permittivity, i.e. $\varepsilon_{e1}' = \varepsilon_e'$ and $\varepsilon_{e2}' = \varepsilon_e' + \Delta\varepsilon_e'$, Equation XIX can be approximated according to (Paren, et al., 1975)

$$R \approx \frac{\Delta\varepsilon_e'}{4\varepsilon_e'}$$

Equation XX

On the other hand, if the variation is mainly due to conductivity, i.e. $\sigma_{e_1} = \sigma_e$ and $\sigma_{e_2} = \sigma_e + \Delta\sigma_e$, Equation XIX becomes (Paren, et al., 1975):

$$R \simeq \frac{\Delta\sigma_e}{4\omega\epsilon_0\epsilon'_e}$$

Equation XXI

High permittivity or conductivity contrasts generate large backscattered echoes, allowing a better identification of the interfaces and, therefore, increasing the quality of the electromagnetic image. Finally, note that because the effect of temperature is more pronounced on conductivity than on real part of permittivity, the R coefficient calculated according to Equation XXI is much more sensitive to temperature than that estimated using Equation XX.

4.4 Dielectric properties of pure water ice

The Debye relaxation model given in *Equation X* is well suited to describe the electrical behaviour of pure water ice. Such behaviour, essentially due to proton hopping polarization, has been extensively studied by several authors, with major contribute from (Bjerrum, 1952), (Gränicher, et al., 1957), (Jaccard, 1959), (Onsager, et al., 1960), (Jaccard, 1964.), (Nagle, 1974). In this section I recall the basic principles and main results of (Jaccard, 1959), (Jaccard, 1964) quantitative theory of the dielectric properties of pure water ice. This is based on the presence in the ice lattice of protonic defects (intrinsic defects), whose motion has the effect of reorienting the molecules along their path. Two different types of protonic point defects can occur inside the perfect structure of

the ice lattice: a first type associated to the rotation of H_2O molecules and a second one due to proton transfer between adjacent molecules. The rotation of the H_2O molecule inside the lattice produces a Bjerrum defect pair (L and D) generating a site with a lack of proton, known as Bjerrum L -defect, and a site with two facing protons, known as Bjerrum D -defect (see Figure XXXIV panel A). On the other hand, the motion of the proton along the bond transfers the ionization state between adjacent H_2O molecules, generating a pair of ionic defects, H_3O^+ and OH^- (see Figure XXXIV).

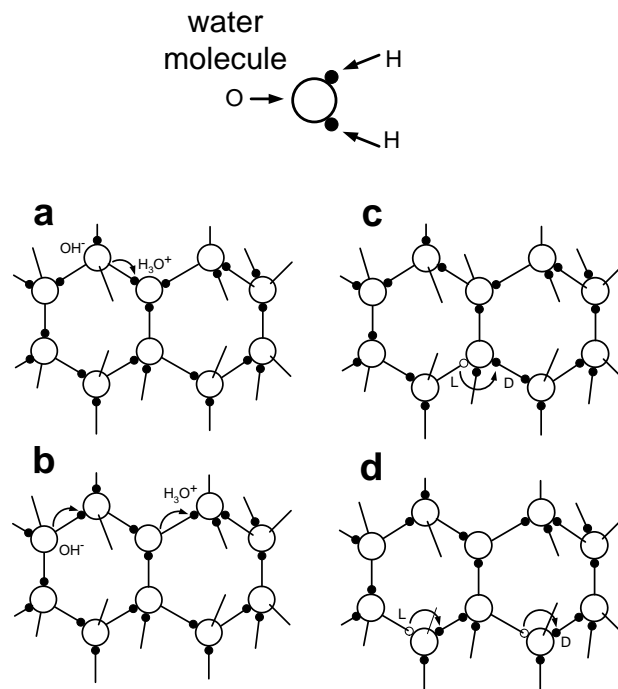


Figure XXXIV

The peculiar structure of pure water ice makes more difficult the understanding of its dielectric behaviour, since the dielectric permittivity and the electrical conductivity are strongly coupled, as pointed out by (Petrenko, et al., 1999). In most materials the process of dielectric polarization and electrical conductivity are totally distinct and

can be analysed independently. This is not the case for ice, where both are properties of the protonic subsystem and arise from motions of the two pairs of protonic point defects". As a consequence, the application of an electrical field produces a motion of the defects along the ice lattice giving rise to both polarization and conduction phenomena.

For each type of defect I can define the partial conductivities as follows:

$$\sigma_i = n_i \mu_i |e_i|$$

Equation XXII

where the subscript i indicates the type of defect, n_i represents the volumetric concentration, μ_i is the mobility and e_i is the effective charge. Some of these parameters have been experimentally estimated and are summarized in (Petrenko, 1993); (Petrenko, et al., 1999). To keep simple the mathematical approach, it is convenient to group the different contributions into a ionic conductivity $\sigma_{\pm} = \sigma_{H_3O^+} + \sigma_{OH^-}$ and a Bjerrum conductivity $\sigma_{DL} = \sigma_L + \sigma_D$. The way these terms combine into the equation of the pure water ice conductivity depends on frequency. At high frequency ($\omega \gg \omega_{rel}$) each defect moves independently from the others and the total conductivity is given by:

$$\sigma_{\infty} = \sigma_{\pm} + \sigma_{DL}$$

Equation XXIII

On the other hand, the static conductivity ($\omega = 0$) is given by:

$$\frac{e^2}{\sigma_s} = \frac{e_{\pm}^2}{\sigma_{\pm}} + \frac{e_{DL}^2}{\sigma_{DL}}$$

Equation XXIV

From Equation XXIV it follows that the static conductivity requires the presence of both types of defect. The effect of each type of defect on total conductivity is still an open issue, even though some authors (Wolff, et al., 1997); (Petrenko, et al., 1999), on the basis of both theoretical considerations and experimental data, pointed out that at normal temperature $\sigma_{DL} \gg \sigma_{\pm}$ which implies that $\sigma_{\infty} \approx \sigma_{DL}$ and $\sigma_s \approx \sigma_{\pm} (e^2/e_{\pm}^2)$.

Finally, the Jaccard theory allow us to define the Debye parameters as follows (Jaccard, 1964), (Petrenko, et al., 1999):

$$\omega_{rel} = \Phi \left(\frac{\sigma_{DL}}{e_{DL}^2} + \frac{\sigma_{\pm}}{e_{\pm}^2} \right)$$

Equation XXV

$$\varepsilon_s - \varepsilon_{\infty} = \frac{(\sigma_{\pm}/e_{\pm} - \sigma_{DL}/e_{DL})^2}{\varepsilon_0 \Phi (\sigma_{\pm}/e_{\pm}^2 + \sigma_{DL}/e_{DL}^2)^2}$$

Equation XXVI

where $\Phi = \frac{8}{3} r_{O-O} k_B T$ is the polarizability constant which depends on temperature and O-O distance r_{O-O} .

The explicit dependence from temperature of the Debye parameters can be obtained taking into account that:

i) the volumetric concentration of the intrinsic defects follows the Boltzmann equation $n_i = N_i \exp(-E_i / 2k_B T)$, where $N_i = \frac{2}{3} N$ for ionic

defects and $N_i = N$ for Bjerrum defects, and N is the number of H_2O molecules per unit volume, E_i are the energies of formation of defect pairs;

ii) the mobility μ_i follows the Arrhenius relation $\mu_i = M_i \frac{1}{T} \exp(-E_{im} / k_B T)$, where M_i is a constant and E_{im} is the activation energy for motion.

If only one type of defect dominates, as in the case of L defects at normal water ice temperature the high frequency conductivity assume a more simple form:

$$\sigma_\infty \propto \frac{1}{T} \exp\left(-\frac{E_{\sigma_\infty}}{k_B T}\right)$$

Equation XXVII

where $E_{\sigma_\infty} = 1/2 E_l + E_{im}$. Note that under these assumptions, the relation for ω_{rel} as a function of temperature assumes the form of *Equation XII* in which $E_{\omega_{rel}} = E_{\sigma_\infty}$.

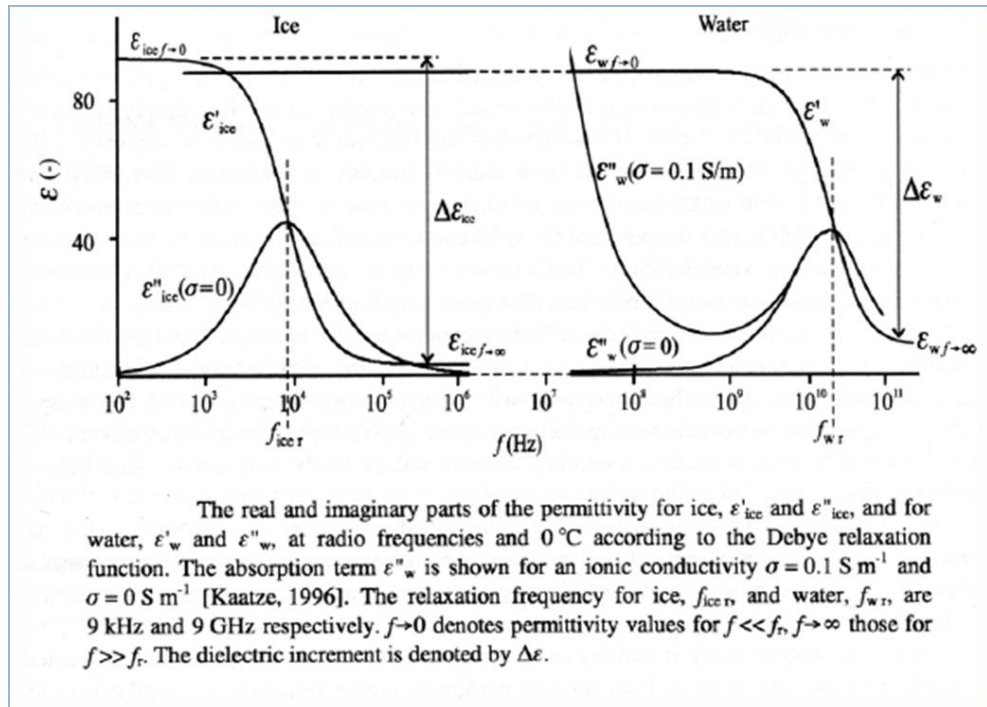


Figure XXXV The real and imaginary parts of the permittivity for ice, ϵ'_{ice} and ϵ''_{ice} and for water, ϵ'_{water} and ϵ''_{water}

Pure water ice electric properties have been experimentally studied in single crystal and polycrystalline samples by several authors (Auty, et al., 1952), (Camplin, et al., 1978), (Johari, et al., 1981); (Johari, 1976); (Johari, et al., 1975). As an example, Figure XXXV shows real and imaginary parts of pure water ice versus frequency. The analysis of the literature shows that electrical conduction through laboratory frozen single crystals is well described by the movements of protonic point defects, in agreement with Jaccard theory. In contrast, conduction through naturally formed polycrystalline ice is inevitably more complex due to variable crystal orientation fabric and to trace concentration of various impurities (Wolff, et al., 1997), (Kulesa, et al., 2007).

4.5 Effect of impurity in water ice

As well known, liquid water is the “universal solvent” because it is able to dissociate more substances than any other solvent. In its solid phase, however, the substances become often insoluble and in general are incorporated as inclusions or clusters. The solubility in ice is quantified by the partition coefficient, which is the ratio of the ions concentration in ice to that in the liquid in which the ice has been grown (Gross, et al., 1977).

The electrical properties of ice are very sensitive to small concentration of specific impurities if these are able to replace the existing oxygen and modify the lattice structure. Such impurities can be incorporated in the hydrogen bonded network and generate protonic point defects (Petrenko, et al., 1999), (Gross, et al., 1971), Gross et al., 1978, (Kawada, et al., 1997). Among those most common ions entering the ice lattice are H^+ , OH^- , NH_4^+ , Cl^- and F^- ; any compound (acid, base or salt) composed by one of these type of ions plays an important role in the ice electric properties (Wolff, et al., 1997), (Petrenko, et al., 1999). On the other hand, anions like NO_3^- and SO_4^{2-} or cations like Na^+ , Mg^{2+} and Ca^{2+} are too large to be incorporated inside the ice lattice and do not significantly affect the ice electric behaviour.

Our knowledge on the dielectric properties of ice with impurities is mainly based on the study of natural ices, being the data related to polar ice electrical measurements much larger than those collected on laboratory-grown ice. In terrestrial ice the four most common ionic impurities are (Wolff, 2000) (i) sea salt ions; (ii) sulphuric acid produced by volcanic eruptions; (iii) ammonium and organic anions; and (iv) terrestrial dust-derived ions. The literature describing the electrical behaviour of impurities in ice is very large (see, for example,

(Wolff, 2000), (Fujita, et al., 2000), (Grimm, et al., 2008), (Stillman, et al., 2010), but rather fragmented in terms of type of sample (natural or laboratory-grown), sample preparation, measurements techniques, range of frequency and temperature, type of impurity and concentration. In particular, the growth mechanism underlying the ice formation, which is very different in natural and artificial conditions, have a strong impact on the total number of ions incorporated in the ice lattice which is quantified by the partition coefficient. The differences in the sample origin and experimental procedures are probably the cause of apparent incoherent results sometime reported by various authors. In this scenario, it is particularly complicated to organize the results according to a key role parameter. Therefore I will present the most important experimental results in terms of different frequency ranges, with particular emphasis to high frequency conductivity σ_{∞} , which dominates the attenuation at RIME frequency (9MHz).

4.6 Static Conductivity

In previous Section I have shown, through *Equation XI* that σ_{∞} is theoretically affected by σ_s , therefore it is important to briefly review also the most significant experimental results relevant to static conductivity. As described in Section V, measurements performed on laboratory grown-ice provide the estimation of σ_s from equivalent circuit parameters, whereas the ECM technique does not allow to rigorously estimate such a parameter, making the comparison of the results very difficult. Several authors (Sugden, et al., 1995), (Gross, et al., 1978), (Jaccard, 1959) have pointed out that the concentration of acids and soluble salts in ice strongly affects the static conductivity. In particular, laboratory-grown doped ice seems to indicate a non-linear dependence of, static conductivity and impurity concentrations C , described by the equation $\sigma_s \propto C^m$, where the m exponent falls in the range 0.4-0.5 for the chemical impurities analyzed in the above mentioned papers. . On the other hand, ECM measurements on polar ice cores seem to indicate that such a technique is only sensitive to ice acidity, with a non linear correlation between the DC current and the H^+ concentration [Hammer. 1980]. The exact relation between σ_s and the DC current is not known, however it is often assumed that ECM essentially measure the static conductivity. In this framework, two mechanisms have been hypothesized to explain the role of acids on σ_s (Wolff, et al., 1997). The first is rooted in Jaccard theory for which acid cations (H^+) produce ionic defects (H_3O^+) in the ice lattice, increasing intracrystalline conduction. The second mechanism is due to electrolytic conduction of acidic liquids present in a network of veins connected at the ice triple junctions (Wolff, et al., 1984); (Kulesa, et al., 2007). The

latter mechanism is supported by observations of acid anions and associated elements at triple junctions and veins obtained by X-ray microanalysis, SEM images and Raman spectroscopy [e.g., *Mulvaney et al.*, 1988; *Wolff et al.*, 1988a; *Fukazawa et al.*, 1998; *Barnes and Wolff*, 2004]. The question of what would be the dominant mechanism controlling the static conductivity is still under debate; a comprehensive review on the issue can be found in (*Kulesa, et al.*, 2007) and literature therein.

4.7 High Frequencies Conductivity

Differently to what discussed above on σ_s , the high frequency conductivity is affected by the presence of different type of ions in the ice lattice, as demonstrated by measurements performed on laboratory-grown ice samples [e.g. (*Camplin, et al.*, 1978), (*Takei, et al.*, 1987), (*Petrenko, et al.*, 1999)] and on terrestrial ice cores with DEP technique [e.g. (*Moore, 1994*), (*Wolff, et al.*, 1997), (*Wolff, 2000*)]. In particular, the extensive literature on AC electrical measurements performed on ice cores, shows that high frequency conductivity is linearly dependent on the concentration of the ionic impurities, according to the following equation:

$$\sigma_{\infty} = \sigma_{\infty pure} + \sum_i \beta_i [C_i]$$

Equation XXVIII

Where $\sigma_{\infty pure}$ is the high frequency conductivity of pure ice, $[C_i]$ are the concentration of the specific ions, β_i are the coefficients weighting the contributions to conductivity of each single species. In the literature, the most common relationship used is:

$$\sigma_{\infty} = 9 + 4[H^+] + 1[NH_4^+] + 0.55[Cl^-]$$

Equation XXIX

with σ_{∞} expressed in $\mu S m^{-1}$ and the ion concentration in μM .

Equation XXIX has been estimated analysing the Greenland Ice Coring Project (GRIP) data (Wolff, et al., 1997); Stillman et al., 2013 at the reference temperature of $-15^{\circ}C$. Note that different coefficients have been derived in other sites sometime using a different reference temperature. Moreover, as highlighted by some authors (Wolff, 1994); (Wolff, 2000) in *Equation XXIX* the uncertainties on both acid and ammonium coefficients are as large as 20% whereas the others two coefficients seem to be affected by uncertainties of few percent. For example, (Barnes, et al., 2002) showed that the value of $\sigma_{\infty pure}$ (at $-15^{\circ}C$) could in some cases be higher ($10-12 \mu S m^{-1}$) than the accepted value $\sigma_{\infty pure} = 9 \mu S m^{-1}$ found by (Camplin, et al., 1978). Even though *Equation XXIX* has been extensively used to correlate the high frequency conductivity to the ionic concentration, (Wolff, 2000) has pointed out that, since the defects that each ion produces would be mutually destructive, such equation should be separated in two contributions (i.e. $\sigma_{\infty} = 9 + 4[H^+] + 1[NH_4^+]$ and $\sigma_{\infty} = 9 + 4[H^+] + 0.55[Cl^-]$) one related to the ammonium content and the other to the chloride content.

Equation XXIX can be explained through Jaccard theory (Equation XXII (Wolff, 1994), (Wolff, et al., 1997), (Wolff, 2000); Stillmann et al., 2013; the first term ($\sigma_{\infty, pure}$) is due to the intrinsic L-defects, the second term to the creation of ionic defects caused by the presence of acids (H_3O^+), the third and the fourth terms to the creation of extrinsic *L*- and *D*-defects. For example, if Cl^- enters the lattice as *HCl*, it forms one *L*-defect and one ionization defect (H_3O^+), whereas if Cl^- enters the lattice alone (e.g. as *NaCl*) it forms two *L*-defects (see Table II) (Wolff, et al., 1997).

It is important to recall that the ionic concentrations in Equation XXVII are measured in the solution obtained after melting the ice sample. Therefore, such a concentration, due to the different solubility of the chemical compounds in water and in ice, is not representative of the number of protonic defects which were originally present in the ice lattice. To quantify this number the partition coefficient for each single species should be known. Several attempts to estimate such coefficients have been carried out on ice core samples (Moore, 1999), (Moore, 1994), (Wolff, 2000), (Stillman, 2013b) and on laboratory-grown ices (Gross, et al., 1977), (Grimm, et al., 2008). The resulting values are in strong disagreement (ranging between $10^{-4} \div 1$) probably due to the experimental factors like the growing process or the origin of ice and the measurement technique used.

Ions Present	Extrinsic Defects created (per ion set)
NH_4^+, Cl^-	$2D, 2L$
H^+, Cl^-	$1 H_3O^+, 1L$
Cl^-	$2L$
NH_4^+	$2D$
H^+	$1 H_3O^+, 1D$

Table III Extrinsic defects due to different ions entering the ice lattice

So far, nothing has been said on the temperature dependence of the bulk conductivity of the doped ice. According to Jaccard theory, the coefficients β_i in *Equation XXVIII* follow the Arrhenius law (cf. *Equation XXVII*) where the activation energy, experimentally estimated for the intrinsic and extrinsic defects (see *Table III*) [(Jaccard, 1959), (Camplin, et al., 1978), (Takei, et al., 1987)] represents the key parameter to compute the conductivity related to each ionic type at a given temperature. Finally, the doped ice bulk conductivity can be computed applying the following equation:

$$\sigma = \sum_i \frac{C_i}{T} e^{-\frac{E_i}{k_B T}}$$

Equation XXX

4.8 Dielectric response up to 1 GHz (imaginary, real part vs impurity)

In a wider frequency range, the imaginary part of dielectric permittivity (up to GHz frequencies) has been considered the combination of the tail of the Debye relaxation behaviour (typical of the low frequencies) and the lattice vibration in the far-infrared region [(Fujita, et al., 2000), (Matzler, et al., 1987); (Matsuoka, 1996)]. On the other hand, the real part can approximately be considered constant vs temperature and frequency.

As the amount of data are essentially present below 1MHz and in the GHz region with and few data in the megahertz region [(Johari, et al., 1975), (Johari, 1976)], the MHz response of ice has been determined by an interpolation of LF data [(Johari, et al., 1975); (Johari, 1976)] and microwave data [(Matzler, et al., 1987), (Matsuoka, 1996)].

That is, the imaginary part is expressed as:

$$\varepsilon'' = \frac{A}{f} + Bf^c$$

Equation XXXI

where the first term, is the tail of Debye relation behaviour and the second describes the effect of absorption due to lattice vibration. (Matsuoka, 1996) report the values of parameter A, B and C as a function of temperature .

4.9 Conductivity

The influence of impurity on the imaginary part of permittivity (or equivalently on conductivity) has been investigated in several articles [(Fujita, et al., 2000), (Matsuoka, 1996)]. The response of the conductivity performed on laboratory doped ice in the microwave range (Moore and Fujita, 1993) are similar to the that of ice core at low frequency and at single temperature (see above). In particular, measurements conducted on acid doped ice containing either HNO_3 , H_2SO_4 or HCl from $-2.5^\circ C$ to $-30^\circ C$ with concentrations between 2 mM and 35 mM show a linear relation between conductivity measured at 9.2 GHz and molarity (M) [Fujita et al., 1992]:

$$\sigma_{GHz} = \sigma_{\text{pure ice}} + \mu_a[\text{acid}]$$

Equation XXXII

where μ_a is a coefficient [$S\ m^{-1}\ M^{-1}$] that depends on temperature (see (Fujita, et al., 2000)). A linear relation between salts and conductivity has also been obtained by (Matzler, et al., 1987) using their measurements conducted on ice containing a high concentration of salt (higher than meteoric ice, 193 μM of sea salt chloride) and pure ice plus the data of Vant et al. [1974] on up to about 75 μM of $NaCl$.

$$\sigma_{GHz} = \sigma_{\text{pure ice}} + \mu[Cl]$$

Equation XXXIII

where μ_{cl} is a coefficient [$S\ m^{-1}\ M^{-1}$] that depends on temperature (see (Fujita, et al., 2000)). I have to note that this relation does not fit the higher salinity samples from (Vant, et al., 1974).

4.10 Real part

The measurements conducted by (Fujita, et al., 2000) and (Matsuoka, 1996), showed that between 100 MHz and 600 MHz and at 9.2 GHz on ice containing either H_2SO_4 , HNO_3 or HCl up to 5×10^{-3} M, the real part of permittivity is linearly dependent on acid concentration above the eutectic temperature of each impurity. In particular, this dependence is influenced also by the frequency and temperature:

$$\frac{d\varepsilon'}{dC} = 10^A f^B$$

Equation XXXIV

where the coefficients A and B are reported in the article of (Fujita, et al., 2000).

Below eutectic point for each sample, this linear relation disappears, probably because liquid phase is frozen below the eutectic points [Matsuoka et al., 1997]. On the other hand above the eutectic temperature, the equation XXX suggests that there is a polarization phenomena that takes place in the sample different from the reorientation of water molecules in the ice lattice (Fujita, et al., 2000) they interpreted this phenomenon with two explanations:

- 1) reorientation of water molecules in the liquid phase (the relaxation frequency is approximately 17 GHz);
- 2) or a kind of space charge polarization

(Maxwell-Wagner effect (*Von Hippel*, 1954)).

4.11 Anisotropy

Another property of the ice is its hexagonal structure which exhibits an uniaxial symmetry [*Kawada*, 1978 (*Fujita*, et al., 2000)]. The complex dielectric permittivity is expressed as a tensor, as follows:

$$\varepsilon = \begin{bmatrix} \varepsilon_{\perp c} & 0 & 0 \\ 0 & \varepsilon_{\perp c} & 0 \\ 0 & 0 & \varepsilon_{\parallel c} \end{bmatrix}$$

Equation XXXV

Here $\varepsilon_{\perp c}$ is the component when electrical field vector is perpendicular to the c-axis; $\varepsilon_{\parallel c}$ is the component when the electrical field is parallel to the c-axis. Therefore, when polycrystalline ice is isotropic (the c-axes have a randomly distributed orientation) and wavelength is sufficiently larger than the size of crystal grains (as is the case in the megahertz range), the macroscopic permittivity is

$$\varepsilon = \frac{2}{3}\varepsilon_{\perp c} + \frac{1}{3}\varepsilon_{\parallel c}$$

Equation XXXVI

The anisotropy of the static permittivity ε_s has been measured by several authors [*Humbel*, *Jona*, *Sherrer*, *Kawada*, 1978]. They reported a 15 % of variation between $\varepsilon_{\parallel c}$ and $\varepsilon_{\perp c}$ with a value of about 100 for $\varepsilon_{\parallel c}$. On the other hand, the anisotropy of the high frequency permittivity ε_{∞} is the order of 1% (*Matsuoka*, 1996) at 1MHz and 39GHz):

$$\varepsilon_{\parallel c} - \varepsilon_{\perp c} = 0.0256 \pm 0.001 + 3.6 \times 10^{-5} T$$

Equation XXXVII

considering the permittivity presents a weak dispersion with temperature in the range 1-100 MHz (*Fujita et al.*, 1993):

$$\varepsilon_{\parallel c} = (3.189 \pm 0.006) + 9 \times 10^{-4} T$$

Equation XXXVIII

(*Matsuoka et al.* 1997), using a single crystal sample, found that the imaginary part also showed clear anisotropy up to 1MHz. In particular, the imaginary part of $\varepsilon_{\parallel c}$ is larger than that of $\varepsilon_{\perp c}$ by about 20%. This anisotropy was observed only in the high frequency tail of the Debye dispersions and it was not observed at microwave frequencies.

This is agreement with the measurements performed by *Kawada* that showed that the relaxation frequency of parallel is greater the perpendicular in all examined temperature range. this small anisotropy in the relaxation frequency is not surprising because the dipole orientation is closely connected with the orientation of the water molecules.

4.12 Rock Impurities

Recently, some authors focused on the analysis of the influence of rock impurities on electrical properties of ice. In particular, (*Stillman, et al.*, 2010) measured the electrical properties of ice silicate/salt mixtures with different water saturation degree down to about 180K. They found at 181K five dielectric relaxation frequencies: the first (~ 630 kHz) is due

to the rotation of adsorbed water, the second ($\sim 200\text{Hz}$) to the rotation of L-defects, the third ($\sim 10\text{Hz}$) is due to Maxwell-Wagner interfacial polarization within adsorbed water, the fourth ($\sim 10\text{mHz}$) is due to Maxwell-Wagner polarization between salt hydrates and silicate and the fifth is the low frequency dispersion which is observed in all the samples at low water content.

(Mattei, et al., 2013) determined the effect of basalt sand in ice measuring the complex permittivity, in a wide range of temperature (150-250K) and frequency (20Hz-1MHz) in ice/basalt mixtures. The results showed that, besides the expected dependence of the attenuation from temperature, the presence of the solid inclusions in the ice strongly affects the behaviour of the attenuation versus frequency (Chyba, et al., 1998).

(Herique, et al., 2002) reported the results of dielectric permittivity measurements performed on granular samples of dunite, montmorillonite and kaolinite in order to correctly estimate the radio wave velocity for CONSERT data inversion. The authors measured the real and imaginary parts of permittivity on dry and iced samples as a function of temperature up to 12 kHz extrapolating the values at higher frequencies through Kramer-Kronig relationship. They found that there are two different components: the first, related to the grain matrix, which depends on the density of the mineral powder and to a lesser extent to the mineral nature; the second, related to the presence of ice, which exhibits a more dispersive behaviour.

(Heggy, et al., 2012) measured synthesized cometary analogs (ice/dust mixtures) with porosities of 20 to 50% (both dry and with porosities saturated by water ice), over the frequency range 1MHz-1GHz between 113-298K. Their results suggest that the real part of the dielectric constant increases with increasing temperature. Moreover the density-dependent measurements suggests that the real part and the loss

tangent of the relative dielectric permittivity increase for a 50:50 dust-to-ice mass ratio. The measurements suggest an exponential decrease in the dielectric constant (both real and imaginary parts) as a function of the decreasing bulk density:

$$\begin{aligned}\varepsilon' &= 2.2^{\rho_{bulk}} \\ \varepsilon'' &= 2.3 \times 10^{-3} \exp(1.17 \rho_{bulk})\end{aligned}$$

Equation XXXIX

4.13 Density

The effect of density on electrical properties of ice has been extensively discussed by several authors (*Robin et al.*, 1968); (*Greenberg, et al.*, 2002), (*Kovacs et al.*, 1995). In particular, (*Robin et al.* 1969) proposed an empirical equation for real part of permittivity obtained from field measurements in Greenland:

$$\varepsilon' = (1 + 0.851\rho)^2$$

Equation XL

where ρ is the density expressed in g cm^{-3} . More recently, the analysis on Antarctica data performed by *Kovacs et al.* [1995] showed that this expression could be slightly modified, as follows

$$\varepsilon' = (1 + 0.845\rho)^2$$

Equation XLI

Also the imaginary part of permittivity increases with increasing density as shown by (*Tiuri et al.* 1984) for dry snow, by (Glenn J.W., 1975) and (*Reynolds* 1985) for firn and by (Barnes, et al., 2002) for doped ices. In particular, (Barnes, et al., 2002) found that a polynomial relationship exists between HF conductivity and ice density taking into account the influence of the latter quantity on the conductivity with varying chemical composition (i.e. the coefficients in *Equation XIV* depends on density).

V. EXPERIMENTAL SET-UP

5.1 Laboratory measurements: the existing facility

The facility operating at the Mathematics and Physics Department of the University of Roma Tre is designed to measure the complex permittivity of a number of materials known or expected to exist on the surface of several Solar System bodies. The samples may consist of water ice/salt solutions or water ice/mineral grain mixtures prepared at the same volume fractions expected on the body surfaces. The measurements are performed in the frequency range from 20 Hz to 30 MHz (LCR meter – Agilent 4285A), thus covering a spectrum that widely includes the frequencies of radars currently operating as well as radars foreseen for future space missions. The samples can be tested in the temperature range 100–300 K, which encompasses the temperatures expected on the surface of several icy bodies in the Solar System.

The experimental setup is based on the use of a capacitive cell, filled with the materials to be tested, cooled at the desired temperature by a liquid nitrogen cryostat. The measurements provide the real part of permittivity and the loss tangent of the samples. These quantities allow us to estimate:

- 1- the propagation velocity of radar signals, which is a key parameter for determining the actual depth of the possible reflectors buried below the surface;
- 2- the attenuation of the radar signals along the propagating path. This is a fundamental parameter for evaluating the permittivity of possible subsurface structures detected at depth, which, in turn, helps in formulating hypotheses on the nature of the buried material.

5.2 Liquid nitrogen cryostat

The cryostat used to perform the measurements of the ice electrical properties versus temperature is schematically shown in Figure XXXIII.

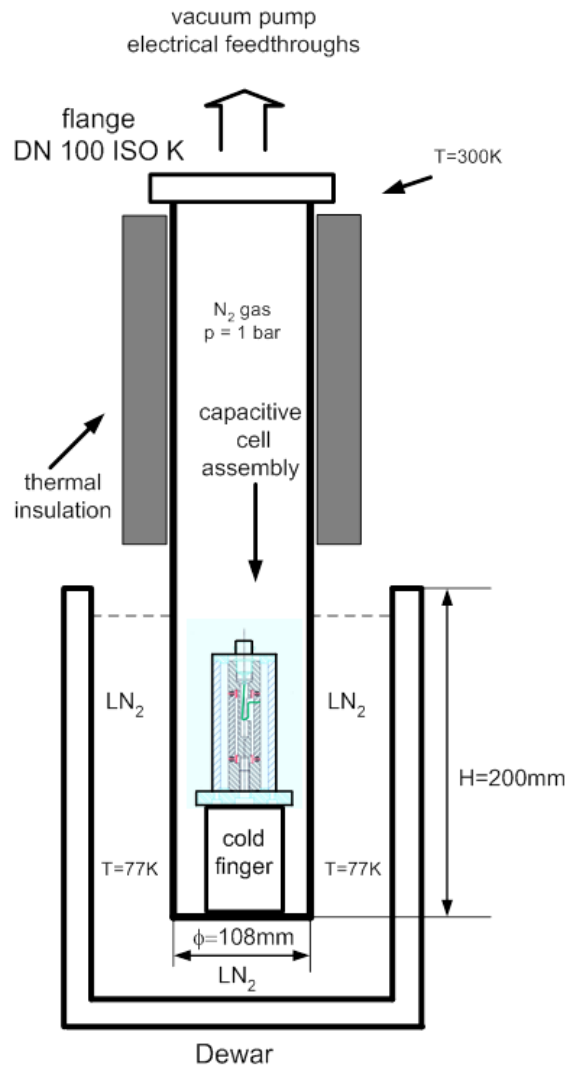


Figure XXXVI Scheme of Cryostat

It consists essentially in a hollow stainless cylinder, approximately 40cm high and 10cm wide, with its bottom part sunk (for a length of about 20cm) in a Dewar filled with liquid nitrogen (LN₂).

The higher part of the cylinder plays the role of thermal insulator which separates the part in contact with the LN₂ bath (at T=77K) from the upper flange which is at the room temperature (the stainless steel is a poor thermal conductor). The thermal losses are also reduced by a thick thermal insulation cover, which is applied on the lateral wall of the cryostat and extends up to the upper flange.

The pressure within the cryostat can be controlled by either evacuating the system, to obtain the degassing of the sample under test, or introducing some nitrogen gas, to enhance the thermal exchange with the capacitive cell and eventually speed up the cooling process.

The capacitive cell assembly is installed within the cylinder and fastened, through a thermal shunt, at its bottom.

The fixture needed to connect the capacitive cell to the LCR meter are made with four RG213 coaxial transmission lines (Teflon dielectric) equipped with four coaxial feedthroughs at the vacuum/air flange transition.

The fixture has been tested to verify its stable electrical properties from room temperature down to 100K by measuring the capacitance of the empty cell during a cooling cycle.

Indeed, in such a case, the measured capacitance is only determined by the geometrical dimensions of the cell (which are very stable) and any observed variation should be attributed to the fixture.

The measurements have confirmed the stability of the electrical properties of the device in the entire range of temperature (300-100K) as can be seen from the plot of capacitance and loss tangent shown in Figure XXXIX and XL. The cryostat has been designed to cool the capacitive cell down to about 100K with a cycle lasting about 3 hours and 6 liters consumption of LN₂.

EXPERIMENTAL SET-UP

For assuring the thermal equilibrium conditions of the ice sample during the measurements, the data acquisition has been performed during the warming part of the cycle, which lasts about 16 hours (from 100K to 300K). The capacitive cell is shown in Figure XXXIV and consists of a cylindrical capacitor with an external electrode 80mm height and 40mm wide. The inner electrode has a diameter of 20mm and is segmented in

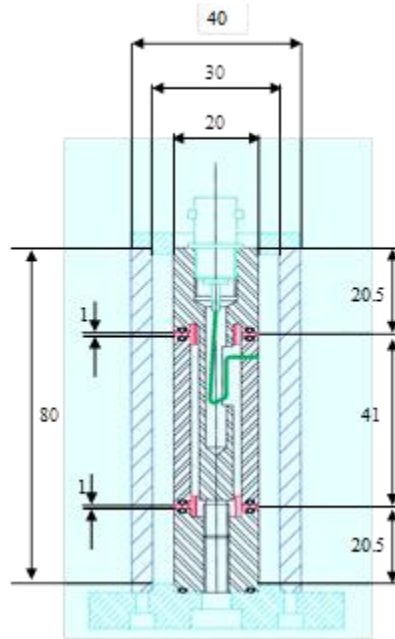


Figure XXXVII Scheme of capacitive cell

three parts: a central electrode 40mm height and two lateral guards each 20mm height.

The DUT has been modified to perform the necessary calibrations of the bridge. The following images show the cell used:



Figure XXXVIII The capacitive cell

EXPERIMENTAL SET-UP

The BNC connector, indicated with L in Figure XXXV, connects the measuring electrode to terminals L_{CUR} and L_{POT} of LCR meter (internal contact of the BNC is connected to the electrode, while the screen is connected to the two guards better described below).

In the outer electrode is present a second BNC connector (indicated with H in Figure XXXV) that is connected to H_{CUR} terminals and H_{POT} of LCR meter). Connecting the BNC cables together, the short-circuit correction can be performed, while the open-circuit calibration can be done simply disconnecting the BNC connector L from the cell.

The equivalent circuit of the capacitive cell (see Figure XXXVI) can be represented by a capacitor in parallel to a resistor, which accounts for the electric losses of the material.

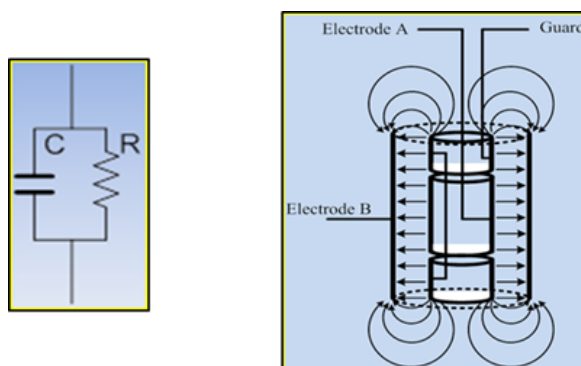


Figure XXXIX Left: *Equivalent electric circuit of a LCR meter*; Right: *Scheme of capacitive cell*.

The guard electrodes are needed to suppress the dispersion of electric field flux in correspondence of the central electrode, thus assuring stable capacitance measurements.

The cell is opportunely equipped with O-ring to allow measurements with liquids.

5.3 LCR meters: Agilent HP4284A/HP4285A

The instrument used is the LCR meter. It's able to measure *resistance*, *capacitance* and *inductance* of a DUT (Device Under Test). Using appropriate DUT, it's possible to study electrical characteristics of the material such as the electrical complex permittivity. In particular, I used two versions of the LCR meter, which operate in two different frequency bands:

<i>Agilent HP4284A</i>	<i>Agilent HP4285A</i>
From 20Hz to 1MHz	From 75KHz to 30MHz

Both tools are based on the same principle of operation, which can be summarized in the following equivalent circuit:

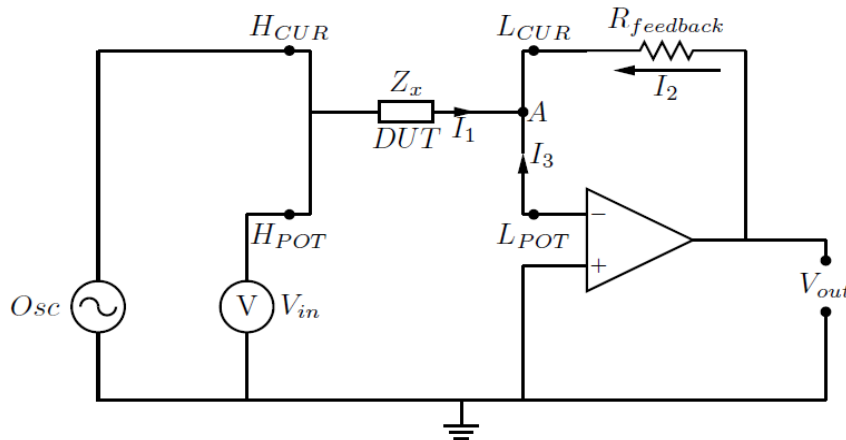


Figure XL Equivalent electric circuit of a LCR meter

The circuit can be modeled as an operational amplifier in inverting configuration, whose feedback resistor $R_{feedback}$ allows vary the

measuring range of the current through the DUT, excited by a sinusoidal voltage sent like input by the oscillator (Osc).

The tool performs a measurement (amplitude and phase) of the output voltage V_{out} , and the selectable input voltage V_{in} generated by the oscillator is appropriately measured in amplitude and phase, by the voltmeter.

The DUT examined is the unknown impedance Z_x , constituted by a capacitive cell (for measurement of electric permittivity). The value of Z_x can be obtained through the study of the currents in the A node:

$$I_1 + I_2 + I_3 = 0$$

Equation XLII

The current I_1 is given by the ratio between the input voltage V_{in} (v), set to a known frequency ν , and the value of the unknown impedance Z_x .

$$I_1 = \frac{V_{in}(\nu)}{Z_x(\nu)}$$

Equation XLIII

The current I_2 , in turn, is given by the ratio between the output voltage V_{out} and the feedback resistor $R_{feedback}$.

$$I_2 = \frac{V_{out}}{R_{feedback}}$$

Equation XLIV

The current I_3 instead, for the principle of virtual mass and assuming infinite input impedance of the operational amplifier, is equal to about zero:

$$I_3 = 0$$

Equation XLV

The sum of the currents of the node allows to express the impedance Z_x as:

$$\frac{V_{in}(V)}{Z_x} + \frac{V_{out}}{R_{feedback}} = 0 \rightarrow Z_x = -\frac{R_{feedback} \cdot V_{in}(V)}{R_{feedback}}$$

Equation XLVI

Through subsequent vector measurements of the input voltage and the voltage in output as a function of frequency, it is possible to know the value of unknown impedance Z_x in magnitude and phase. As you can see from Figure XXXV the connection of the DUT to the instrument is carried out with four wires (coaxial cables) connected to the four instrument's BNC denominated H_{CUR} , H_{POT} , L_{CUR} and L_{POT} .

5.4 Zeroing Calibration

Open and short circuit calibration (zeroing) should be performed on a daily basis to correct for cable and fixture errors before taking measurements. When test fixtures or test cables are changed, the zeroing process should be performed again. All data performed during the calibration is stored in the internal memory of the LCR.

The Open circuit calibration determines the stray admittance and compensates high impedance measurements. The short calibration determines the residual impedance and is used when determining low impedance measurements.

On both instruments HP4284A and HP4285A you have to perform two different corrections: OPEN and SHORT. Any error of calibration, or a

calibration not done properly could lead to errors in the measurements, especially at high frequencies.

5.5 Measurement of the electric permittivity

The LCR meter allows measurements to be made with reference to various circuits equivalent of the DUT, returning several parameters. For example, a capacitor can be characterized with parallel capacitance (C_p) and parallel resistance (R_p), or in series capacity (C_s) and series resistance (R_s), and still capacity parallel C_p and loss tangent ($\tan \delta$) and others...

To calculate the electric permittivity I use the equivalent circuit formed by the parallel capacitance C_p and the loss tangent $\tan \delta$ through these two values, I can retrieve information on the real and imaginary parts of the permittivity. The general relationship between current and voltage in the case of a capacitive cell, with its three impedances is:

$$I_{tot} = V \left(i \omega C + \omega C_0 \varepsilon_r'' + \frac{1}{R_\sigma} \right)$$

Equation XLVII

In this case it can become the following:

$$I_{tot} = V \left(i \omega \varepsilon_r' C_0 + \omega C_0 \varepsilon_r'' + \frac{\sigma}{\varepsilon_0} \right)$$

Equation XLVIII

with $\varepsilon_{tot}'' = \varepsilon_r'' + \frac{\sigma}{\varepsilon_0 \omega}$ I can simplify the formula by dividing the components in a capacitive reactance and resistance:

$$I_{tot} = V(i\omega\varepsilon'_r C_0 + \omega C_0 \varepsilon''_{rtot})$$

Equation XLIX

The following Figure XXXVIII shows the equivalent circuit of the above formula and the resulting phasor, in addition the δ tangent's angle is also indicated and its value will provide by the instrument:

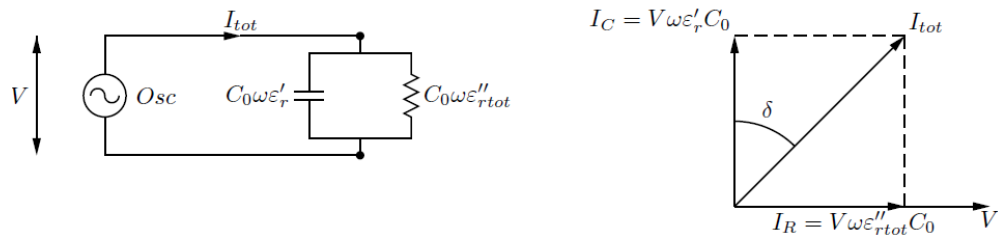


Figure XLI Vectorial currents diagram in a capacitive cell

ε'_r can be derived from the capacitance value provided by the instrument:

$$C = \varepsilon'_r C_0 \rightarrow \varepsilon'_r = \frac{C_p(V)}{C_0}$$

Equation L

Operatively, the real part of permittivity ε' can be derived directly from the ratio of capacitance C to the correspondent air capacitance C_0 , (being C_0 the capacitance of the cell measured removing the material from the gap).

Therefore is necessary to measure before the capacity of the DUT empty and then perform a measurement after that this was filled with the test

material. The uncertainty of the real part of the permittivity is calculated by the previous equation through the error propagation law given by:

$$\Delta\varepsilon'_r = \pm \frac{1}{\sqrt{3}} \left(\frac{\Delta C}{C_0} + \frac{C\Delta C_0}{C_0^2} \right)$$

Equation LI

where ΔC and ΔC_0 are obtained using a specific procedure.

As you can see from the diagram of Figure XXXVIII, $\tan \delta$ is the ratio between I_R and I_C , and this can be derived ε''_{rtot} :

$$\tan \delta = D = \frac{\omega C_0 \varepsilon''_{rtot}}{\omega C_0 \varepsilon'_r} = \frac{\varepsilon''_{rtot}}{\varepsilon'_r} \rightarrow \varepsilon''_{rtot} = D \cdot \varepsilon'_r$$

Equation LII

and

$$\Delta\varepsilon''_{rtot} = \pm \frac{1}{\sqrt{3}} (\varepsilon'_r \cdot \Delta D + D \cdot \Delta\varepsilon'_r)$$

Equation LIII

while $\Delta\varepsilon'_r$ is given by Equation LI the uncertainty ΔD is also shown in Appendix A and in Appendix B.

5.5.1 Theory of capacitive cell dielectric spectroscopy

As I mentioned earlier the dielectric spectroscopy has been performed by using two autobalance bridges coupled with a capacitive cell of large dimensions (volume of 400 cm³) covering the range 20 Hz – 30 MHz.

As it has been shown in Sect. 5.1, the complex permittivity at low frequencies consists of a real part ε' , corresponding to the actual dielectric constant, and an imaginary part $\varepsilon'' = \frac{\sigma_t}{\omega\varepsilon_0}$, which is a function of the ohmic conductivity of material, dipole dissipation and the testing frequency.

The complex permittivity of a given material, at low frequencies, is usually obtained by measuring the impedance of a capacitive cell filled with the test material given by this equation:

$$Z_{cell} = \frac{V_{gen}}{V / R_{fb}}$$

Figure XLII

Operatively, the real part of permittivity ε' can be derived directly from the ratio of capacitance C to the correspondent air capacitance C₀, (being C₀ the capacitance of the cell measured removing the material from the gap).

$$\varepsilon' = \frac{C_p(\nu)}{C_0}$$

Equation LIV

The imaginary part ε'' is obtained from the measurement of the dissipation factor ($\tan \delta$) through:

$$\tan \delta(\nu) = \frac{\varepsilon''(\nu)}{\varepsilon'(\nu)}$$

Equation LV

being the $\tan \delta$ related to the electrical circuit parameters through

$$\tan \delta(\nu) = \frac{1}{\omega C_p(\nu) R_p(\nu)}$$

Equation LVI

The measured quantities are the capacitance C and the loss tangent δ , which, in turn, provide the real and imaginary parts of the dielectric permittivity through the previous formulas :

$$\varepsilon' = \frac{C_p}{C_0}$$

$$\varepsilon'' = \varepsilon' \cdot \tan \delta$$

C_0 , the capacitance of the cell measured removing the material from the gap, can be measured through:

$$C = 2\pi\varepsilon_r\varepsilon_0 \frac{h}{\ln\left(\frac{D_2}{D_1}\right)}$$

Equation LVII

where D_2 is the diameter of the outer electrode, D_1 is the diameter of the inner electrode and h is the cylinder's height as indicated in the Figure XXXIII.

<i>Inner electrode's diameter</i>	$D_1 = 20.00 \pm 0.05 \text{ mm}$
<i>Outer electrode's diameter</i>	$D_2 = 30.00 \pm 0.05 \text{ mm}$
<i>cylinder's height</i>	$h = 40.05 \pm 0.05 \text{ mm}$

So the capacitance of the empty cell (capacitance between the central and external electrodes) is equal to :

$$C = 2\pi\varepsilon_r\varepsilon_0 \frac{h}{\ln\left(\frac{D_2}{D_1}\right)} = 5.56 \pm 0.04 \text{ pF}$$

EXPERIMENTAL SET-UP

And its uncertainty is given by:

$$\Delta C_0 = 2 \sqrt{\left[\frac{\varepsilon_0 \pi}{\ln\left(\frac{D_2}{D_1}\right)} \Delta h \right]^2 + \left[\frac{\varepsilon_0 h \pi}{D_2 \ln^2\left(\frac{D_2}{D_1}\right)} \Delta D_2 \right]^2 + \left[\frac{\varepsilon_0 h \pi}{D_1 \ln^2\left(\frac{D_2}{D_1}\right)} \Delta D_1 \right]^2}$$

Equation LVIII

Air capacitance C_0 measurements were made by both the HP4284A, and the HP4285A. The following graphs I can observe data acquired by the two instruments:

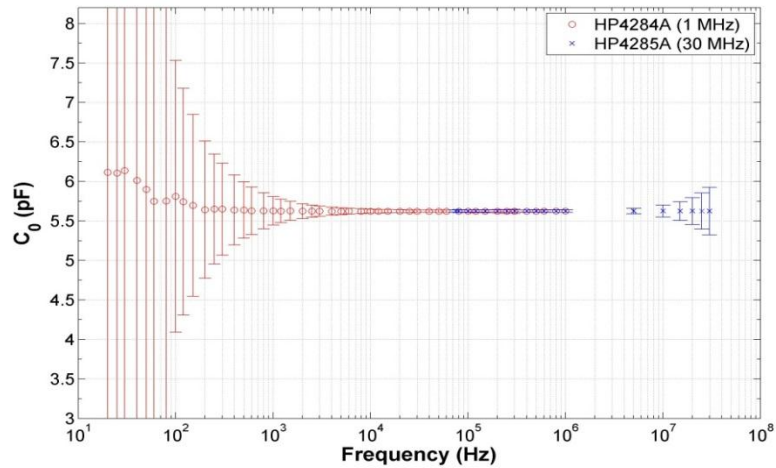


Figure XLIII Air Capacitance C_0

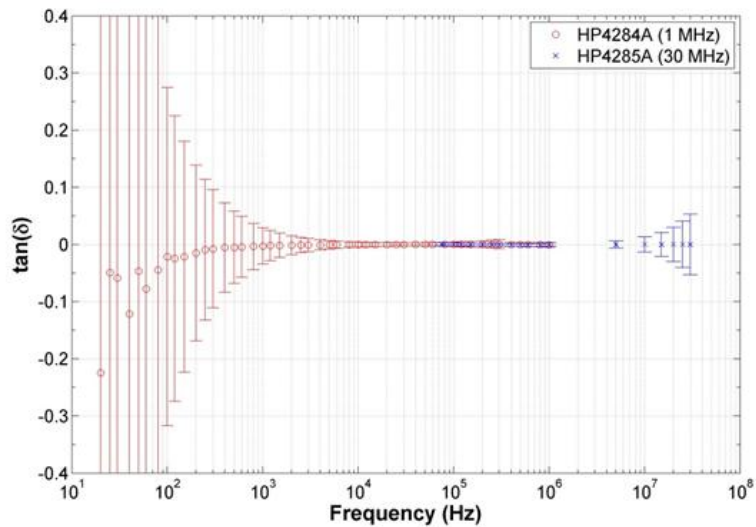


Figure XLIV Loss Tangent

EXPERIMENTAL SET-UP

As can be noted the value of the capacitance of the empty cell is constant in the frequency range from 100Hz to 5MHz. Some noises in the measurements occur at frequencies close to the harmonics (50Hz) but it does not invalidate the results at HF frequencies.

Through a fit of data in the plateau zone, it's possible to calculate the average value of $C_0 = 5.64 \pm 0.07 \text{ pF}$, a value in good agreement with the capacitance calculated geometrically.

In the following table there is shown the two values of capacitance C_0 .

<i>Geometrical Capacitance</i>	$C_0 = 5.56 \pm 0.04 \text{ pF}$
<i>Measured Capacitance</i>	$C_0 = 5.64 \pm 0.07 \text{ pF}$

VI. DIELECTRIC MEASUREMENTS AND RADAR ATTENUATION ESTIMATION OF ICE/BASALT SAND MIXTURES AS MARTIAN POLAR CAPS ANALOGUES.

This chapter has been published in Icarus 2013. My coauthors are E. Mattei, S.E. Lauro, G. Vannaroni, F. Bella and E. Pettinelli. I conducted the preparation of samples, the measurements, the synthesis and calculation of attenuation rates. E. Mattei, S.E. Lauro, G. Vannaroni and E. Pettinelli guided my work and edited the entire manuscript.

6.1 Abstract

The nature of the materials underlying the superficial deposits of Mars can be inferred, applying an inversion algorithm, from the data acquired by the orbiting HF radars MARSIS and SHARAD. This approach requires the knowledge of the electromagnetic properties of the shallow deposits and an accurate evaluation of the signal attenuation. The present work is focused on the determination of the dielectric parameters of several icy mixtures. I performed the measurements of the complex permittivity, in a wide range of temperature (150-250K) and frequency (20Hz-1MHz), on pure water ice, dry basalt sand and ice/basalt mixtures with different sand volume fractions. The data are presented in terms of attenuation as a function of basalt volume fraction, frequency (20Hz-1MHz) and temperature (150-250K), and discussed in terms of extrapolation to MARSIS and SHARAD frequency bands. The results show that, besides the expected dependence of the attenuation from

temperature, the presence of the solid inclusions in the ice strongly affects the behaviour of the attenuation versus frequency.

6.2 Introduction

Since 2005 the HF radars MARSIS (Mars Subsurface and Ionosphere Sounder) and SHARAD (Shallow Radar) (Picardi, et al., 2004), (Seu, et al., 2004.) have intensively sounded the Martian subsurface, producing hundreds of electromagnetic images of the shallow Mars interior. A large amount of these images were collected on the Martian Polar Caps because the icy materials are particularly transparent to radio waves, resulting in a maximum signal penetration of about 3.7km in the South Pole (Plaut, et al., 2007). In principle, the radar data can also be used to infer the nature of the materials underlying the superficial deposits, applying some robust inversion algorithm and imposing some constraints to the electromagnetic behaviour of such deposits (Zhang, et al., 2008); (Grima, et al., 2009); (Mouginot, et al., 2010); (Mouginot, et al., 2012.); (Carter, et al., 2009); (Lauro, et al., 2010); (Lauro, 2012); (Grima, et al., 2012). In particular, if the goal of the analysis is the conversion of the electromagnetic image into a geological stratigraphy (i.e. the transformation of two-way travel time in depth), the key parameter is the wave velocity which, for low-loss and non magnetic materials, is mainly dependent on the real part of the complex dielectric permittivity.

Note that in the MHz range, the real part of the permittivity of geomaterials (including ice) can usually be assumed frequency independent. On the other hand, if the aim of the prospection is the estimation of the permittivity of the buried materials, the inversion

procedure requires the knowledge of the attenuation, which is dominated by the imaginary part of permittivity.

The Martian Polar Caps are the only areas where the inversion techniques can be considered more reliable, being the H₂O ice the main component of the caps (Plaut, et al., 2007); (Phillips, et al., 2008) even though a variable percentage of CO₂ ice and silicates is also present in the shallow deposits (Mitrofanov, 2002), (Bibring, et al., 2004). It is generally accepted that the North Polar Layer Deposits (NPLD) are made of almost pure water ice (maximum 5% of dust admixtures as estimated by Grima et al., 2009), and the South Polar Layers Deposits (SPLD) are predominantly composed by “dirty ice”, (up to 15% of dust admixtures, as evaluated by (Zuber, et al., 2007); (Li, et al., 2010). In these terrains, which do not have any terrestrial analogue as the dust content in the Earth polar caps is much lower than 1% (Petit, et al., 1999) the inversion procedure is challenging due to the lack of information on the behaviour of the attenuation vs. frequency and temperature. In fact, the inversion procedure applied so far to radar data acquired on the Martian Polar deposits has been addressed assuming rather different attenuation models. For example, (Zhang, et al., 2008) considered a frequency independent attenuation as usually assumed in terrestrial polar ice sheets (Gudmandsen, 1971); (MacGregor, et al., 2007), (Picardi, 2008) used a linear frequency dependence.

The dielectric properties of pure water ice and dry rocks behave differently in terms of temperature and frequency, and have been extensively studied (see for example (Petrenko, et al., 1999); (Guéguen, et al., 1994); (Fujita, et al., 2000) and references therein). However, the ice/rocks mixtures have a much more complex dielectric behaviour, depending on the two phases relative content.

At the ice freezing point and above the Debye relaxation frequency ν_{rel} ($\nu_{rel} \cong 10\text{kHz}$ at $T \cong 273\text{K}$), the real part of pure water ice permittivity is $\varepsilon' = 3.15$ and the imaginary part ε'' decays as ν_{rel}/ν . The ice relaxation frequency is strongly affected by the temperature as ν_{rel} moves towards lower frequencies when the temperature decreases. The cooling process does not modify the value of the real part of permittivity above ν_{rel} but significantly reduces the imaginary part. As a consequence, because the attenuation of pure water ice is proportional to $\nu \varepsilon''/\sqrt{\varepsilon'}$ (see below), any temperature variation will affect this quantity (Fujita, et al., 2000); (MacGregor, et al., 2007). On the other hand, at a fixed temperature, the attenuation of pure water ice can be considered frequency independent in the kHz-MHz range (Gudmandsen, 1971); (Fujita, et al., 2000), i.e. in the operating frequency band of MARSIS and SHARAD. In contrast, both real and imaginary parts of permittivity of dry rocks and soils are usually frequency independent (in the MHz range), and virtually insensitive to low temperatures (Guéguen, et al., 1994); (Rust, et al., 1999). Very little is known about the dielectric behaviour of an ice/grain (rock or soil) mixture as a function of frequency and temperature. The few data available from laboratory experiments are very heterogeneous in terms of mixture composition, frequency and temperature ranges (see for example (Herique, et al., 2002), (Stillman, et al., 2010), (Heggy, et al., 2012)). Moreover, some attempts have also been made to predict the dielectric behaviour of an ice/soil mixture (at fixed frequency) applying a mixing formula (Chyba, et al., 1998); (Nunes, 2006), however the lack of extensive laboratory measurements prevented any validation on the reliability of such predictions.

The present work contributes to filling the knowledge gap that exists regarding the dielectric properties of Martian ice/basalt mixtures.

To this goal, I measured the real part of permittivity and loss of pure water ice, dry basalt sand (60% porosity), ice/basalt mixture with 11.3% sand volume fraction, and ice/basalt mixture with 43% sand volume fraction (which is appropriate to simulate the Basal Unit of the NPLD) (Tanaka, et al., 2008); (Lauro, 2012). The results are presented in terms of attenuation as a function of basalt volume fraction, frequency (20Hz-1MHz) and temperature (150-250K), and discussed in terms of extrapolation to MARSIS and SHARAD frequency bands.

6.3 Methods

The dielectric properties of the samples were measured using an Agilent precision LCR meter HP4284A, operating in the frequency range 20Hz-1MHz; the instrument was coupled to a cylindrical capacitive cell, equipped with guard electrodes (Cereti, et al., 2007), filled with the test material. The inner and outer electrodes have diameters of 2cm and 3cm respectively and the investigated sample volume is approximately 15cm³.

The equivalent circuit of the capacitive cell can be represented by a capacitor, which accounts for the polarizability of the material, in parallel to a resistor, which represents the electric losses. The measured quantities are the capacitance $C(\nu)$ and the loss tangent $\tan \delta(\nu)$. The real part of the dielectric permittivity is related to the capacitance through:

$$\varepsilon'(\nu) = \frac{C(\nu)}{C_0}$$

where $C_0 = 5.62\text{pF}$ is the capacitance of the empty cell. This quantity was measured with the LCR meter and found to be in full agreement

with the theoretical value calculated on the basis of the cell geometry. In what follows the uncertainty in the permittivity $\varepsilon'(\nu)$ is calculated neglecting the uncertainty in C_0 , being this value much smaller than that associated to $C(\nu)$. The capacitive cell is inserted in a cryostat operating with liquid nitrogen, which is capable to cool the sample down to about 100K. However, to cover the temperature profile expected for the Martian Polar Caps from surface down to a depth where liquid water may exist (Larsen, et al., 2000); (Clifford, et al., 2010) the range of temperature was limited to 150-250K. The measurements were performed first dropping the temperature from 273K to 150K and then allowing the system to slowly reach again the temperature of 273K. Each cycle lasted about 24 hours, 6 hours for cooling and 18 hours for warming up. I measured $\varepsilon'(\nu)$ and $\tan \delta(\nu)$ on four different samples: i) pure water ice (with negligible air content); ii) dry basalt sand with a $(40 \pm 1)\%$ grains and $(60 \pm 1)\%$ air; iii) water ice/basalt mixture with $(11.3 \pm 0.2)\%$ grains $(84 \pm 1)\%$ ice and $(5 \pm 1)\%$ air; and iv) water ice/basalt mixture with $(43 \pm 1)\%$ grains $(46 \pm 1)\%$ ice and $(11 \pm 1)\%$ air. The volume fraction of each mixture component was calculated by weighting the sand and the water with a precision scale and using a grain density of $2.978 \pm 0.002 \text{ g/cm}^3$, estimated with a helium pycnometer (Micromeritics). Note that the unwanted residual air content is a consequence of the small dimension of the cell and the filling procedure in the grain/ice mixtures. The ice used in the samples was obtained from bi-distilled water whereas the basaltic sand (having a grain dimension lower than 0.5mm) was collected at Mt. Etna (Italy) from a volcanic non-magnetic sand deposit. The dielectric properties

were measured at 48 stepped frequencies logarithmically distributed within the band 20Hz-1MHz (10 frequencies per decade).

A single frequency sweep lasted about two minutes, and since the system was running continuously during the entire thermal cycle, about 700 curves were acquired for each sample. The measurements presented here refer to the warming up part of the cycle, which is slow enough to ensure both the stability of the temperature during each frequency sweep and the thermal equilibrium inside the sample.

The measured dielectric parameters were then used to evaluate the attenuation vs. frequency which, in case of non magnetic materials, can be expressed as (Ulaby, et al., 1986):

$$A_{dB/km} = 8.68 \cdot 10^3 \left[\frac{2\pi\nu}{c} \sqrt{\frac{\epsilon'}{2}} \sqrt{\sqrt{1 + \tan^2 \delta} - 1} \right]$$

Equation LIX

where c is the speed of light in a vacuum, and A is given in dB/km. In particular, for low-loss materials ($\epsilon''(\nu) \ll \epsilon'(\nu)$) and considering that $\epsilon''(\nu) = \epsilon'(\nu) \tan \delta(\nu)$, the attenuation can be approximated with the following equation:

$$A_{dB/km} \cong 8.68 \cdot 10^3 \left[\frac{\sqrt{2}\pi\nu}{c} \frac{\epsilon''(\nu)}{\sqrt{\epsilon'(\nu)}} \right]$$

Equation LX

6.4 Results and Discussions

6.4.1 Pure water ice

The results, presented in the following figures shown electromagnetic properties ($\epsilon'(\nu)$, $\epsilon''(\nu)$ and $A_{dB/km}$) measured on pure water ice at five different temperatures (150, 175, 200, 225 250K), chosen among all curves collected during each measuring cycle.

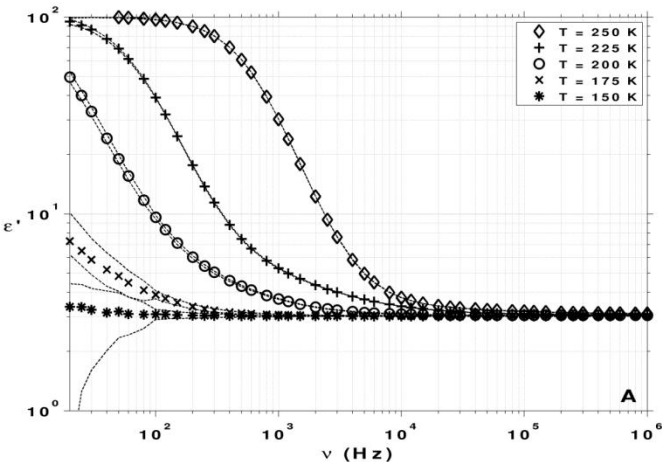


Figure XLVI Real Part of permittivity measured on pure water ice

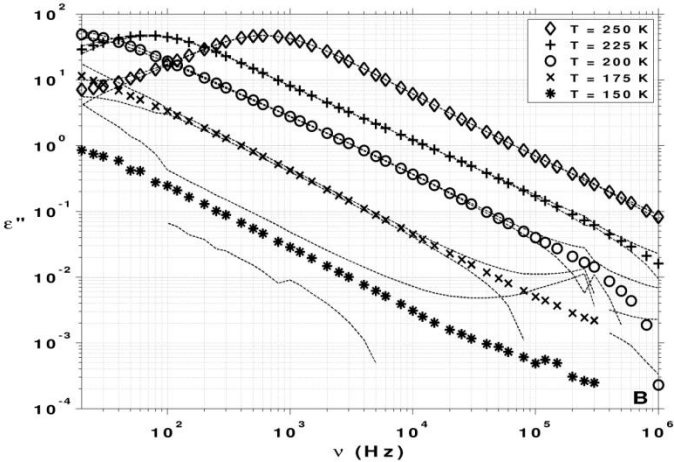


Figure XLV Imaginary Part of permittivity measured on pure water ice

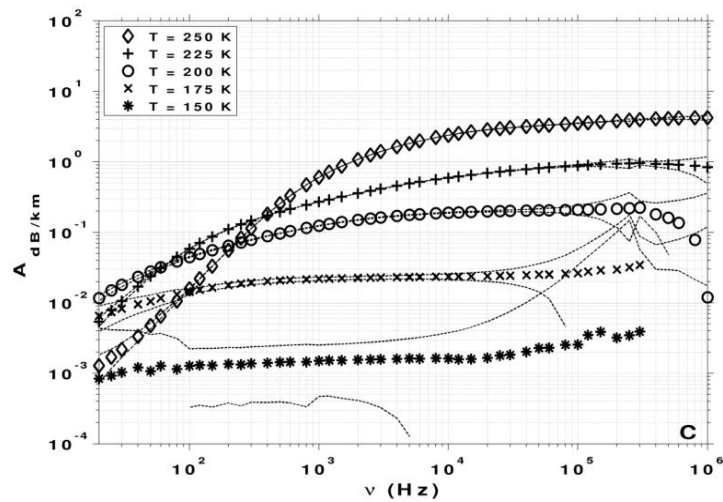


Figure XLVII Attenuation on pure water ice

In particular these figure respectively show the real, imaginary part of permittivity and finally the attenuation calculated according to Equation LIX. The graphs also include the measurement uncertainties that were calculated on the basis of the specifications provided by Agilent for the HP4824A LCR meter, i.e. assuming a type B standard uncertainty with uniform distribution (Kirkup, et al., 2006). The uncertainties are shown through dashed lines which define an uncertainty region around each curve, indicating the envelope of the error bars associated to the measurement points. As illustrated by the plots, the uncertainties in $\varepsilon'(\nu)$ progressively decrease towards higher frequencies, becoming negligible at frequencies higher than about 1kHz. On the other hand, the uncertainties in $\varepsilon''(\nu)$ exhibit a more complicated behaviour being dependent on both frequency and temperature. In fact *Figure XLV*, *Figure XLIX*, *Figure LIII*, *Figure LIV* show that good measurement accuracy is achieved only at intermediate frequencies, getting worse towards higher and lower frequencies, especially at low temperatures.

Note that the $\varepsilon''(\nu)$ curve does not regularly exhibit the uncertainty region lower limit, as at 150K and at some frequencies, the uncertainties become comparable with the measured values and cannot be drawn in a logarithmic scale. This effect is also visible in the low frequency region of the other samples. The uncertainties associated to the attenuation curve shown in *Figure XLVII*, are calculated applying the propagation formula to equation (LI), conservatively assuming the uncertainties totally correlated (Kirkup and Frenkel, 2006).

The graphs of the real and imaginary parts versus frequency for pure water ice (*Figure XLVI*, *Figure XLV*): both graphs show the characteristic Debye relaxation process, which confirms the reliability of the measurements. In particular, in the curve of *Figure XLVI* it is visible the typical drop of $\varepsilon'(\nu)$ from the static value of about 100, to the high frequency expected value of about 3.1. Moreover, the trend of the various curves clearly illustrates the effect of the temperature on the relaxation frequency, which moves leftwards when the temperature drops (e.g. ν_{rel} is of the order of few kilohertz at 250K and much smaller at 150K). Also the $\varepsilon''(\nu)$ curves show the classical relaxation frequency peak, which shifts leftwards when the temperature drops.

Furthermore, as expected, at high frequency the right flank of the peak decreases with a ν^{-1} law. Now, applying *Equation LX* in the region above ν_{rel} , where the real part of permittivity $\varepsilon'(\nu)$ is constant and $\varepsilon''(\nu) \propto \nu^{-1}$, it follows that the attenuation of pure ice is independent from frequency (see *Figure XLVII*).

6.4.2 Dry basaltic sand

Figure XLVIII, Figure XLIX illustrates the results obtained for the dry basaltic sand where, with the exception of the low frequency region dominated by the Maxwell-Wagner phenomena, $\epsilon'(\nu)$ and $\epsilon''(\nu)$ are constant with frequency and temperature. Such a behaviour implies that in a dry “warm” or “cold” environment, according to Equation LX, the attenuation of the basaltic sand always increases linearly with frequency (see Figure L).

This fact is in agreement with the literature on dry rocks (Guéguen, et al., 1994) and references therein), and shows that the presence of air does not affect the dielectric behaviour vs. frequency, but only reduces the values of both real and imaginary parts of permittivity with respect to those of the solid matrix.

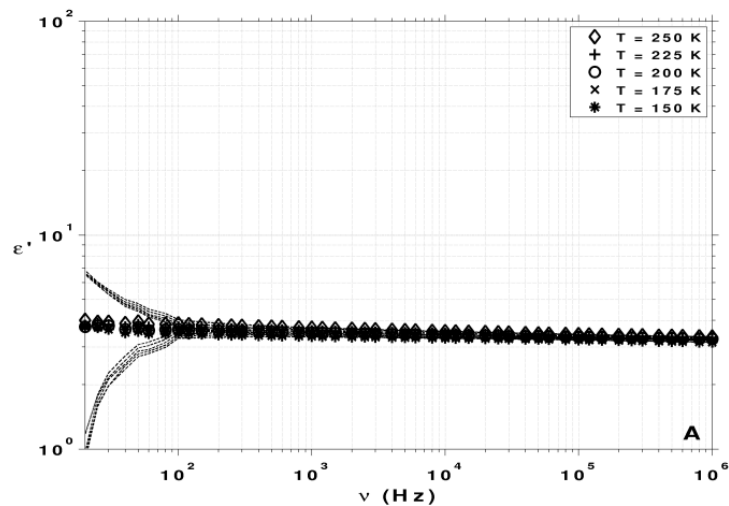


Figure XLVIII Real Part of permittivity measured on dry sand

DIELECTRIC MEASUREMENTS AND RADAR ATTENUATION ESTIMATION OF ICE/BASALT SAND MIXTURES AS MARTIAN POLAR CAPS ANALOGUES.

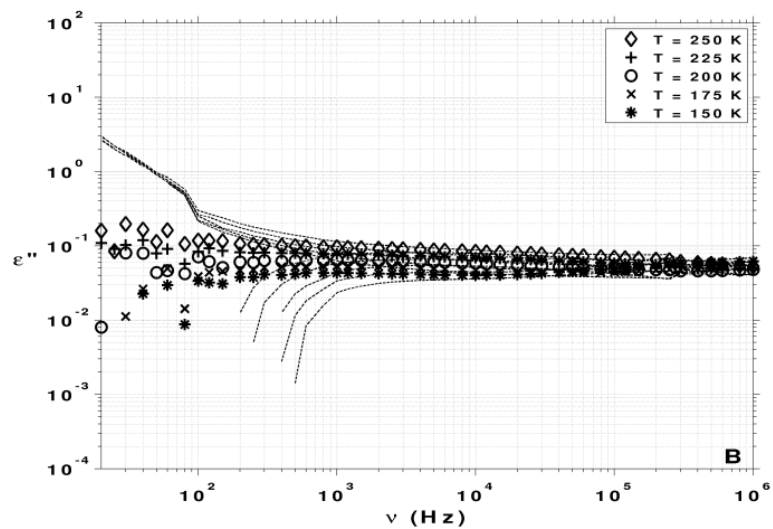


Figure XLIX Imaginary Part of permittivity measured on dry sand

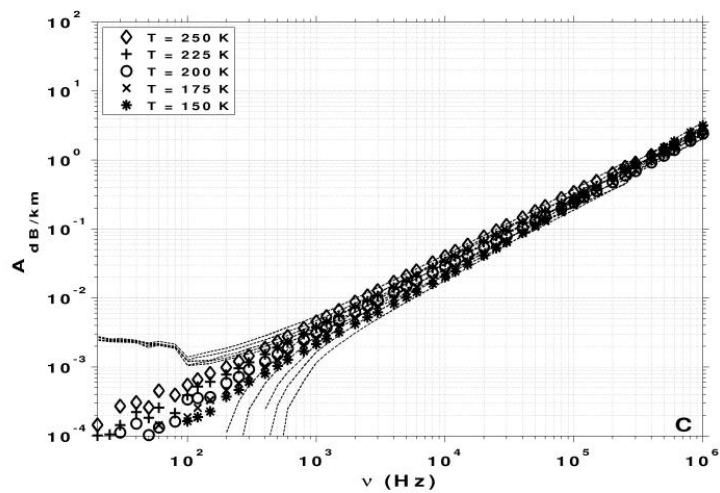


Figure L Attenuation measured on dry sand

6.4.3 11.3% and 43% ice/basalt sand mixtures

Figure LI Figure LII illustrate the real part of permittivity of the 11.3% and 43% ice/basalt sand mixtures.

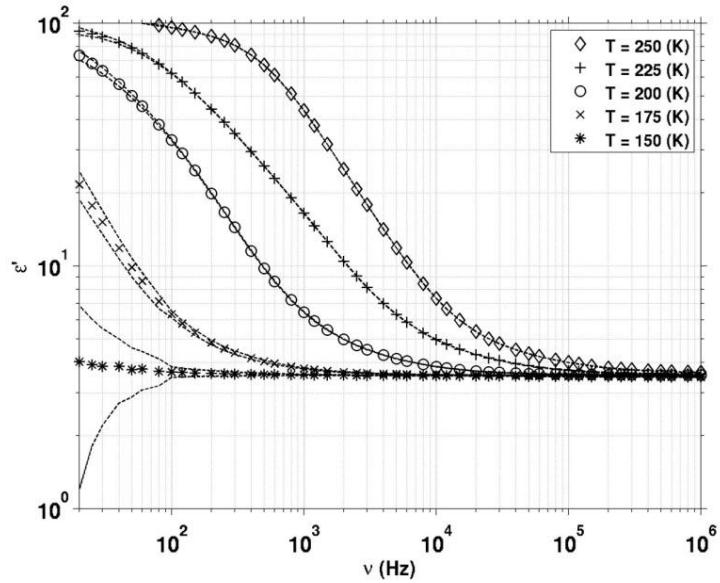


Figure LI Real part of permittivity of the 11.3% and ice/ice/grains mixture at different temperatures

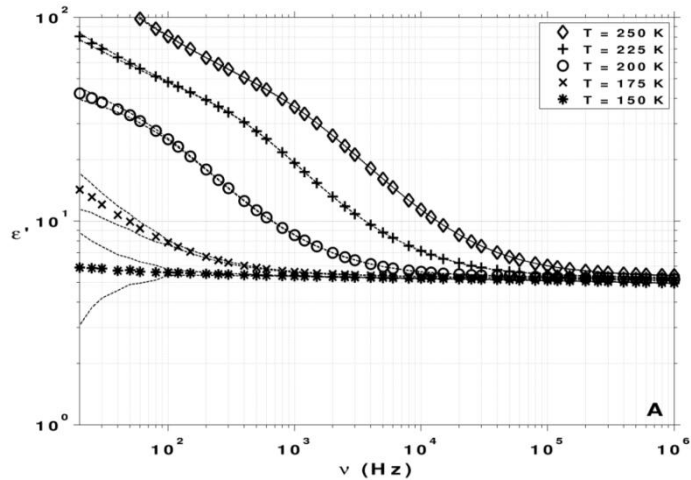


Figure LII Real part of permittivity of the 43% ice/ice/grains mixture at different temperatures

The trends of $\varepsilon'(\nu)$ are similar to the one of pure water ice even though, as expected, the high frequency values of $\varepsilon'(\nu)$ are larger, being 3.5 and 5.0 respectively. On the other hand, the imaginary parts of both mixtures exhibit a more complex behaviour (see *Figure LIII Figure LIV*): at low frequency the $\varepsilon''(\nu)$ curves show a linear decay similar to the one of pure water ice, whereas at high frequency the curves tend to flatten (like in the solid rock matrix) and converge to the 150K $\varepsilon''(\nu)$ curve.

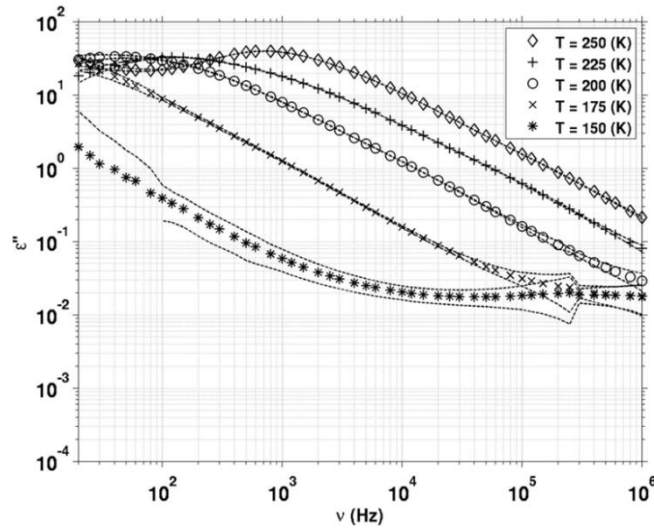


Figure LIII Imaginary part of permittivity measured on 11.3% ice/grains mixture at different temperatures

DIELECTRIC MEASUREMENTS AND RADAR ATTENUATION ESTIMATION OF ICE/BASALT SAND MIXTURES AS MARTIAN POLAR CAPS ANALOGUES.

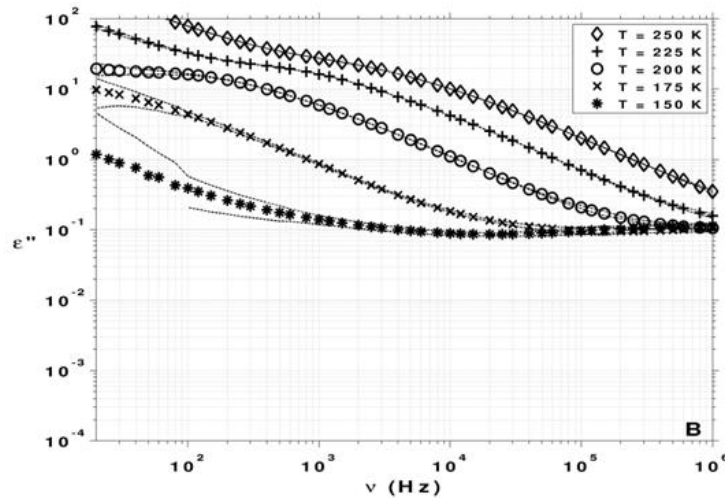


Figure LIV Imaginary part of permittivity measured on 43% ice/grains mixture at different temperatures

This behaviour suggests that the imaginary parts of the mixtures are a linear combination of those of the two components (i.e. ice and solid matrix). Note however that, these two mixtures have a small amount of residual air which, at higher frequencies, slightly reduces the values of both real and imaginary parts of permittivity, whereas, at low frequency, may produce an interfacial polarization (Maxwell-Wagner). The attenuations of the icy mixtures are presented in *Figure LV, Figure LVI*:

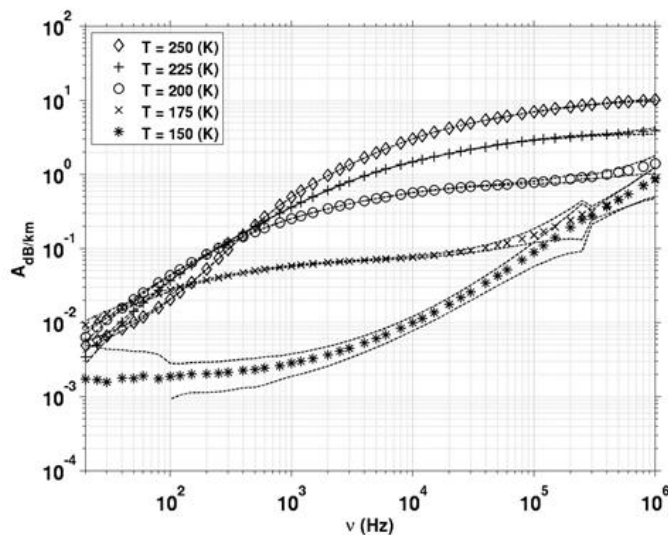


Figure LV Attenuation measured on 11.3% ice/grains mixture at different temperatures.

DIELECTRIC MEASUREMENTS AND RADAR ATTENUATION ESTIMATION OF ICE/BASALT SAND MIXTURES AS MARTIAN POLAR CAPS ANALOGUES.

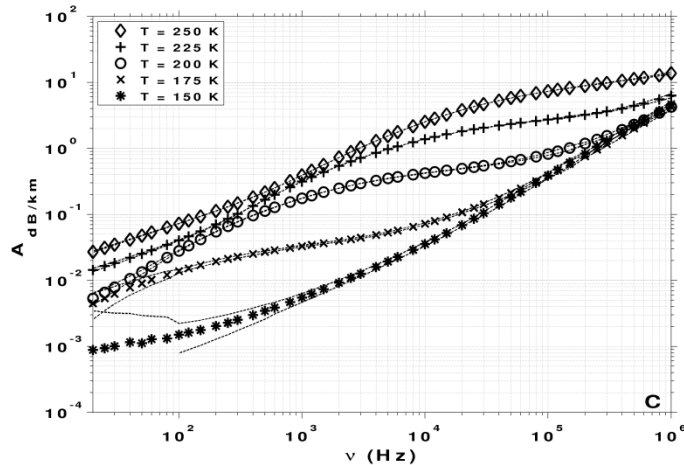


Figure LVI Attenuation measured on 43% ice/grains mixture at different temperatures

both figures illustrate that the curves exhibit a slope which increases at higher frequencies and lower temperatures. I observe that, in the high frequency limit, the lower temperature curves appear to converge to that measured at 150K, which may be interpreted as an “asymptotic attenuation limit” proportional to the frequency according to

$$A_{dB/km} = A_0 \cdot \nu$$

Equation LXI

where ν is expressed in MHz and A_0 is a coefficient which can be estimated from the experimental data. The coefficient A_0 is $0.9 \text{ dB km}^{-1}\text{MHz}^{-1}$ for the 11.3% mixture, $4.2 \text{ dB km}^{-1}\text{MHz}^{-1}$ for the 43% mixture, and $2.4 \text{ dB km}^{-1}\text{MHz}^{-1}$ for the dry basalt.

Figure LV, Figure LVI also show that the approximation of the attenuation with Equation LXI is valid for temperatures below 175K in the case of 11.3% mixture and below 200K in the case of 43% mixture. It is reasonable to suppose that, at higher temperatures, the attenuation curves reach the “asymptotic attenuation limit” at frequencies larger than 1 MHz. To validate such an assumption, I investigated in more

detail the high frequency behaviour of the 11.3% mixture, performing the measurements also with a HP4285A LCR meter, starting from 100kHz up to 20MHz as shown in *Figure LVII*.

The measurements acquired with the two different instruments in the same frequency range (100kHz - 1MHz) are in full agreement (see *Figure LV* and *Figure LVII*.) indicating a satisfactory cross-calibration of the two instruments.

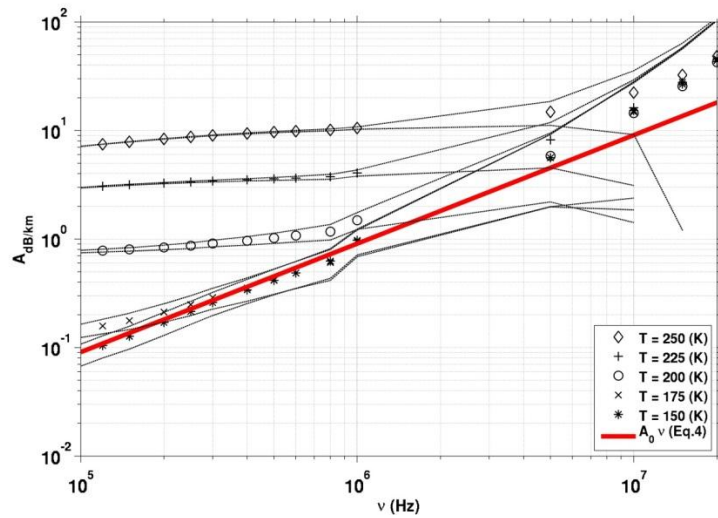


Figure LVII Comparison between measurements performed on the 11.3% mixture with the HP4285A LCR meter (75kHz-30MHz) and the asymptotic curve calculated using equation (LIII).

The red line represents the asymptotic attenuation curve previously discussed using $A_0 = 0.9 \text{ dB km}^{-1}\text{MHz}^{-1}$ and extrapolated up to 20MHz. The data acquired above 1 MHz, follow a linear trend which is slightly offset with respect to the red line. Nevertheless, taking into account for the uncertainty region, such data are still compatible with the red line, i.e. with the asymptotic attenuation curve.

6.5 Final Remarks

The results reported in this chapter highlight the importance of the laboratory experiments to properly characterize the dielectric properties of ice/soil (or rock) mixtures at temperatures typical of Martian surface. In fact, at very low temperatures, the icy mixtures can sometime exhibit unexpected behaviours which, in the frequency band typical of the subsurface penetrating radars, deviate from the properties of pure water ice.

Our measurements show that, besides the expected dependence of the attenuation from temperature, the presence in the ice of the solid inclusions (mineral grains) strongly affects the behaviour of the attenuation versus frequency. In particular, I found that at low frequency and high temperature the behaviour of the pure ice dominates and the attenuation is approximately constant, whereas at high frequency and low temperature the behaviour of the basalt matrix dominates and the attenuation linearly increases with frequency.

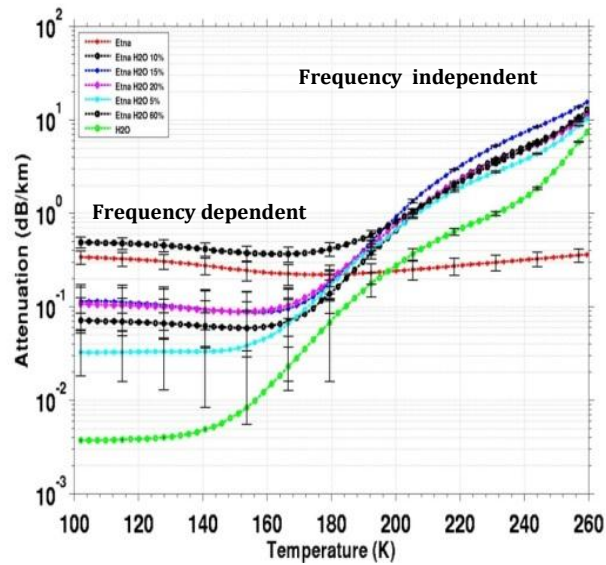


Figure LVIII Comparison between measurements of attenuation performed on the different ice/basalt sand mixture with the HP4285A LCR meter (75kHz-30MHz) and the asymptotic curve calculated using equation (LIII).

Such effect is important when the inversion procedures are applied to radar data collected on planetary dirty ices, even in case of relatively low content of inclusions.

As a conclusion, the estimation of the attenuation should take into account both the temperature profile inside the icy deposits and the distribution versus depth of the grain inclusions.

These findings have important implications not only for the radar sounding of the Martian Polar Caps but, more in general, for any radar application in cold icy materials.

VII. DIELECTRIC MEASUREMENTS OF SALINE ICES UP TO 200K

During the first step of my research I have conducted measurements of dielectric properties of pure and saline ice. In particular I have used the probable salts present within the crust of Europa and Ganymede: $\text{MgSO}_4 \cdot 7\text{H}_2\text{O}$ and anhydrous Na_2SO_4 . All samples were cooled, immersing the capacitive cell (described in the section V), in a polystyrene box containing CO_2 -ice able to reach a minimum temperature of about 200 K, although this is not the typical temperature of the ice crust of these satellites. Also in this case I have used HP4284 LCR meter to evaluate the real and imaginary parts of dielectric permittivity of ice both as function of frequency (20 Hz to 1MHz) and temperature (290 K to 200 K).

The temperature was measured with (Platinum Resistance Thermometers) connected to the KEITHLEY 2700 multimeter and was monitored inside capacitive cell as shown in the *Figure LIX*.

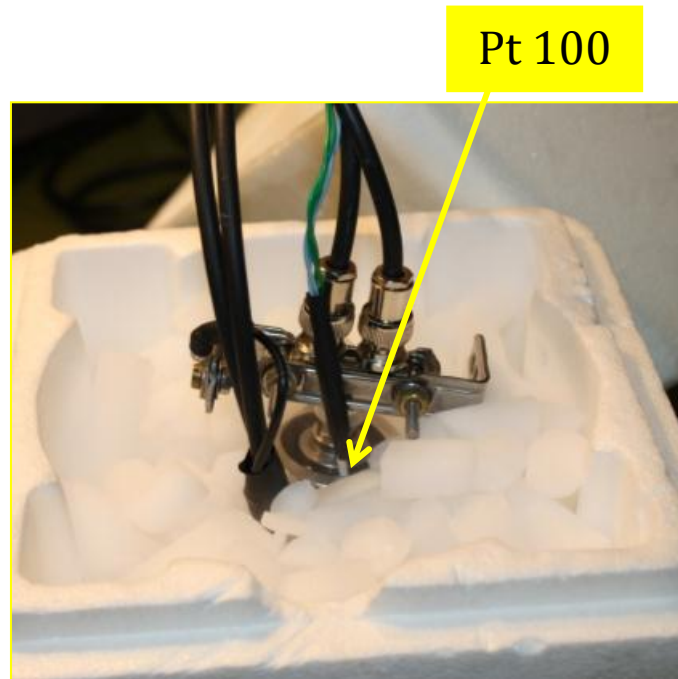


Figure LIX the capacitive cell in the polystyrene box containing CO_2 -ice

We have prepared seven samples, each mixing a different concentration of salt with bidistilled water through a magnetic stirrer, as reported in the following *Table IV*:

	<i>WEIGHT SALTS (g)</i>
C1	0.0049
C2	0.0123
C3	0.0246
C4	0.0469
C5	0.1230
C6	0.2460
C7	2.4600

Table IV Salts concentrations of samples

7.1 Dielectric measurements of $\text{MgSO}_4 \cdot 7\text{H}_2\text{O}$ -ice at different temperatures and concentrations

The results obtained are shown in the *Figure LX* and *Figure LXI*: these plots show real and imaginary part of permittivity at six different temperatures for solution of magnesium sulfate hepta hydrate ($\text{MgSO}_4 \cdot 7\text{H}_2\text{O}$) and at three different concentration of salt. For simplicity only show graphs of some concentrations.

Real part of permittivity at different temperatures

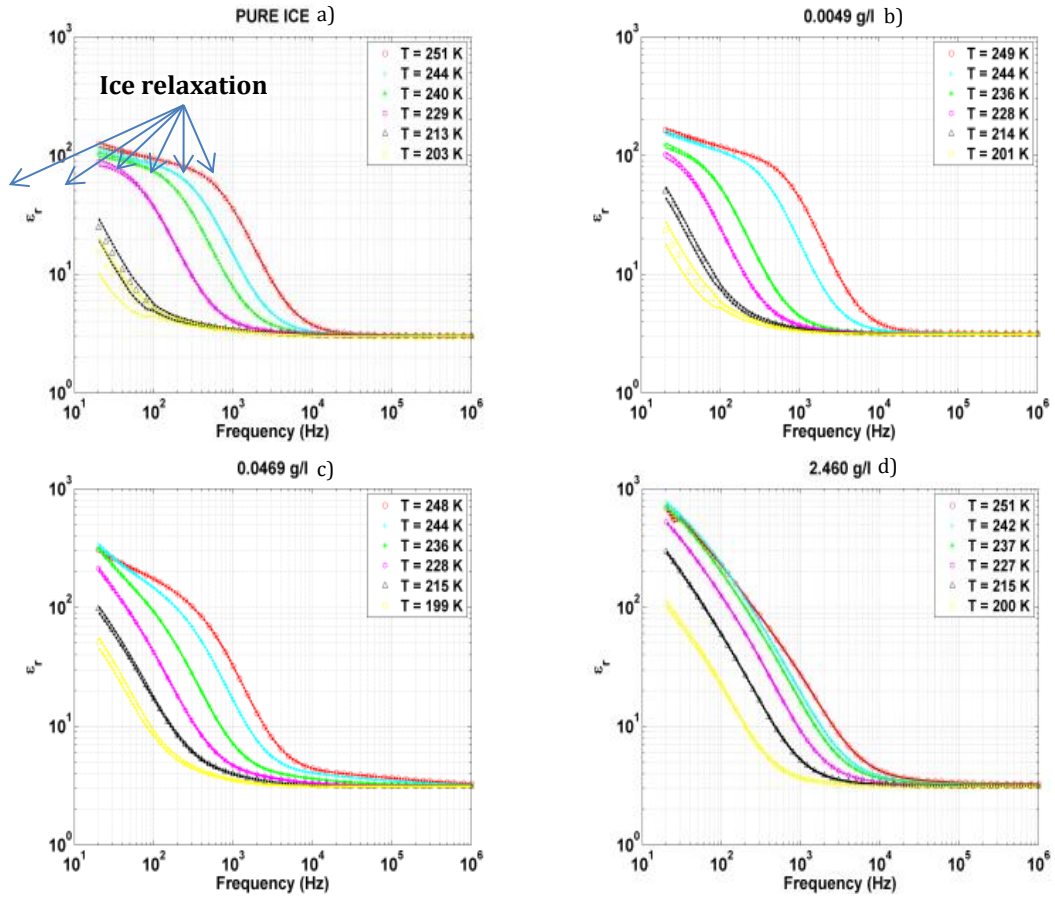


Figure LX Real part of permittivity at six different temperatures of: **a)** Pure ice, **b)** C1, **c)** C4, **d)** C7

Imaginary part of permittivity at different temperatures

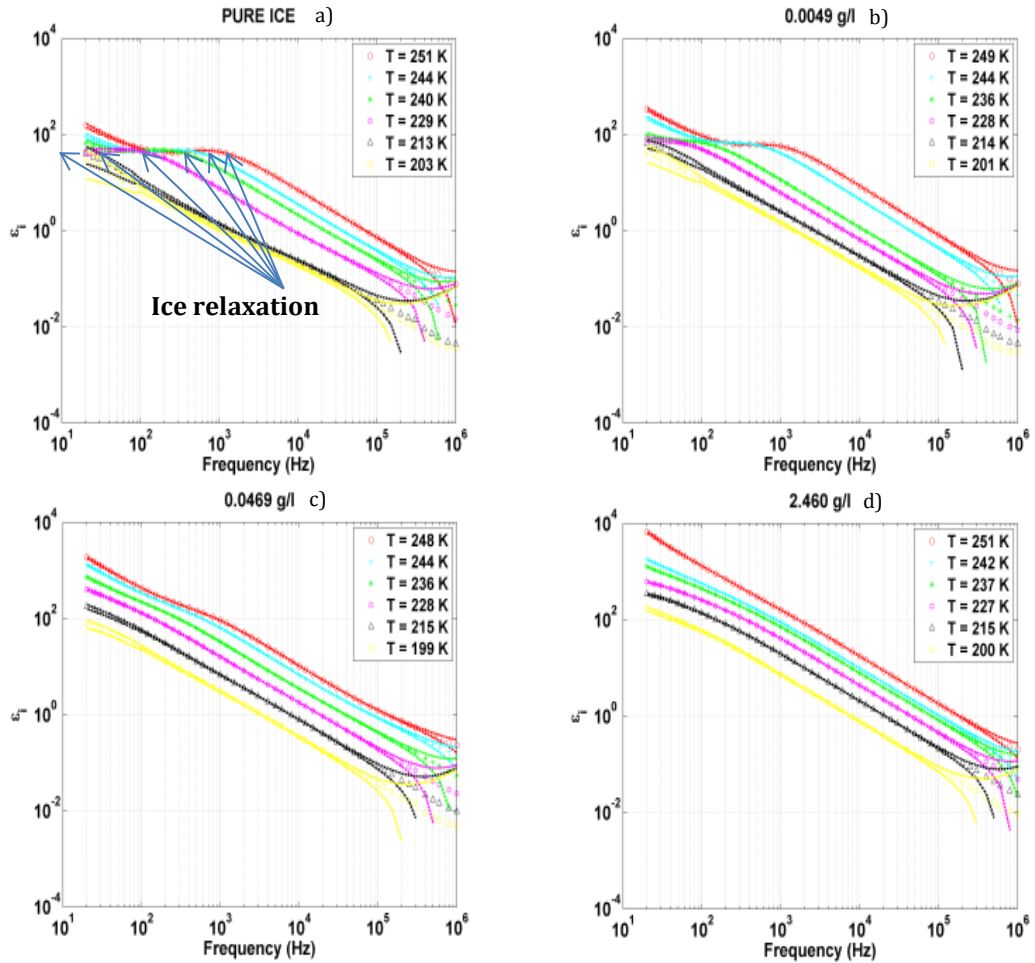


Figure LXI *Imaginary part of permittivity at six different temperatures of: a) Pure ice, b) C1, c) C4, d) C7*

The real and imaginary part decreases as the temperature decreases. The dashed lines define the uncertainties of the measurements obtained propagating the errors of the LCR meter.

The errors are functions of both frequency and impedance levels.

Very interesting is the shift of the frequency of relaxation toward lower frequencies as the temperature decreases.

In a similar manner the imaginary part:

Real part of permittivity at different concentrations

In these graphs *Figure LXII* instead I chose only four temperatures and I have plotted the real part of the permittivity to vary the concentration of the salt and I can see the real part increases as the amount of salt.

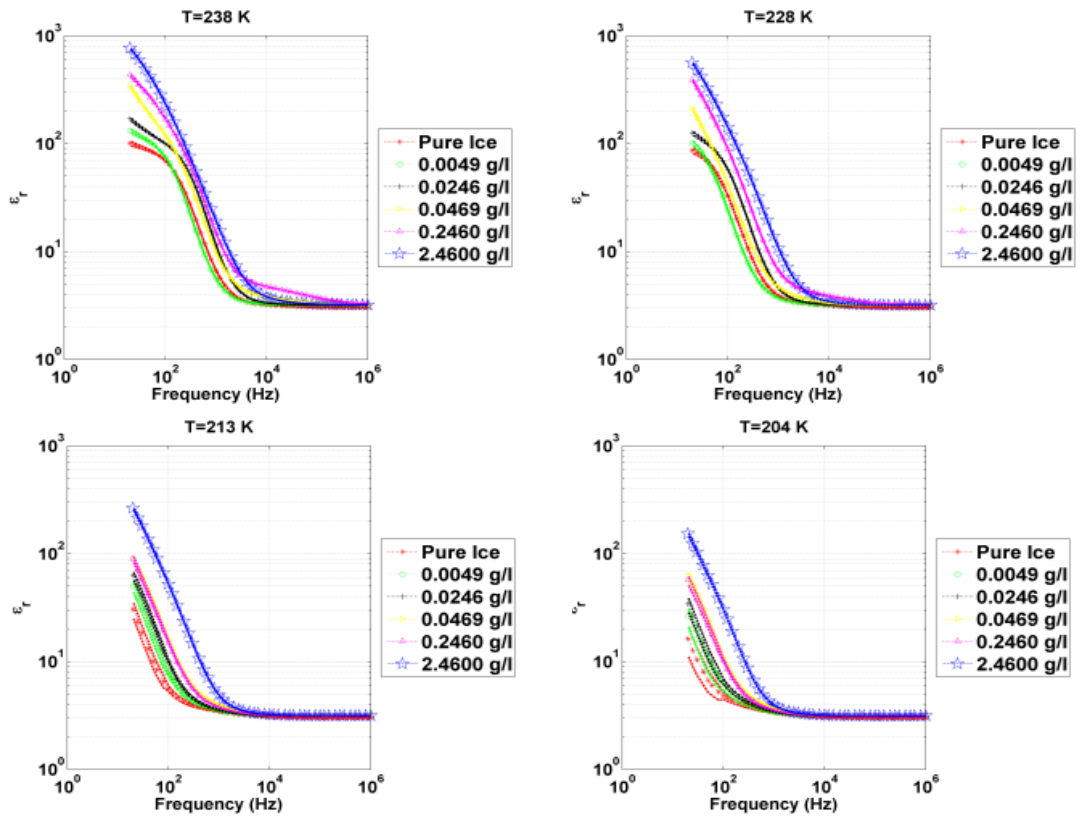


Figure LXII Real part of permittivity at five different concentrations at four different temperatures

Imaginary part of permittivity at different concentrations

The imaginary part *Figure LXIII* shows a similar trend suggesting that the losses become lower and lower with temperature decrease.

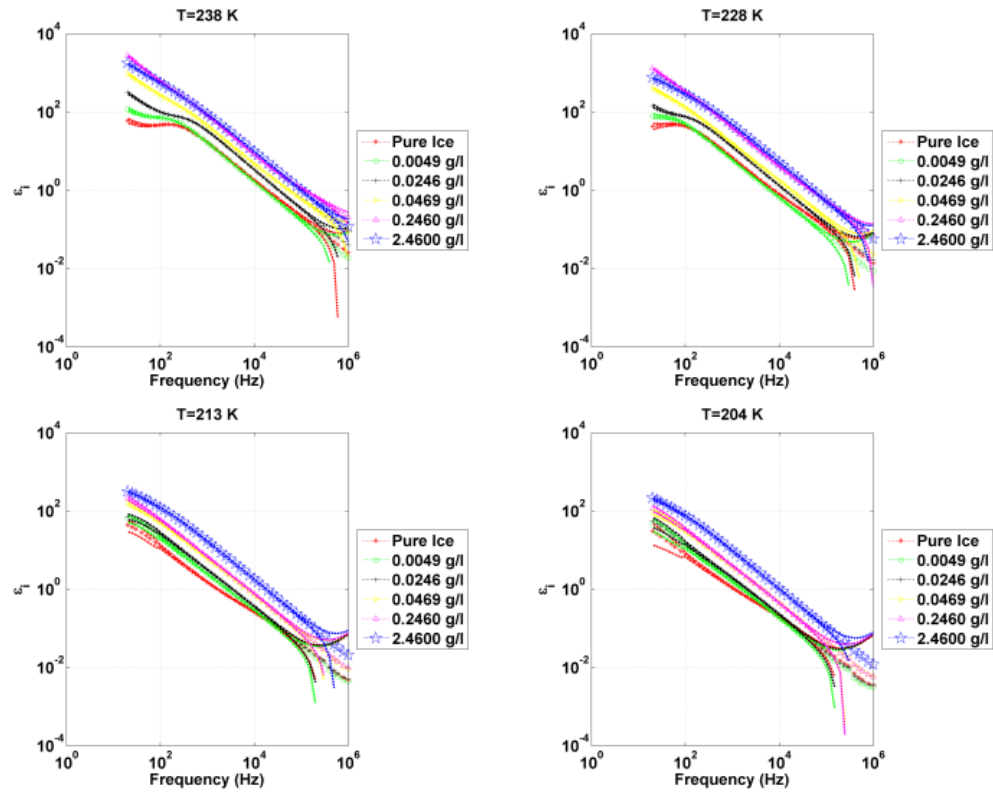


Figure LXIII *Imaginary part of permittivity at five different concentrations at four different temperatures*

7.2 Dielectric measurements of Na₂SO₄-ice at different temperatures and different concentrations

Even with regard to the sodium sulfate find the same trend for both the real part and for the imaginary part *Figure LXIV* and *Figure LXV*.

Real part of permittivity at different temperatures

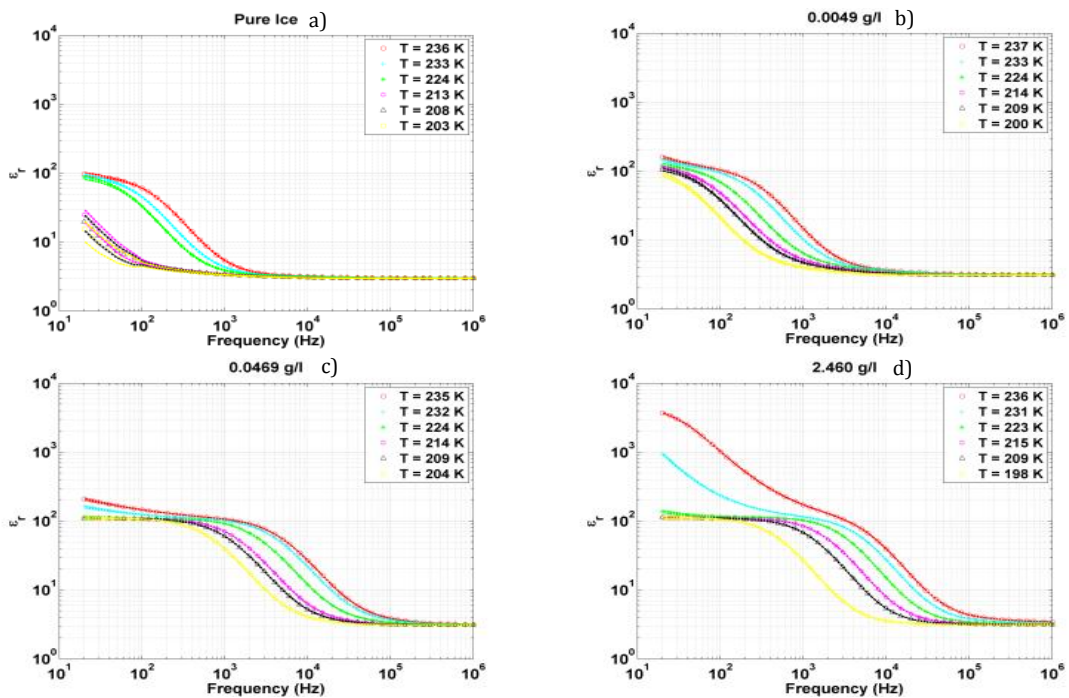


Figure LXIV Real part of permittivity at six different temperatures of: **a)** Pure ice, **b)** C1, **c)** C4, **d)** C7

Imaginary part of permittivity at different temperatures

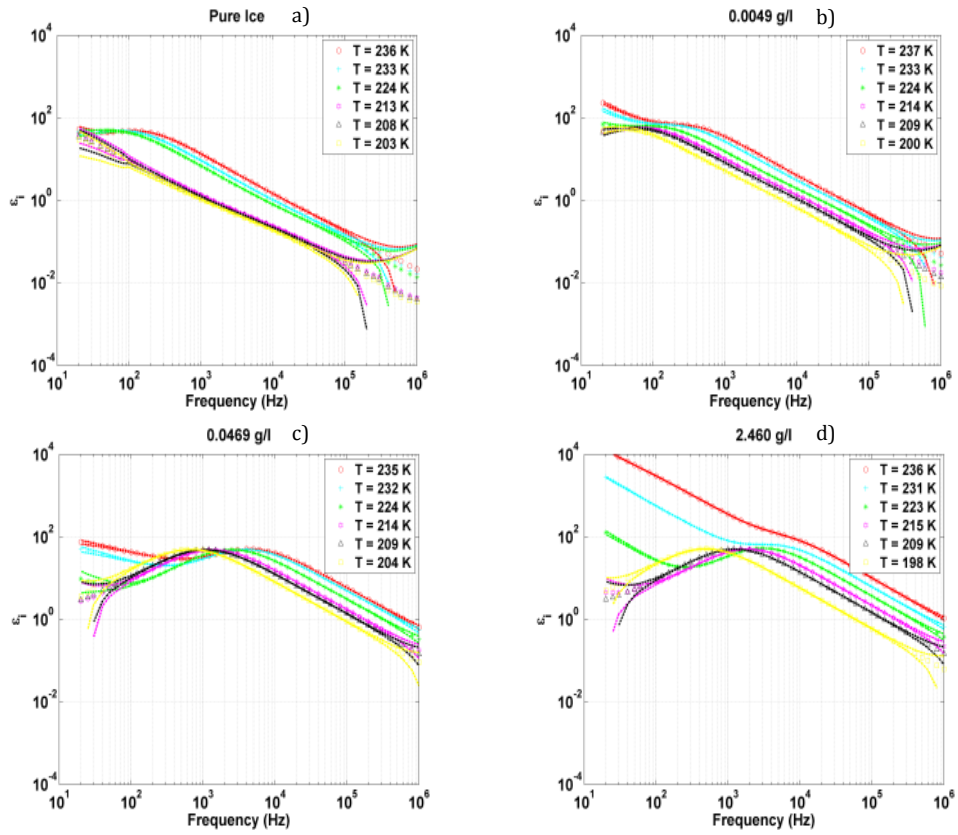


Figure LXV Imaginary part of permittivity at six different temperatures of: **a)** Pure ice, **b)** C1, **c)** C4, **d)** C7

Real part of permittivity at different concentrations

In these graphs Figure LXVI and Figure LXVII instead, I have plotted real and imaginary part of permittivity versus frequency chose only 4 temperatures and I have plotted the real part of the permittivity to vary the concentration of the salt : I can see the real part increases as the amount of salt

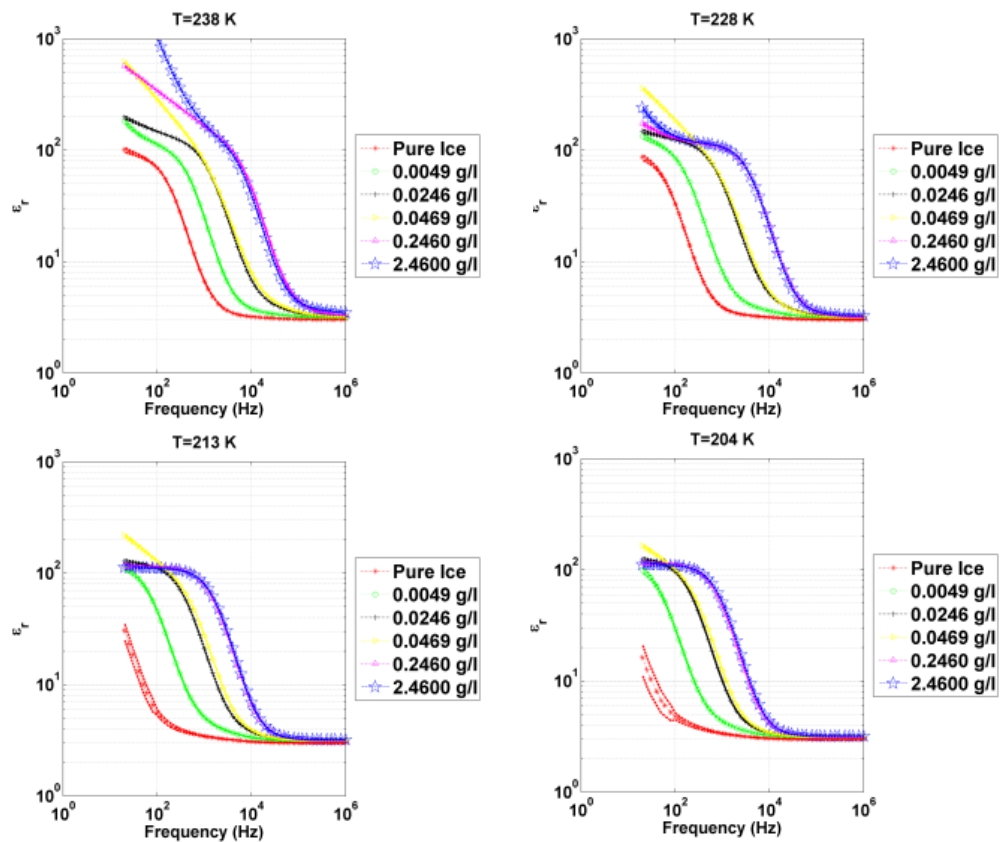


Figure LXVI Real part of permittivity at five different concentrations at four different temperatures

Imaginary part of permittivity at different concentration

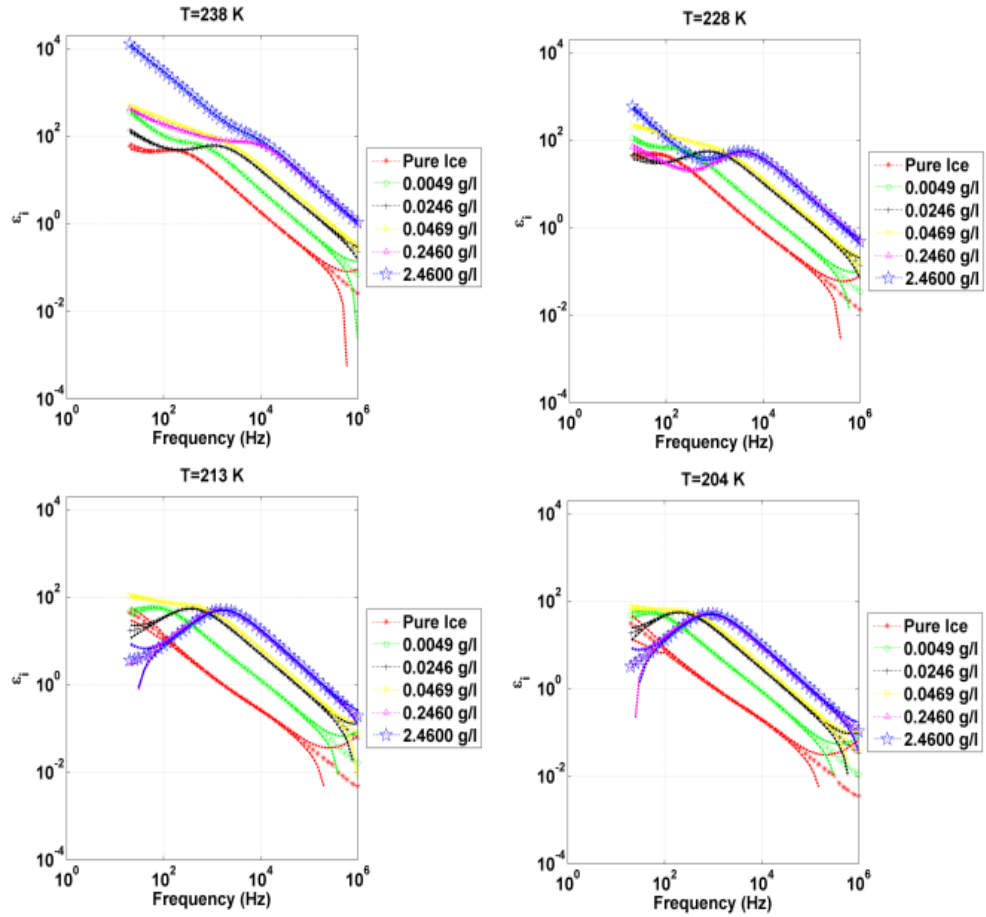


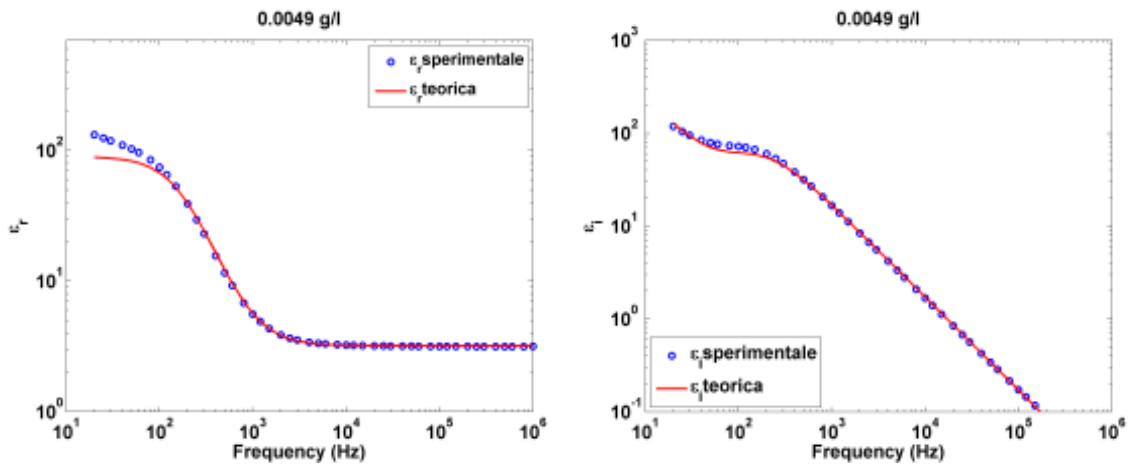
Figure LXXVII Imaginary part of permittivity at five different concentrations at four different temperatures

7.3 FIT with DEBYE MODEL

We assume that the ice samples followed Debye Model (as discussed in the previous section) described by this equation and I can see from these pictures Figure LXVIII that the model fit very well the experimental data for sulfate magnesium:

$$\varepsilon = \varepsilon_{\infty} + \frac{\varepsilon_s - \varepsilon_{\infty}}{1 + j\omega\tau_{rel}} - j \frac{\sigma_{DC}}{\omega\varepsilon_0}$$

MgSO₄·7H₂O sample at C1 concentration



Na₂SO₄ sample at C1 concentration

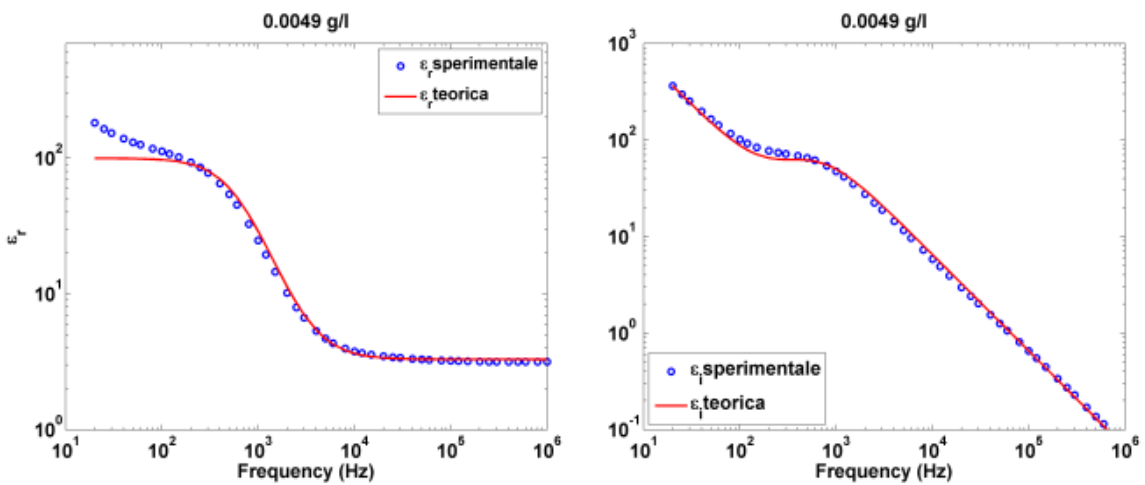


Figure LXVIII Fit with Debye Model of real part of permittivity at C₁ concentration

7.4 Attenuation in dB/km for different salt concentration in ice and fit up to 50 MHz

The real and imaginary parts of the permittivity allow the evaluation of attenuation of the electromagnetic waves through:

$$\alpha = -\frac{\omega}{c} \text{Im} \left[\sqrt{\epsilon^*} \right]$$

$$A(\text{ dB / km }) = 10^3 \times 20 \log_{10} e^{-\alpha}$$

Also in this case for brevity I will show the attenuation calculated for the lower concentration (C1) for each of the two salts at six different temperatures *Figure LXIX* . The attenuation coefficient becomes very small as the temperature decreases

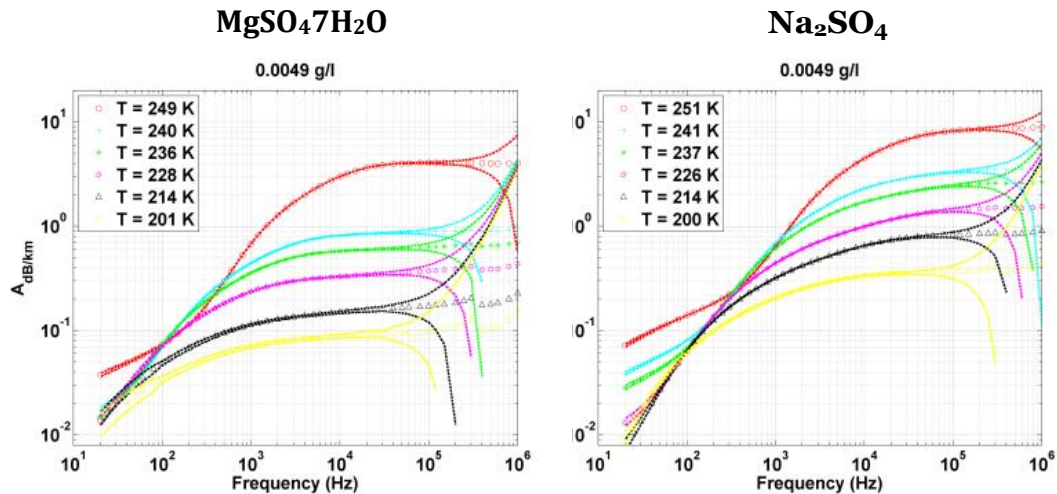


Figure LXIX Electromagnetic Attenuation of both salts at C1 concentration

Finally since the probable frequency penetrating radar is below 50 MHz, I extrapolated our data up frequency limit *Figure LXX*.

We can see an attenuation about few dB per km, since the expected temperature of Ganymede's crust is about 100 K, the attenuation should be lower and so the radar signal should be able to penetrate the icy surface of the satellite.

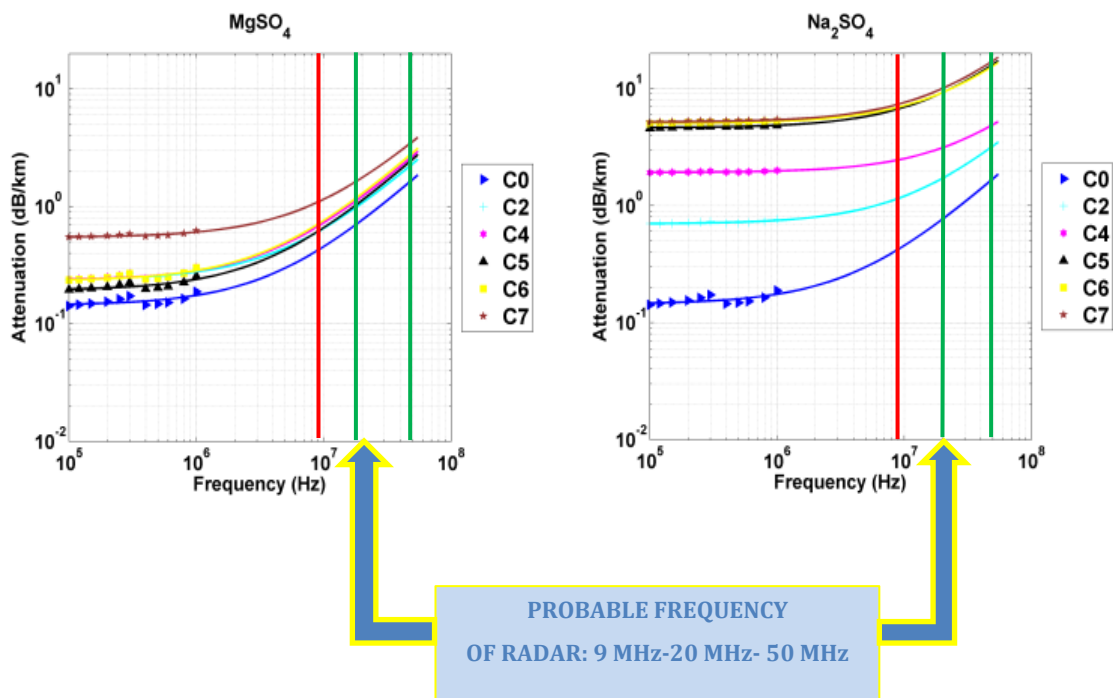


Figure LXX Fit of Attenuation up to 50 MHz of both salts at lower temperature of about 200 K

VIII. DIELECTRIC MEASUREMENTS OF SALINE ICES UP TO 100K

8.1 Introduction

I know, from literature, that the ice containing entrapped salt eliminate this salt under the influence of a temperature gradient through the ice (Whitman, 1926).

The salt diffuses as a brine through the ice towards the warmest part of the ice block. Diffusion will not occur where the ice is below the eutectic temperature T .

The process of diffusion will occur independently of gravity and is satisfactorily explained by the effect of temperature upon the equilibrium relationships between ice and salt solutions.

So, in the second step of my research, to avoid running into this phenomenon, I choose to perform new measurements of saline ices at the eutectic concentration.

These measurements have been completed in the capacitive cell that is inserted in a cryostat operating with liquid nitrogen, which is capable to cool the sample down to about 100K.

Also in this case I have chosen the same salt: $\text{MgSO}_4 \cdot 7\text{H}_2\text{O}$ and Na_2SO_4

8.2 Eutectic Freeze Crystallization

Eutectic freeze crystallization is a process based on crystallization at the eutectic point. This can be explained using *Figure LXXI* which is a typical phase diagram of a salt-water mixture.

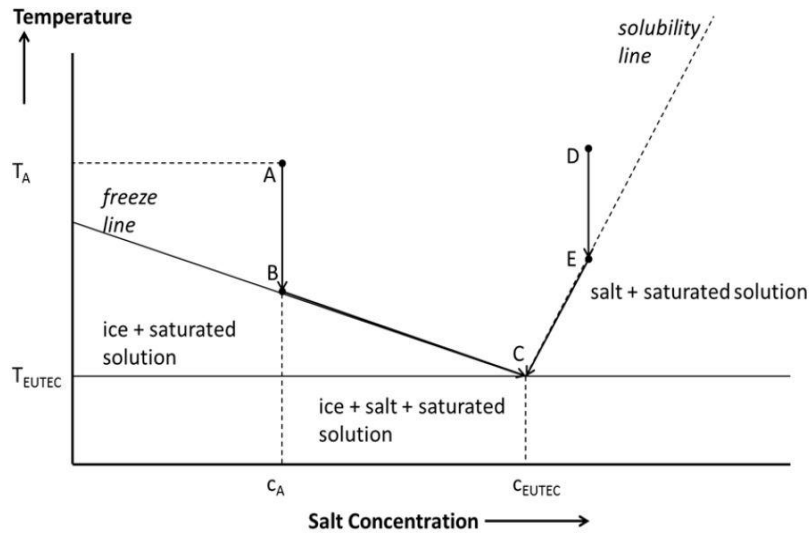


Figure LXXI Phase diagram of a binary salt-water mixture

Take a salt water mixture at point A, with temperature T_A and concentration C_A . By decreasing the temperature of this mixture, eventually point B will be reached. At this point ice crystals will start to form. Point B is a point on the freeze line. This line indicates the concentrations with corresponding temperature at which ice is formed in the mixture.

By creating ice crystals, water is removed from the mixture. This means that the concentration increases and the temperature can be decreased again. This is continued along the freeze line until point C is reached. At point C the freeze line intersects with the solubility line. The solubility line indicates the concentration of salt that is soluble in water at a certain temperature. At point C the concentration cannot become any higher without increasing the temperature. When more ice is

formed the amount of dissolved salt is too high and salt crystals start to form, the salt is no longer soluble in the water. Point C is also known as the eutectic point. Of course, the same principle is also possible with a solution where the concentration is higher than the eutectic concentration. This can be seen in point D, the temperature is decreased again, until the solubility line is reached at point E. At point E, salt crystals are formed and the concentration of the solution is lowered. The temperature can now decrease again, this is repeated until the eutectic point is reached again and ice crystals start to form.

8.3 Dielectric measurements of MgSO_4 -ice and Na_2SO_4 -ice at eutectic concentration

In particular the *Figure LXXII* in the panels a), b), c) respectively show the real, imaginary part of permittivity and finally the attenuation at the eutectic concentration calculated according to the Equation LIX.

The graphs also include the measurement uncertainties that were calculated on the basis of the specifications provided by Agilent for the HP4824A LCR meter, i.e. assuming a type B standard uncertainty with uniform distribution (Kirkup, et al., 2006). The uncertainties are shown through dashed lines which define an uncertainty region around each curve, indicating the envelope of the error bars associated to the measurement points. As illustrated by the plots, the uncertainties in $\varepsilon'(\nu)$ progressively decrease towards higher frequencies, becoming negligible at frequencies higher than about 1kHz. On the other hand, the uncertainties in $\varepsilon''(\nu)$ exhibit a more complicated behaviour being dependent on both frequency and temperature. In fact, *Figure XLII* shows that good measurement accuracy is achieved only at intermediate

frequencies, getting worse towards higher and lower frequencies, especially at low temperatures.

DIELECTRIC MEASUREMENTS OF SALINE ICES UP TO 100K

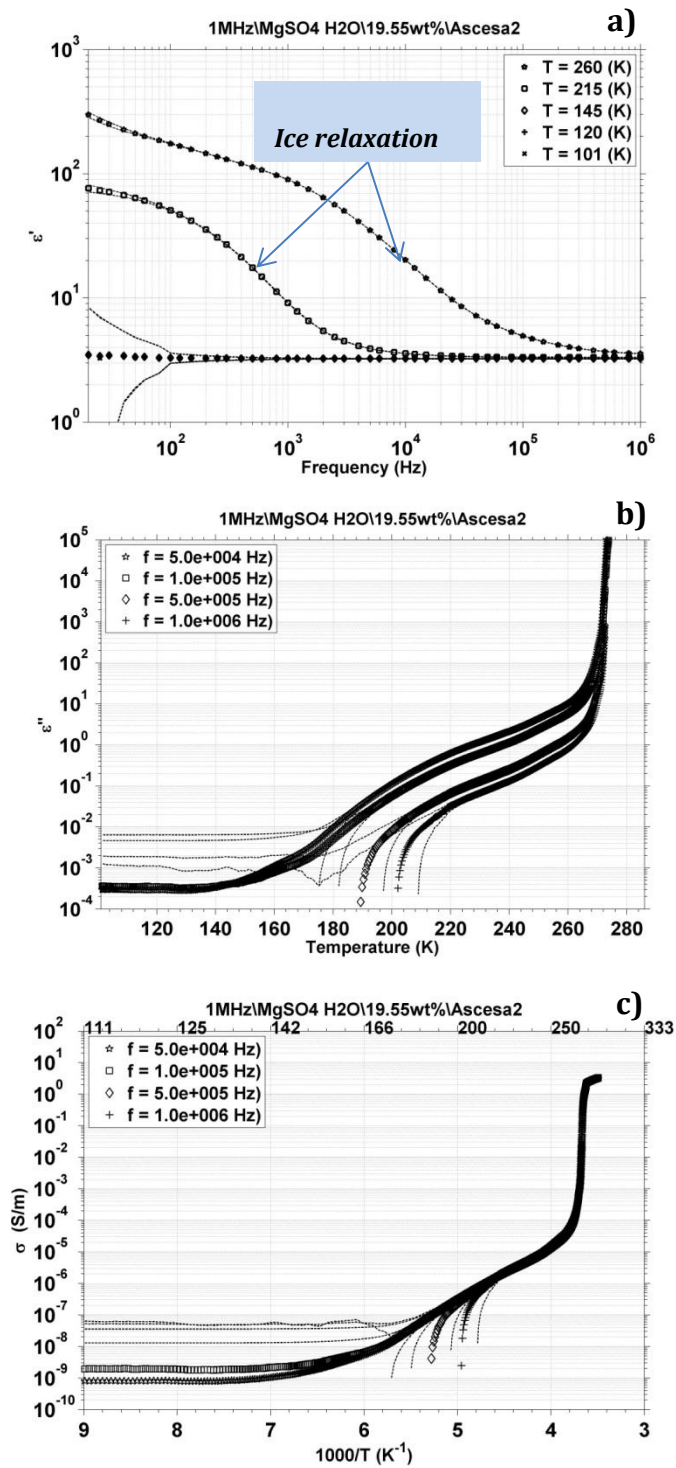


Figure LXXII a) Real part of permittivity, b) Imaginary part, c) Conductivity

In addition we can note that also in this case the real and imaginary part decreases as the temperature decreases, and the shift the frequency of relaxation toward lower frequencies as the temperature drops.

In the similar manner for the dielectric properties of Na_2SO_4 as shown in the following figures.

In the both cases we can see that the attenuation coefficient becomes very small as the temperature decreases, about few dB per km and so the radar signal should be able to penetrate the icy surface of the satellite.

DIELECTRIC MEASUREMENTS OF SALINE ICES UP TO 100K

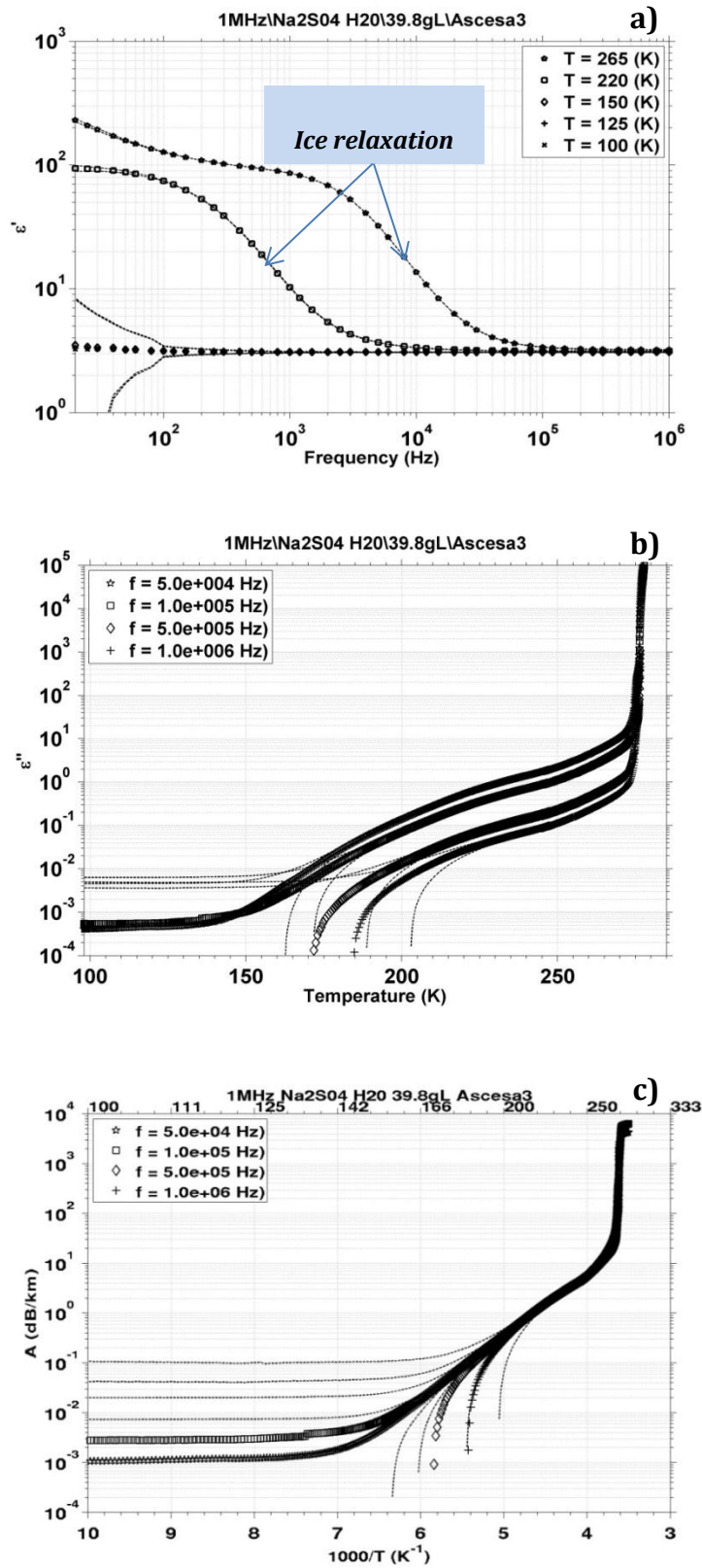


Figure LXXIII a) Real part of permittivity, b) Imaginary part, c) Attenuation

IX. THERMAL MODELS AND ELECTROMAGNETIC ATTENUATION

9.1 Europa - Interior structure and dynamics of the ice shell

Since the first observations performed by the Voyager spacecrafts, the surface of the Jovian satellite Europa revealed a noticeable paucity of large impact craters and a high albedo (Smith, et al., 1979a) (Smith BA, 1979b) (Bierhaus, et al.) related the frequency distribution of the impact craters to the young age of the european crust, estimating a surface age of about 40-90 Ma. The bright surface high albedo was explained by spectroscopic observations (Kuiper, 1957) evidencing that the surface is covered by a high percentage of water ice. After the Galileo mission, the presence of a water ocean beneath the icy crust was inferred by gravity (Anderson, et al., 1998) and magnetic data (Khurana, et al., 1998) and confirmed by tectonic mapping (Carr, et al., 1998) (Pappalardo, et al., 2004). The presence of an induced magnetic field beneath the surface can be addressed to salts dissolved in the water ocean, as demonstrated by the spectroscopic observation of some kind of salts in the surface of Europa (see section 2.3).

Since the surface temperature on Europa is about 100 K, a certain source of heat is necessary in order to prevent the ocean to freeze. Such heat source can be both the radiogenic heating within the rocky mantle of the satellite and the tidal heating due to Laplace resonance associated to the others Galilean moons (Barr, et al., 2009); (Greenberg, 2010). The first has been estimated as supplying $\sim 6-8 \text{ mW m}^{-2}$, and the second having a value of $\sim 10-100 \text{ mW m}^{-2}$ (Tobie, et al., 2003); (Barr, et al., 2009). The tidal dissipation inside the ice shell is usually calculated

considering a Maxwell viscoelastic solid [(Ojakangas, et al., 1989); since the orbital period of Europa [3.5 days] is very close to the Maxwell time for warm ice I, the ice shell could reasonably be in a maximally dissipative state (Ojakangas, et al., 1989). Furthermore, for a Maxwell rheology the volumetric dissipation rate is proportional to the viscosity, which in turn depends on grain size and temperature. As a result, the maximum tidal dissipation occurs in the warmest regions of the ice shell (Barr, et al., 2009), causing local partial melting.

The internal heat transferred from the ocean to the icy crust drives resurfacing processes that originate the peculiar european surface structures (pits, uplifts and chaos). Such features can be explained by two different thickness/dynamics models for the crust capable to dissipate the same heat flux, a thin conductive and a thick convective ice shell (Mitri, et al., 2005); (Barr, et al., 2009) *Figure LXXIV* .

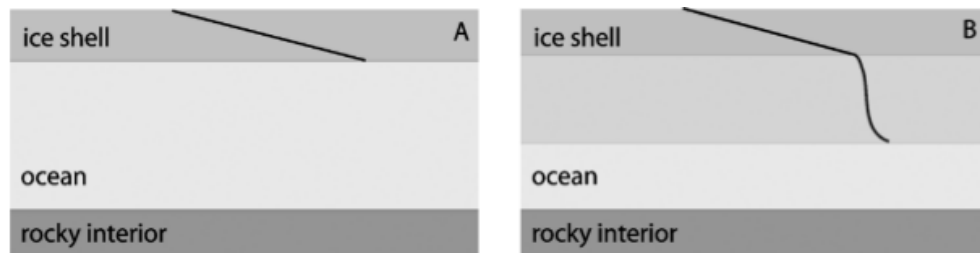


Figure LXXIV Structures and temperature profiles for two possible configurations of the ice shell of Europa. The heat generated in the interior of the planet might be shed by simple conduction through a relatively thin ice shell directly overlying a subsurface ocean (A), or transported equally well through a much thicker ice shell containing of an actively convecting layer (B). Because of the large viscosity near the surface, the ice shell in B develops a stagnant lid at the surface; the convective motions are confined to a sublayer of the ice shell. The states (A) and (B) could have very similar heat fluxes [Mitri and Showman, 2005]

Some authors (Greenberg, et al., 1998) (O'Brien, et al., 2002); (Sotin, et al., 2002) considered that a thin [<10 km] conductive ice shell can produce the observed fracturing of the european surface as a consequence of tidal stress and melting due to the concentration of tidal heating beneath the crust. Other authors support the idea that an ice shell >10 km can be unstable to solid-state convection (Pappalardo, et al.,

1998), (McKinnon, 1999); (Solomatov, et al., 2000); (Tobie, et al., 2003) since the warm ice at the bottom of the shell results less dense than the cold ice at the top. In the convective model, As long as the thermal gradient between the bottom and the top of the ice shell is considerable, the viscosity of the upper part of the ice shell results significantly higher with respect to the bottom layer; in such a condition, a cold “stagnant lid” forms at the top of the ice shell, almost passive to the convection beneath it (Moresi, et al., 1995); (Solomatov, 1995). In the stagnant-lid convection regime, the maximum dissipation and the fluid motion occurs in the sublayer which can be considered as isothermal (Figure LXXIV).

As Europa travels around Jupiter, the tidal heating inside the ice shell could be anything but constant experiencing periodical bursts that perturb the thermal state of the system (Barr, et al., 2009) (Mitri, et al., 2005) demonstrated that for a range of conditions, small perturbations in the heat flux at the base of the ice shell are capable to drive switches between conductive and convective regimes, generating changes in the shell thickness up to 30 km. Such rapid changes in Europa’s volume can generate stresses up to ~10 MPa, inducing significative surface fractures due to the expansion [or contraction], and may have occurred repeatedly in Europa’s history (Mitri, et al., 2005)

Since a significant presence of salts has been observed inside the european ice [see section 2.3], (Pappalardo, et al., 2004) proposed a thermo-compositional convection model in order to explain the generation of domes on the Europa’s surface, if the lithosphere is thin [<0.5 km] and brittle. In this model, diapirism is driven by compositional buoyancy due to differences in impurity levels with respect to the surrounding ice. Partial melting in the ice diapir results in the depletion of salts which drain down into the ocean with the melt, favoring the buoyancy. As a result, Europa’s ice shell will be depleted in low-eutectic

impurities over time. Such a model has been demonstrated to be valid by (Han, et al., 2005) if the european surface is weak and brittle. For a more extensive review of the literature concerning heat transfer, rheology and resurfacing on Europa, the interested reader is addressed to (Barr, et al., 2009).

One of the main physical quantities that govern the thermal profile inside the crust (especially in a pure conductive regime) is the heat flux at the bottom of the shell. Estimations of such quantity were performed by many authors on the basis of geological considerations, rheological studies and convective models. In

Table v the main estimations of the heat flux (both radiogenic or tidal) performed by different authors are presented. Since the concentration of radiogenic elements in the Galilean satellites is substantially unknown, in order to estimate the radiogenic heating the chondritic composition is usually considered as a reference (Spohn, et al., 2003).

Study	Basal heat flux (mW m ⁻²)
Ojakangas and Stevenson [1989]	~ 10
Deschamps and Sotin [2001]	< 50
Husmann et al. [2002]	~ 20
Nimmo and Manga [2002]	> 90
Tobie et al. [2003]	< 50
Sotin and Tobie [2004]	~ 8
Showman and Han [2004]	50-70
Mitri and Showman [2005]	20-60
Moore [2006]	20-65

Table V Estimation of the basal heat flux for Europa

The depth of the ocean is a vital information for the radar exploration of the icy crust. Estimations of the ice shell thickness were performed studying the evolution of the satellite's surface, crater morphology, crater size-distribution and convective processes.

Study	Ice shell thickness (km)
<i>Ojakangas and Stevenson</i> [1989]	≤ 30
<i>Pappalardo et al.</i> [1998]	3-10
<i>McKinnon</i> [1999]	6-26
<i>Hussmann et al.</i> [2002]	30-60
<i>Sotin et al.</i> [2002]	35
<i>Tobie et al.</i> [2003]	20-25
<i>Nimmo et al.</i> [2003]	~ 25
<i>Sotin and Tobie</i> [2004]	~ 50
<i>Showman and Han</i> [2004]	≤ 50
<i>Moore</i> [2006]	> 16
<i>Hand and Chyba</i> [2007]	≤ 15

Table VI Estimation of the Europa ice shell thickness

A value of 25-30 km seems to be accepted by the most of the authors, anyway there are some different estimations.

Considering a conductive shell as depicted in *Figure LXXIV*, in *Table VI* the estimations of the different layer thicknesses are listed.

9.2 Ganymede - Interior structure of the ice shell

Similarly to Europa, also Ganymede presents a H₂O rich surface. Voyager spacecrafts revealed a surface characterized by two main features: heavy cratered regions with low albedo, alternated to a younger brighter terrain consisting in a series of roughly parallel ridges and troughs (Smith, et al., 1979a), (Smith BA, 1979b) Such grooved terrain indicates that the satellite experienced an intense tectonic resurfacing in the past (Greenberg, 2010) probably due to an enhanced tidal heating connected to a 3:2 resonance phase (Spohn, et al., 1998).

With respect to Europa, the ocean inside Ganymede is supposed to be at a higher depth. Some authors supposed a shell thickness of about 150 km (Sotin, et al., 2004), (Kuskov, et al., 2005), (Seufert, et al., 2011). Such a value could be reasonably decreased to 60-80 km if the ammonia is present in the ocean (McKinnon, et al., 1986), (Spohn, et al., 2003).

The internal heat flux for Ganymede is supposed to be mainly due to the presence of radiogenic elements inside the satellite. The effect of tidal flexing is reduced with respect to Europa and is supposed to be around 2-5 mW m⁻² (Deschamps, et al., 2001).

Since the icy shell is thicker with respect to Europa, the thermal gradient inside the crust of Ganymede is slight and the temperature at a depth of 9 km is supposed to be around 120 K (*JUICE-RIME*).

9.3 Thermal conductivity

The thermal conductivity of a solid material is a property defined as the ratio between the heat transmitted across a unit area per unit time to the temperature gradient normal to the area (Hobbs, 1974). Considering a conductive regime for an ice shell, the Fourier's law governs the thermal profile from the bottom to the top of the shell:

$$q = k(T) \frac{(T_t - T_b)}{D}$$

Equation LXII

where q is the basal heat flux (W m⁻²), T_t and T_b are respectively the temperatures at the top and the bottom of the shell, D is the shell thickness and $k(T)$ the thermal conductivity of the ice.

As explicitly reported in Equation LXII the thermal conductivity depends on temperature, and this proportionality has to be considered in the calculation of the thermal profile. Furthermore, the thermal conductivity of a material depends also on pressure, porosity, composition and structure. Exhaustive reviews on the rheology and the thermal properties of solar system ices were performed by (Ross, et al., 1998) and (Durham, et al., 2010). Since this work deals with the crusts of the Galilean satellites, there will be considered the thermal conductivities of some materials observed or expected to these moons.

9.3.1 Thermal conductivity of ice I_h

Independent measurements and estimations of the thermal conductivity of ice I_h in the temperature range valid for Europa and Ganymede were performed in the past by many authors (Ratcliffe, 1962), (Dillard, et al., 1966), (Ross, et al., 1977), (Ross, et al., 1978); (Andersson, et al., 1980), (Klinger, 1980), (Slack, 1980), (Petrenko, et al., 1999). In

Table vii the fit equations, the temperature range and the pressure used for the measurements by the different authors are listed. As shown in ***Errore. L'origine riferimento non è stata trovata.***, the descending behavior of k with the temperature is noticeable for all the different models, but especially at low temperatures any differences become significant. Unfortunately, more recent and accurate measurements of the thermal conductivity in the temperature range useful for the Galilean satellites are not available. Furthermore, (Andersson, et al., 1980) and (Slack, 1980) demonstrated that around 175 K, the T^{-1} dependence of k is not strictly respected, as also noticeable from the fitting curves of (Ross, et al., 1977), (Ross, et al., 1978) in

Table vii.

In *Figure LXXVI* the thermal profile inside an icy moon is shown considering the temperature dependent models of thermal conductivity reported in Table V. The growing depth causes divergence between the models; at a depth of 9 km a difference up to 30 K comes from the choice of the thermal conductivity model.

Author	Temperature range (K)	Fit curve for $k(T)$
Ratcliffe [1962]	120-273	$780/T - 0.615$
Dillard and Timmerhaus [1966]	110-273	$488.19/T + 0.4685$
Ross <i>et al.</i> [1977]	120-270	$786/T^{1.05}$
Ross <i>et al.</i> [1978]	120-270	$335/T + 3.27 - 0.00881T$
Klinger [1980]	> 25	$567/T$
Yen [1981]	40-270	$9.828\exp[-0.0057T]$
Petrenko and Withworth [1999]	*	$651/T$

Table VII Fit equations for $k(T)$ for ice I_h

* Not reported.

Even if the phase I_h is surely present on the icy crusts of Europa and Ganymede, around a pressure of 0.2 GPa there is the transition to the phase II (or III, depending on temperature); such a condition causes an abrupt decline in the thermal conductivity (furthermore decreases the melting temperature down to ~250 K), and could be reached at the depth of about 150 km for Europa and 140 km for Ganymede. Such a solid-state phase transition would cause also a change in rheology, determining variation in the internal dynamics of the satellites. Thermal conductivity measurements of different ice phases are reported in (Ross, *et al.*, 1977), (Ross, *et al.*, 1978). Anyway, since the depth that is supposed to be reached by the radar RIME is around 9 km, it is reasonable to consider only the I_h phase of the ice.

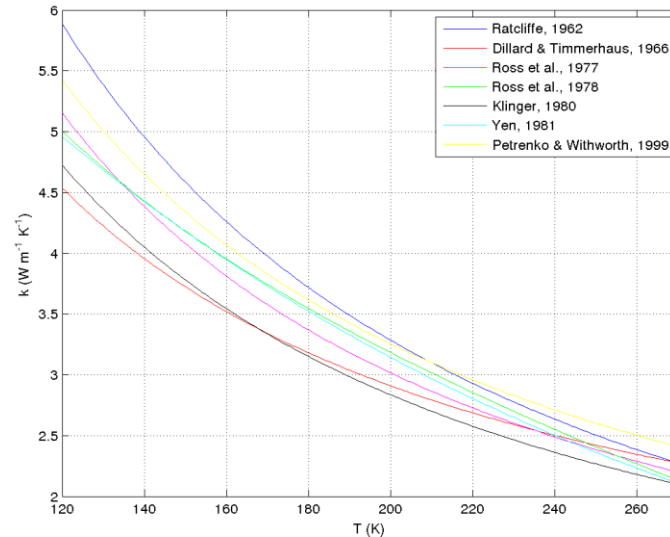


Figure LXXV Temperature-dependent thermal conductivity fit obtained by different authors for ice Ih

Measurements of thermal conductivity of porous ice (Steiner, et al., 1991), and amorphous ice (Andersson, et al., 1994) were also performed to study and simulate the Measurements of thermal conductivity of porous ice (Steiner, et al., 1991); and amorphous ice (Andersson, et al., 1994) where also performed to study and simulate the composition and thermal properties of comets, but considering the cases of the Galilean satellites, these kind of ices can be neglected; even if amorphous ice has been observed at the surface, it is not supposed to be present in the interior of the planetary ice shells (Spohn, et al., 2003).

Studying the thermo-dynamical state of icy satellites, some authors [(Hussmann, et al., 2002); (Nimmo, et al., 2003), (Spohn, et al., 2003), (Sotin, et al., 2004), (Moore, 2006), (Mitri, et al., 2005), (Rudolph, et al., 2012) considered a mean constant value of k for ice I_h , mainly because they studied the thermodynamics of the ice shell by means of numerical codes for solid state convection that does not enable the use of a temperature dependent thermal conductivity. In some cases (McKinnon,

1999), (Tobie, et al., 2003), (Barr, et al., 2005), (McKinnon, 2006), (Mitri, et al., 2008), (Barr, et al., 2009), (Mitri, et al., 2010), corrections were applied in order to consider the effect of the temperature-dependent thermal conductivity in the estimation of heat fluxes and convective lid thickness. Anyway, if the ice shell is sufficiently thick, such an approximation can be a source of uncertainty (Ojakangas, et al., 1989) extracted the thermal profile for Europa inserting the temperature dependence of k directly in the time-independent thermal diffusion equation, and the same model was followed by (Chyba, et al., 1998) and (Moore, et al., 2000) in order to extract the attenuation of the radar signal in the ice shell. A temperature-dependent thermal conductivity was also considered by (Nimmo, et al., 2002) to model the convective diapirism on Europa.

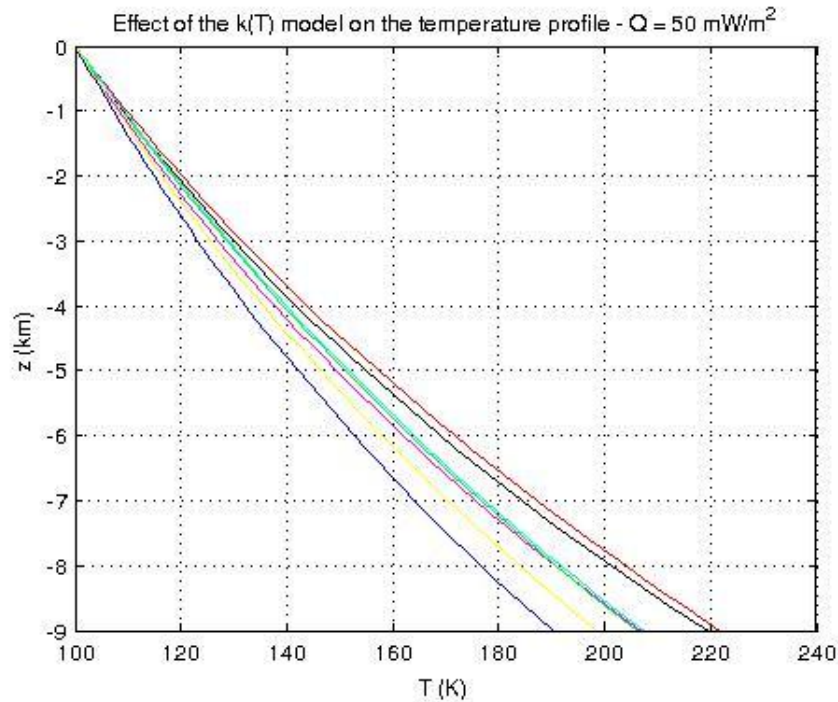


Figure LXXVI *Effect of the thermal conductivity model on the thermal profile for a pure conductive lid.*

9.3.2 Thermal conductivity of salts

As reported in section 2.3 the Europa ice could reasonably contain the presence of some salts, mostly Na_2SO_4 and $MgSO_4$.

Measurements of the thermal and mechanical properties of some hydrated Na_2SO_4 and $MgSO_4$ where performed by many authors in order to simulate the european ice (Durham, et al.), (McCarthy, et al., 2007), (Golding, et al., 2013). Measurement of thermal conductivity of $Na_2SO_4 \cdot 7H_2O$ (mirabilite) and $MgSO_4 \cdot 7H_2O$ (epsomite) at low temperature (173-298 K) where performed by (Prieto-Ballesteros, et al., 2005); in *Figure LXXVI* their results are compared to the thermal conductivity of Ice Ih and others icy materials interesting for icy satellites. As shown in this figure , the thermal conductivity of mirabilite and epsomite is an order of magnitude lower with respect to the ice Ih, and the temperature dependence is different.

In a model considering an ice with an certain concentration of salts, an effective thermal conductivity from the combination of k_{ice} and k_{salt} must be considered *Figure LXXVII* shows the thermal profile for Europa obtained considering pure water ice, epsomite and the eutectic mixture of ice and epsomite obtained by (Prieto-Ballesteros, et al., 2005). Another element that could reasonably be present in the european ice is the chlorine. As reported in section 4.5 the effect of the Cl^- ions inside the ice lattice could influence significantly the electrical properties. The most probably salt containing chlorine is $NaCl$. The values of thermal conductivity obtained for sodium chloride by (Håkansson, et al., 1986) at low pressure are also in agreement with previous measurements of (McCarthy, et al., 1960). Since the value of k for $NaCl$ is significantly higher than that of pure ice, the effect on the resulting thermal conductivity could be significative.

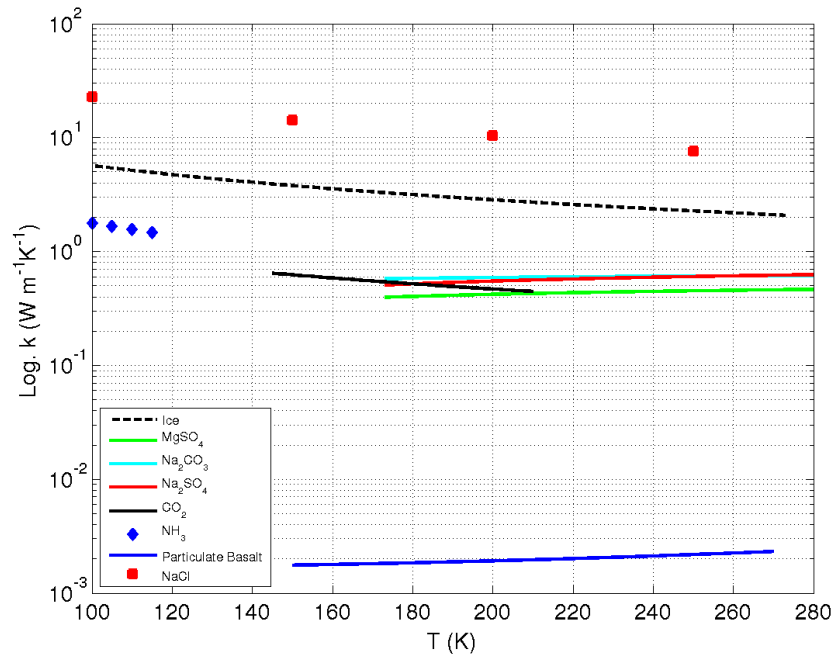


Figure LXXVIII $k(T)$ of epsomite and mirabilite [Prieto-Balesteros and Kargel, 2005] compared to the ice

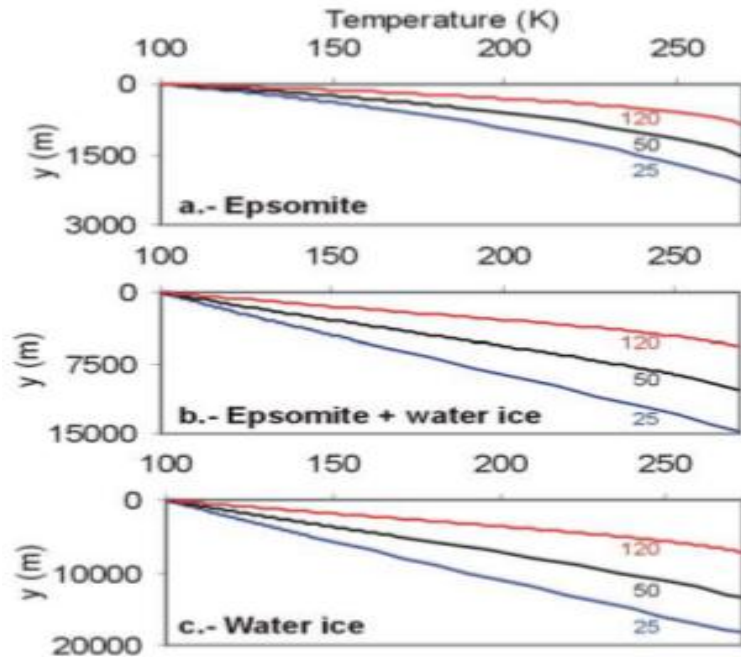


Figure LXXVII Thermal profile of Europa considering ice Ih, epsomite and the eutectic mixture of ice and epsomite [Prieto-Balesteros and Kargel, 2005].

I_h.

9.3.3 Thermal conductivity of ammonia

Some authors considered the ammonia as a contaminant for planetary ices (Croft, et al., 1988), (Kargel, 1991), (Kargel, et al., 1991), (Kargel, 1992), (Hogenboom, et al., 1997), (Ross, et al., 1998). As shown in section 4.5, ammonia phases could be present also in the ices of Europa and Ganymede. Moreover, the presence of NH_3 significantly lowers the melting point of the ice favouring the presence of a liquid ocean beneath the icy crust of the satellites.

In *Figure LXXVIII* is reported the thermal conductivity of solid ammonia measured by (Krupskii, et al., 1968) in the temperature range useful for Galilean satellites. Such results are in agreement with preliminary measurements of $NH_3 \cdot 2H_2O$ performed by (Kargel, 1990), and with thermal conductivity measurements performed by other authors (Shandera, et al., 2000), (Lorenz, et al., 2001) on 10-30% aqueous ammonia-rich ice.

Unfortunately, there are no measurements of the thermal conductivity of ammonia at higher temperatures. Even if the thermal conductivity of ammonia at low temperature is pretty similar to that of ice I_h , its value have to be considered in a model of ice containing a certain percentage of NH_3 .

9.3.4 Thermal conductivity of dust

Some authors (Chyba, et al., 1998), (Moore, et al., 2000)] as reported in previous section) considered a certain percentage of lunar dust as a contaminant in the European ice. (Fountain, et al., 1970) performed measurements of the thermal conductivity of particulate basalt samples in a temperature range of (150-270) K and a pressure of 10^{-6} Pa in order to simulate the lunar soil conditions. The authors noted that the experimental results were fitted by the function $k(T) = A + BT^3$ (see *Figure LXXVIII*) obtained experimentally by (Watson, 1964) for silicate powders in vacuum. The results show a value of $\sim 10^{-3} \text{ W m}^{-1} \text{ K}^{-1}$ and are in agreement with measurements of the thermal conductivity of lunar surface samples performed by other authors (Birkebak, et al., 1970) (Cremers, et al., 1970) even if there is the evidence of higher values of thermal conductivity at depths of some tens of centimeters (Keihm, et al., 1973), (Langseth, et al., 1976).

Since the thermal conductivity of lunar regolith is almost three orders of magnitude lower than that of ice I_h , care must be taken if a mix of the two materials is considered: the lunar powder could act as an insulator, giving rise to higher temperatures inside the dirty-ice crust encouraging the presence of brines at lower depths.

9.3.5 Thermal conductivity of carbon dioxide

The carbon dioxide is usually considered as present inside planetary ices, especially in the polar caps of Mars (Ross, et al., 1998).

(Kravchenko, et al., 1986) performed a measurement of the thermal conductivity of solid CO_2 in the temperature range (145-210) K. The

authors evidenced that the temperature dependence of the thermal conductivity of solid carbon dioxide was $k(T) = 93.4/T$ (reported in *Figure LXXVIII*), similar to the ice I_h. The results were also in agreement with measurements performed by (Konstantinov, et al., 1988) in a similar temperature range.

X. CONCLUSIONS

The main goal of this dissertation is the electromagnetic characterization of Europa's and Martian analogues for estimating the performance of the radar sounders used to investigate the subsoils.

It has provided an intense laboratory work aimed at evaluating the effects of scattering and the electromagnetic properties of ice mixtures, simulating the subsurface of Mars and Europa, on the attenuation of the radar signal (Pettinelli et al.). Such a study is critical for the determination of specific RIME and to determine its performance in terms of maximum penetration depth, spatial resolution, and detection capability of interfaces to weak electromagnetic contrast.

The results reported in this work highlight the importance of the laboratory experiments to properly characterize solid (mineral) impurities on the ice electromagnetic behavior.

In fact the dielectric properties of ice/soil (or rock) mixtures at temperatures typical of Martian surface underline that at very low temperatures, the icy mixtures can sometime exhibit unexpected behaviours which, in the frequency band typical of the subsurface penetrating radars, deviate from the properties of pure water ice.

Our measurements show that, besides the expected dependence of the attenuation from temperature, the presence in the ice of the solid inclusions (mineral grains) strongly affects the behaviour of the attenuation versus frequency.

CONCLUSIONS

In particular, I found that at low frequency and high temperature the behaviour of the pure ice dominates and the attenuation is approximately constant, whereas at high frequency and low temperature the behaviour of the basalt matrix dominates and the attenuation linearly increases with frequency as shown in this figure:

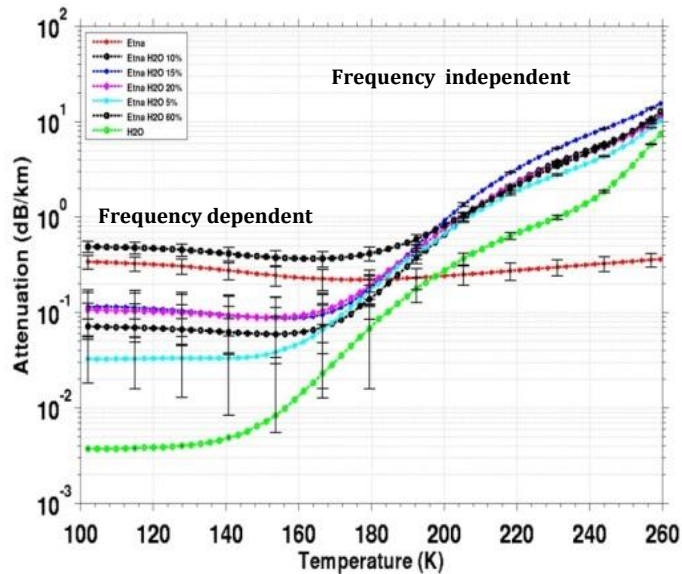


Figure LXXIX Comparison between measurements of attenuation performed on the different ice/basalt sand mixture with the HP4285A LCR meter (75kHz-30MHz) and the asymptotic curve calculated using equation (LIII).

On the other hand the saline-ice electromagnetic behaviour has underlined that:

- real and imaginary part of permittivity decreases as the temperature decreases;
- real and imaginary part increases as the amount of salt therefore the losses become lower and lower with temperature drops;
- the attenuation coefficient becomes very small as the temperature decreases so the penetration of the radar signal is possible since the salts like impurities in ice don't influence so

CONCLUSIONS

much the conductivity and consequently the attenuation as shown in the following picture.

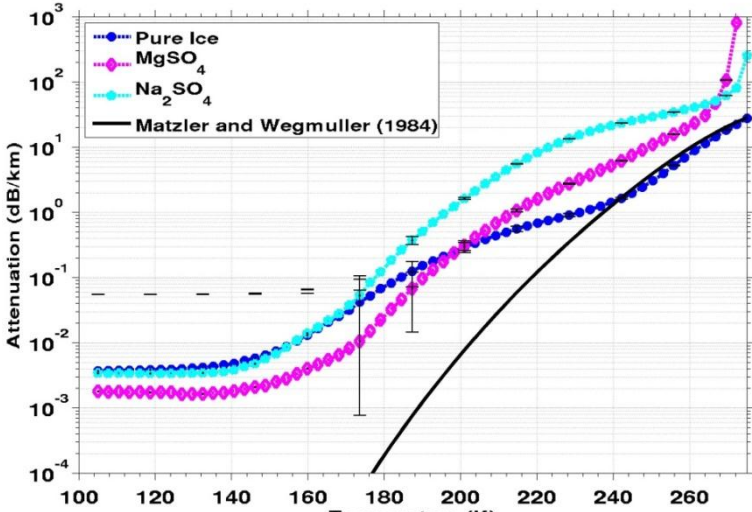


Figure LXXX Comparison between measurements of attenuation performed on the different saline ices mixture with the HP4285A LCR meter (75kHz-30MHz) and the asymptotic curve calculated using equation of Matzler and Wegmuller (1984).

XI. FUTURE WORKS

Since some acids (like Sulphuric and Hydrochloric acid) play an important role in the conduction mechanisms of the ice, object of future research will be the study of the dielectric properties of ice mixtures containing such type of impurities.

In addition a possible future work is a project will perform simultaneous measurements of the icy materials reproducing the physical-chemical and compositional properties of different Solar System icy surfaces, with the aim of characterizing the studied materials in different regions of the electromagnetic spectrum (VIS-IR and HF bands, respectively).

To our knowledge, such proposed combined measurements are unique considering the range of temperatures and type of investigated materials.

This approach will minimize the intrinsic uncertainty caused by spatial heterogeneity in different samples. At this setup we plan to couple a spectroscopic system aimed to characterize the surface composition of the icy sample placed in the same capacitive cell as shown in the following figure.

The data analyses of present or future large planetary missions, which will foresee the use of both reflectance spectroscopy and subsurface radar, will take full advantage from the results of the proposed combined laboratory measurements.

Indeed these measurements will provide complementary constraints useful to determine the nature of the subsurface icy materials.

FUTURE WORKS

The novelty of the project resides in the possibility to create a large database of VIS-IR and dielectric spectra of peculiar ices, whose properties are measured simultaneously on the same sample. From such database, the propagation parameters in the frequency range of HF radar will be also calculated.

Among non-ice materials to be measured, relevant for the composition of real planetary surfaces and available from the market, we plan to use: phyllosilicate and clay minerals, carbon dioxide, ammonia, hydrated salt minerals, and some organics miscible with water.

Each measurement will refer to a mixture of one of the above compounds with water in different concentrations. One measurement run will take approximately 18 hours, needed to cool the sample down to ~ 100 K and take measurements during the ascending phase of the temperature cycle.

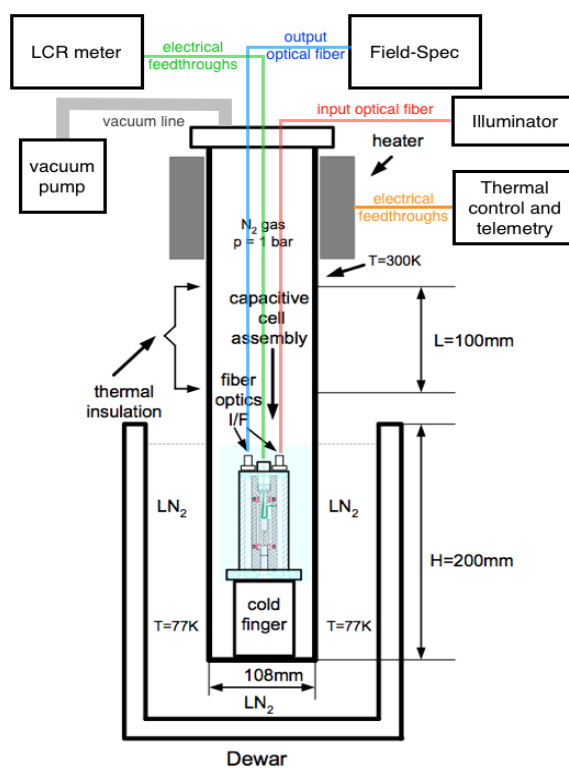


Figure LXXXI Scheme of implemented experimental setup

FUTURE WORKS

Finally more interesting is the development the thermal model of Europa's ice shell. In particular it's necessary to understand how the radar signal is influenced by variations of thermal conductivity inside ice shell. Consequently knowing the thermal profiles of different scenarios, it's possible to simulate the radar signal and so verify the detectability of the liquid ocean as reported in the following figures where I simulated the propagation of a plane wave in a crust of pure ice overlaying a liquid ocean, in the circle line of Figure LXXXIII is underlined the reflection from the ice/ocean interface that is located at the depth of 10 km.

I imposed a 2 % of randomic fluctuation of real permittivity which produces a noise level in the radargram see Panel b) of Figure LXXXIII. The temperature of the icy crust is shown in the panel a) of Figure LXXXIII.

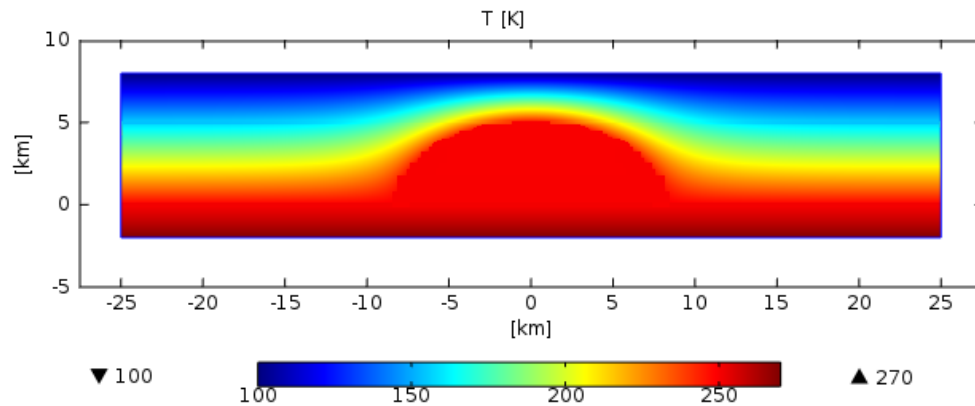


Figure LXXXII Example of temperature's distribution in Europa's plume in a thickness of 10 km

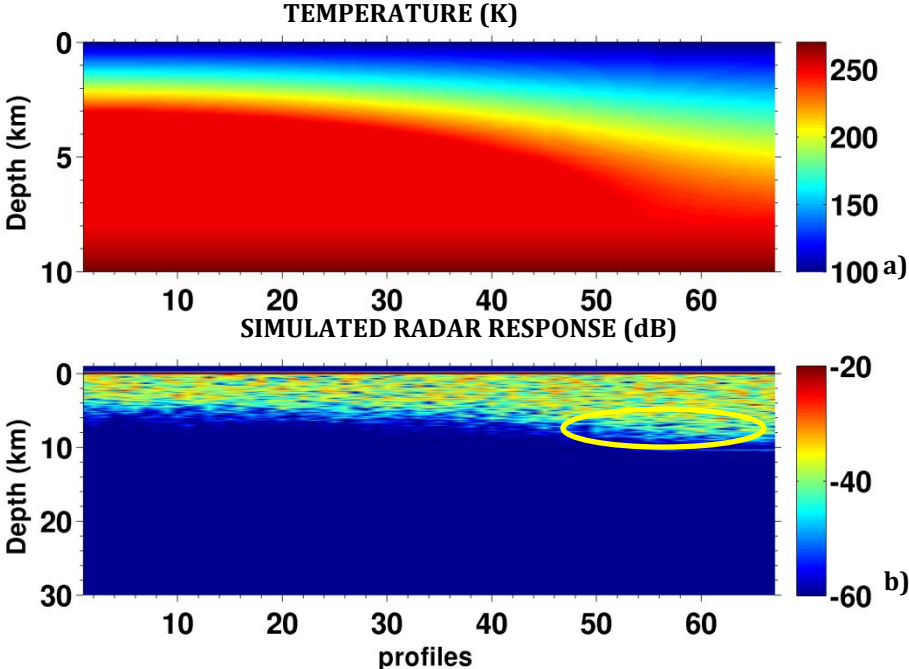


Figure LXXXIII a) Temperature's distribution, b) Simulated Radargram; in the circle line is underlined the reflection from the ice/ocean interface that is located at the depth of 10 km.

BIBLIOGRAPHY

- Anderson J. D. and G. Schubert, R. A. Jacobson, E. L. Lau, W. B. Moo** Europa's differentiated internal structure: Inferences from four Galileo encounters : Science, 1998.
- Andersson and Suga H** Thermal conductivity of low-density amorphous ice: Solid State Communications, 1994.
- Andersson P and Backstrom R G Ross and G** Thermal resistivity of ice Ih near the melting point : J. Phys. C: Solid State Phys., 1980.
- Arvidson and et al.** Three mars years: Viking lander 1 imaging observations: Science, 1983. - Vol. 22.
- Auty Robert P. and Cole Robert H.** Dielectric Properties of Ice and Solid D₂O: The Journal of Chemical Physics, 1952. - Vol. 20.
- Barnes and P. R. F., Wolff, E. W., Mulvaney, R., Udisti, R.** Effect of density on electrical conductivity of chemically laden polar ice.: Journal of geophysical research, 2002.
- Barr A.C. and Showman A.P.** Heat transfer in Europa's ice shell. - 2009.
- Barr and T. Pappalardo R.** Onset of convection in the icy Galilean satellites: Influence of rheology: J. Geophys. Res, 2005.
- Basu et al.** Simulation of the martian dust cycle with gfdl mars gcm.: J. Geophys.Res, 2004. - Vol. 109.
- Bibring J.P. and et al** Perennial water ice identified in the south polar cap of Mars: Nature, 2004.
- Bierhaus and et al** Europa .
- Birkebak and C. J. Cremers, and J.P. Dawson** Thermal radiation properties and thermal conductivity of lunar materials: Science, 1970.
- Bjerrum** Structure and properties of ice : Science, 1952. - 385-390 : Vol. 115.2989 .
- Bland and Showman** - 2007.
- Boynton W [et al.]** Distribution of hydrogen in the near surface of Mars: Evidence for subsurface ice deposits : Science, 2002. - 81-85 : Vol. 297.
- Calvin W. M. and Titus, T. N.** Summer season variability of the North residual cap of Mars MGS-TES: In 35th Lunar and Planetary Science Conference, 2004. - 1455.
- Camplin and J. W. Glen J . G. Parch** Theoretical models for interpreting dielectric behaviour of HF-doped ice : J.Glaciology, 1978.

- Camplin G. C., J. W. Glen and J. G. Paren** Theoretical models for interpreting the dielectric behavior of HF-doped ice : J. Glaciol., 1978. - Vol. 21.
- Cantor B. A. [et al.]** Recession of martian north polar cap: 1990-1997 Hubble Space Telescope observations : Icarus, 1998. - 136:175-191.
- Cantor, Bruce, A. and James, P. B.** Interannual variability of the martian residual north polar cap : In 32nd Lunar and Planetary Science Conference, # 1951., 2001.
- Carr M. H** Water on Mars. : Oxford University Press, 1996.
- Carr M. H and M. J. S. Belton, C. R. Chapman, M. E. Davies, P** Evidence for a subsurface ocean on Europa : Nature, 1998.
- Carter L.M. and et al.;** Dielectric properties of lava flows west of Ascraeus Mons, Mars: Geophys. Res. Lett, 2009.
- Cereti A. and Vannaroni, G., Vento, D., Pettinelli, E.** Electromagnetic measurements on martian soil analogs: Implications for MARSIS and SHARAD radars in detecting subsoil water. Planet. Space Sci., 2007.
- Chelidze T. L. and Gueguen Y.,** Electrical spectroscopy of porous rocks: a review-I. : Geophys. J. Int., 1999.
- Chizov** - 1993.
- Chyba** - 2000.
- Chyba and C. F., Ostro, S. J., & Edwards, B. C.** Radar detectability of a subsurface ocean on Europa : Icarus, 1998.
- Chyba and Phillips** - 2001.
- Chyba C.F. and Ostro, S.J., Edwards, B.C.,** Radar detectability of a subsurface ocean on Europa. : Icarus, 1998.
- Clifford and et al.** The state and future of mars polar science and exploration : Icarus. - 144 : Vol. 2000.
- Clifford S.M. and Lasue J., Heggy, E., Boisson, J., McGovern, P.** Depth of the martian cryosphere: Revised estimates and implications for the existence and detection of subpermafrost groundwater : J. Geophys. Res., 2010.
- Cooper and et al** - 2001.
- Crary and Bagenal** - 1998.
- Cremers and C.J., Birkebak, R.C., Dawson, J.P., .** Thermal conductivity of fines from Apollo 11. : Proc. Apollo 11 Lunar Sci. Conf., 1970.
- Croft and J.I. Lunine, J. Kargel** Equation of state of ammonia-water liquid – Derivation and planetological applications : Icarus, 1988.
- Debye and Peter Josef William** Polar molecules. - New York: Dover : [s.n.], 1929. - Vol. Vol. 172.
- Deschamps and Sotin** Thermal convection in the outer shell of large icy satellites : Journal of Geophysical Research, 2001.
- Dillard and Timmerhaus** Low temperature thermal conductivity of solidified H₂O and D₂O : Pure and Applied Cryogenics, 1966.
- Durham and al et** Rheological and Thermal Properties of Icy Materials : Space Science Reviews, 2010.

- Durham and L.A. Stern T. Kubo, S.H. Kirby** Flow strength of highly hydrated Mg- and Na-sulfate hydrate salts, pure and in mixtures with water ice, with application to Europa : J. Geophys. Res.
- Edgett K. and M. Malin** New views of mars eolian activity, materials, and surface properties: three vignettes from the mars global surveyor orbiter camera : J. Geophys. Res, 2000. - Vol. 105.
- El-Said and M.A.H** Geophysical Prospection of Underground Water in the Desert by Means of Electromagnetic Interference Fringes : IEEE, 1956.
- Fanale and et al.** Global distribution and migration of subsurface ice on mars : Icarus, 1986. - Vol. 67.
- Feldman W. C. [et al.]** Global distribution of neutrons from Mars: Results from Mars Odyssey : Science, 2002. - 75-78 : Vol. 297.
- Feldman W. C. [et al.]** The global distribution of near-surface hydrogen on Mars. In Sixth International Conference on Mars - 2004. - 3218.
- Fischer and Spohn** - 1990.
- Fishbaugh K. and C. Hvidberg** Martian north polar layered deposits stratigraphy: Implications for accumulation rates and flow : J. Geophys. Res. - Vols. 111(E06012), doi: 10.1029/2005JE002,571.
- Fisher D.** If martian ice caps flow: ablation mechanisms and appearance : Icarus, 1993. - Vol. 105.
- Fisher D.** Internal layers in an "accublation" ice cap: a test for flow : Icarus,, 2000. - Vol. 144.
- Forget F. [et al.]** Improved general circulation models of the martian atmosphere from the surface to above 80 km : Journal of Geophysical Research, 1999. - Vol. 104(E10).
- Fountain James A. and Edward A. West.** Thermal conductivity of particulate basalt as a function of density in simulated lunar and Martian environments : Journal of Geophysical Research, 1970.
- Fujita S and Matsuoka T., Ishida, T., Matsuoka, K., Mae, S.** A summary of the complex dielectric permittivity of ice in the megahertz range and its applications for radar sounding of polar ice sheets : Physics of Ice Core Records, 2000.
- Gaidos and al. et** - 1999.
- Gierasch P. and R. Goody** The effect of dust on the temperature of the mars atmosphere : J. Atmos. Sci, 1972. - Vol. 29.
- Glenn J.W. and J.G.Paren, ,** The electrical Proprieties of snow and Ice : Journal of Glaciology, 1975.
- Golding [et al.]** Mechanical properties of the ice I–magnesium sulfate eutectic: A comparison with freshwater ice in reference to Europa : Icarus, 2013.
- Golombek** - 1982.
- Gränicher H. and et al** Dielectric relaxation and the electrical conductivity of ice crystals : Discussions of the Faraday Society, 1957. - 50-62 : Vol. 23.

- Greenberg** - 2009.
- Greenberg** - 1982.
- Greenberg** - 2005.
- Greenberg** - 2008.
- Greenberg** - 2005, 2008.
- Greenberg and Geissler** - 2002.
- Greenberg and Geissler** - 2002.
- Greenberg and Peale** - 1982, 1986.
- Greenberg R., Geissler P., Hoppa, G., Tufts, B.R., Durda, D.D, Pappalardo, R., Head, J.W., Greeley, R., Sullivan and Carr M.H** Tectonic processes on Europa: Tidal stresses, mechanical response, and visible features : Icarus, 1998.
- Greenberg** The icy Jovian satellites after the Galileo mission : Rep. Prog. Phys, 2010.
- Grima C. and Kofman, W., Mouginit, J., Phillips, R.J., Hérique** North polar deposits of Mars: Extreme purity of the water ice : Geophys. Res. Lett, 2009.
- Grima C. and , Kofman, W., Hérique, A., Orosei, R., Seu, R.,** Quantitative analysis of Mars surface radar reflectivity at 20 MHz : Icarus, 2012.
- Grimm R. E. and Stillman, D. E., Dec, S. F., & Bullock, M. A** Low-frequency electrical properties of polycrystalline saline ice and salt hydrates : The Journal of Physical Chemistry B, 2008.
- Gross and et al.** - 1971.
- Gross and G. W., HAYSLIP, I. C., & Hoy, R. N.** Electrical conductivity and relaxation in ice crystals with known impurity content : Journal of Glaciology, 1978.
- Gross and G. W., Wong, P. M., & Humes, K.** Concentration dependent solute redistribution at the ice-water phase boundary. III. Spontaneous convection. Chloride solutions. : The Journal of Chemical Physics, 1977.
- Gudmandsen P.** Electromagnetic probing of ice. In: Wait, J.R. (Ed.), Electromagnetic Probing in Geophysics. : Golem Press, 1971.
- Guéguen Y. and Victor P.** Introduction to the Physics of Rocks : Princeton, 1994.
- Haberle and et al.** Mars atmospheric dynamics as simulated by the nasa/ames general circulation model, 1. the zonal-mean circulation : JGR, 1993. - 13 : Vol. 102.
- Haberle R. ,** Interannual variability of global dust storms on mars, Science, 234 : Science, 1986. - Vol. 234.
- Håkansson and P. Andersson** Thermal conductivity and heat capacity of solid NaCl and NaI under pressure : J. Phys. Chem. Solids, 1986.
- Han and A. Showman** Thermo-compositional convection in Europa's icy shell with salinity. : Geophys. Res. Lett, 2005.
- Hand and et al** - 2007.

- Hand and Chyba** - 2007.
- Head and et al.** Recent ice ages on mars : Nature, 2003. - Vols. 426, 797.
- Hecht M.** Metastability of liquid water on mars : Icarus, 2002. - Vol. 156.
- Heggy and E.M. Palmer, W. Kofman, S. Clifford, K. Righter** Radar properties of comets: Parametric dielectric modeling of Comet 67P/Churyumov–Gerasimenko : Icarus, 2012.
- Heggy E. and Palmer, E.M., Kofman, W., Clifford, S., Righter** Radar properties of comets: Parametric dielectric modeling of Comet 67P/ : Icarus, 2012.
- Heldmann and et al.** Formation of martian gullies by the action of liquid water owing under current martian environmental conditions : JGR, 2005. - Vols. 110(E05004), doi:10.1029/2004JE002,261.
- Herique A and Gilchrist, J., Kofman, W., Klinger, J.** Dielectric properties of comet analog refractory materials. : Planet. Space Sci., 2002.
- Herique and A., J. Gilchrist, W. Kofman and J. Klinger** Dielectric properties of comet analog refractory materials : Planetary and Space Science, 2002.
- Herkenhoff** Evidence from opportunity's microscopic imager for water on meridiani planum : Science, 2004. - Vol. 306.
- Hindmarsch and et al.** Sublimation of ice through sediment in beacon valley, antartica : Geografiska Annaler, 1998. - Vol. 80.
- Hobbs** Ice Physics - New York : Oxford Univ. Press, 1974.
- Hogenboom and J.S. Kargel, G.J. Consolmagno, T.C. Holden, L. L** The ammoniawater system and the chemical differentiation of icy satellites : Icarus, 1997.
- Hoppa and et al** - 1999a,1999b.
- Hourdin F. [et al.]** Meteorological variability and the annual surface pressure cycle on Mars. : Journal of the Atmospheric Sciences, 1993. - 3625-3640 : Vol. 50(21).
- Howard A.** The role of eolian processes in forming surface features of the martian polar layered deposits : Icarus, 2000. - Vol. 144.
- Hurford** - 2005.
- Hussmann and Spohn** - 2004.
- Hussmann, Spohn T. and Wiczerkowski K.** Thermal equilibrium states of Europa's ice shell: Implications for internal ocean thickness and surface heat flow. : Icarus, 2002.
- Hvidberg C.** Water on Mars and Life : Springer-Verlag Berlin Heidelberg, 2005. - Vols. chap. 6, 1st ed.,.
- Hvidberg** Relationship between topography and flow in the north polar cap on mars : Annals of Gaciology, 2003. - Vol. 37.
- Jaccard C.** Etude theoretique et experimentale des proprietes electriques de la glace - 1959. - 32,89-128 : Vol. Helv. Phys. Acta.

- Jaccard C.**, Thermodynamics of irreversible processes applied to ice, : Phys. Kond. Mat., 1964.. - Vol. 3.
- Jaccard Claude** "Thermodynamics of irreversible processes applied to ice." : Physik der kondensierten Materie , 1964. - Vol. 3.2.
- Jakosky B. and M. Mellon** Water on mars : Phys. Today, 2004. - Vol. 71.
- Jakosky B. M. and Farmer, C. B.** The seasonal and global behavior of water vapor in the Mars atmosphere: Complete results of the Viking atmospheric water detector experiment : Journal of Geophysical Research. - 2999-3019. : Vol. 87(B4).
- James P. B. and Cantor, B. A.** Martian north polar cap recession: 2000 Mars Orbiter Camera Observations : Icarus, 2001. - 154:131-144.
- James P. B., Kieffer, H.H. and Paige, D.A.** The seasonal cycle of carbon dioxide on Mars : Mars, pages 934-968, The University of Arizona Press, 1992.
- Johari G. P. and P. A. Charette.** The permittivity and attenuation in polycrystalline and single-crystal ice Ih at 35 and 60 MHz : J. Glaciol, 1975.
- Johari G. P. and Edward Whalley** The dielectric properties of ice Ih in the range 272–133 K : The Journal of Chemical Physics, 1981. - 75.
- Johari Gyan P.** Glass transition and secondary relaxations in molecular liquids and crystals : Annals of the New York Academy of Sciences, 1976.
- Kahn R. A., Martin, T. Z. and Zurek, R. W.** The martian dust cycle : The University of Arizona Press, 1992.
- Kargel** Cryomagmatism in the Outer Solar System. - [s.l.]: Ph.D. dissertation, 309 pp., University of Arizona, 1990.
- Kargel** Ammonia-water volcanism on icy satellites: phase relations at 1 atmosphere : Icarus , 1992.
- Kargel and S.K. Croft, J.I. Lunine, J.S. Lewis** Rheological properties of ammonia-water liquids and crystal- liquid slurries—Planetological applications. : Icarus, 1991.
- Kargel** Brine volcanism and the interior structures of asteroids and icy satellites : Icarus, 1991.
- Kawada and Tutiya, R.** Dielectric properties and annealing effects of as-grown KOH-highly doped ice single crystals. : Journal of Physics and Chemistry of Solids, 1997.
- Keating et al. G. (1998)**, The structure of the upper atmosphere of mars: In situ accelerometer measurements from mars global surveyor : Science, 1998. - Vol. 279.
- Keihm and Langseth, M.G., .** Surface brightness temperatures at Apollo 17 heat flow site: Thermal conductivity of the upper 15 cm of regolith. : Proc. 4th Lunar Sci. Conf., 1973.
- Khurana and et al** - 1998.

- Khurana K. K. and , M. G Kivelson, D. J. Stevenson, G. Schubert, C.** Oceans in Europa and Callisto: Independent evidence from magnetic perturbations. : Nature, 1998.
- Kieffer and et al** : Mars, University of Arizona Press, Tucson, Arizona, 1992.
- Kirkup L. and Frenkel, R.B.** An Introduction to Uncertainty in Measurement: Using the GUM (Guide to the Expression of Uncertainty in Measurement). : Cambridge University Press, 2006.
- Kivelson and et al** - 2002.
- Kivelson and et al** - 2000.
- Klinger** Influence of a phase transition of ice on the heat and mass balance of comets : Science, 1980.
- Konstantinov and Manzhelii V.G. Smirnov S.A., Tolkachev A.M.** Heat transfer in solid CO₂ and N₂O: dependence on temperature and volume : Sov. J. Temp. Phys., 1988.
- Kravchenko Y.G. and Krupskii, I.N., .** Thermal conductivity of solid N₂O and CO₂ : Soc. J. Low Temp. Phys, 1986.
- Krupskii and V. G. Manzhelii, and L. A. Koloskova,** Thermal Conductivity of Solid Ammonia : Phys. Status Solidi, 1968.
- Kuiper G. P.** Infrared Observations of Planets and Satellites : AJ, 1957.
- Kulesa and Bernd** A critical review of the low-frequency electrical properties of ice sheets and glaciers : Journal of Environmental & Engineering Geophysics, 2007.
- Kuskov and Kronrod, V.A** Internal structure of Europa and Callisto. - 2005.
- Lainey and et al.** - 2009.
- Langseth and M.G. Keihm S.J., Peters, K.,** Revised lunar heat-flow values. : Proc. Lunar Sci. Conf, 1976.
- Larsen J. and Dahl-Jensen, D.** Interior temperatures of the northern polar cap on Mars : Icarus, 2000.
- Laskar and et al.** Orbital forcing of the martian polar layered deposits : Nature, 2002. - Vol. 419.
- Lauro S.E. and et al.** Permittivity estimation of layers beneath the northern polar layered deposits, Mars : Geophys. Res. Lett, 2010.
- Lauro S.E.** Dielectric constant estimation of the uppermost Basal Unit layer in the martian Boreales Scopuli region : Icarus, 2012.
- Leighton R. B and B. C. Murray** Behavior of carbon dioxide and other volatiles on mars : Science, 1966. - Vol. 153.
- Leovy and et al.** Mechanisms of mars dust storms : J. Atmos. Sci., 1973. - 74 : Vol. 30.
- Leovy C** Weather and climate on mars : Nature, 2001. - Vol. 412.
- Li J. and Andrews-Hanna, J.C., Sun, Y., Zuber, M.T., Phil** Density variations within the south polar layered deposits of Mars : J. Geophys. Res., 2010.
- Lorenz and Shandera .** - 2001.

- MacGregor J.A. and Winebrenner, D.P., Conway, H., Matsuoka, K., Maye** Modeling englacial radar attenuation at Siple Dome, West Antarctica, using ice chemistry and temperature data : J. Geophys. Res., 2007.
- Malin and et al** Present day impact cratering and contemporary gully activity on mars : Science, 2006. - Vol. 10.1126.
- Marchis and et al** - 2005.
- MARSIS and Picardi et al. 2005, Jordan et al., 2009**
- Matson and et al.** - 2001.
- Matsuoka** Dielectric properties of freshwater ice at microwave frequencies : iopscience, 1996.
- Mattei E. and , et al.** Dielectric measurements and radar attenuation estimation of ice/basalt sand mixtures as martian Polar Caps analogues : Icarus, 2013.
- Matzler and Wegmuller** Dielectric properties of freshwater ice at microwave frequencies : iop.science, 1987.
- McCarthy and S.S Ballard** Thermal conductivity of eight halide crystals in the temperature range 220 °K to 390 °K : Journal of applied Physics, 1960.
- McCarthy C. and R.F. Cooper S.H. Kirby, K.D. Rieck, L.A. Stern C.** McCarthySolidification and microstructures of binary ice-I/hydrate eutectic aggregates : Am. Mineral, 2007.
- McCollom** - 1999.
- McCollom 1999 Zolotov and Shock 2003, 2004**
- McKinnon and E.M Parmentier** Ganymede and Callisto. - 1986.
- McKinnon** On convection in ice I shells of outer solar system bodies, with specific application to Callisto : Icarus, 2006.
- McKinnon W.B.,** Convective instability in Europa's floating ice shell : Geophys. Res. Lett. , 1999.
- Mellon M. and R. Phillips** Recent gullies on mars and the source of liquid water : J.Geophys. Res., 2004. - 23 : Vol. 106.
- Mitri and et al.** Mountains on Titan: Modeling and observations. : J. Geophys. Res., 2010.
- Mitri and P. Showman A.** Convective-conductive transitions and sensitivity of a convecting ice shell to perturbations in heat flux and tidal-heating rate: Implications for Europa. : Icarus, 2005.
- Mitri and P. Showman A.** Thermal convection in ice-I shells of Titan and Enceladus : Icarus, 2008.
- Mitrofanov I. [et al.]** CO₂ snow depth and subsurface water-ice abundance in the northern hemisphere of Mars : Science, 2003. - 2081-2084 : Vol. 300.
- Mitrofanov I. [et al.]** Maps of subsurface hydrogen from the High Energy Neutron Detector, Mars Odyssey : Science, 2002. - 78-81 : Vol. 297.

BIBLIOGRAPHY

- Mitrofanov I.** Maps of subsurface hydrogen from the high-energy neutron detector, Mars Odyssey. : Science, 2002.
- Montabone and et al.** Interannual variability of martian dust storms in assimilation of several years of mars global surveyor observations : Adv. Space Res, 2005. - Vols. 36,.
- Moore** - 2003.
- Moore** Soil-like deposits observed by sojourner, the pathfinder rover, : J.Geophys. Res., 1999. - Vol. 104.
- Moore and et all** - 1999.
- Moore and Hussmann** - 2009.
- Moore and Schubert** Models of radar absorption in European ice : Icarus, 2000.
- Moore** Electrical response of the Summit-Greenland ice core to ammoniums, sulphuric acid, and hydrochloric acid : Geophysical Research Letters, 1994.
- Moore** Thermal equilibrium in Europa's ice shell. Icarus : Icarus, 2006.
- Moresi and Solomatov** Numerical investigation of 2D convection with extremely large viscosity variations : Phys. Fluids, 1995.
- Mouginot J and et al.** The 3–5 MHz global reflectivity map of Mars by MARSIS/ Mars Express: Implications for the current inventory of subsurface H₂O : Icarus, 2010.
- Mouginot J and Pommerol, A., Beck, P., Kofman, W., Clifford, S** Dielectric map of the martian northern hemisphere and the nature of plain filling materials. : Geophys. Res. Lett, 2012..
- Murray and et al.** Geological framework of the south polar region of mars : Icarus, 1972. - Vol. 17.
- Mustard and et. al** Evidence for recent climate change on mars from the identification of youthful near-surface ground ice. : Nature, 2001. - Vol. 412.
- Nagle J. F.** Statistical mechanics of the melting transition in lattice models of polymers : Proceedings of the Royal Society of London. A. Mathematical and Physical Sciences, 1974. - 1611 : Vol. 337.
- Nimmo and Manga M** Causes, characteristics, and consequences of convective diapirism on Europa. : Geophys. Res. Lett, 2002.
- Nimmo, Pappalardo, R.T. and Giese, B.,** Estimates of Europa's ice shell thickness from elastically-supported topography : GEOPHYSICAL RESEARCH LETTERS, 2003.
- Nunes D.C., Phillips, R.J.** Radar subsurface mapping of the polar layered deposits on Mars : J. Geophys. Res., 2006.
- Nye J. F. [et al.]** The instability of a south polar cap on Mars composed of carbon dioxide. : Icarus, 2000.
- O'Brien, et al and Geissler, P., Greenberg, R.,** A melt-through model for chaos formation on Europa : Icarus, 2002.
- Oberst and et al** - 1999.
- Ojakangas and Stevenson** - 1986.

- Ojakangas and D. Stevenson** Thermal state of an ice shell on Europa : Icarus, 1989.
- Onsager L. and Dupuis M** The electrical properties of ice : Rendiconti della Scuola Internazionale di Fisica "Enrico Fermi," 1960.
- Oswald and Gongineni** Recovery of subglacial water extent from Greenland radar survey data - 2008. - Number 184 : Vols. Volume 54, January 2008 , pp. 94-106(13).
- Pankine A. and , and A. Ingersoll** Interannual variability of mars global dust storms: An example of self-organized criticality : J. Geophys. Res, 1999. - Vol. 104.
- Pappalardo and A. Barr** The origin of domes paon Europa: The role of thermally induced compositional diapirism : Geophys. Res. Lett., 2004.
- Pappalardo and et al** - 2004.
- Pappalardo R.T. and Head, J.W., Greeley, R., Sullivan, R.J., Pilcher** Geological evidence for solid- state convection in Europa's ice shell. : Nature, 1998.
- Paren G. and Robin G. de Q.** Internal reflections in polar ice sheets : Journal of Glaciology, 1975. - 71 : Vol. 14.
- Peale** - 1986.
- Peale and et al.** - 1979.
- Petit J.R. and et al** Climate and atmospheric history of the past 420,000 years from the Vostok ice core, Antarctica : Nature, 1999.
- Petrenko V.F** On the nature of electrical polarization of materials caused by cracks. Application to ice electromagnetic emission : Phil. Mag. B, 1993.
- Petrenko Victor F. and Whitworth. Robert W.** Physics of ice : Oxford University Press, 1999.
- Pettinelli et al. 2007**
- Phillips R.J. and et al.** Mars north polar deposits: Stratigraphy, age, and geodynamical response. : Science, 2008.
- Picardi et al. 2005, Seu et al. 2007 and Ono et al. 2008**
- Picardi et al. 2005, Seu et al. 2007 and Ono et al. 2008**
- Picardi et al. 2005, Seu et al. 2007 and Ono et al. 2008**
- Picardi G. and et al.** Performance and surface scattering models for the Mars Advanced Radar for Subsurface and Ionosphere Sounding (MARSIS). : Planet.Space Sci, 2004.
- Picardi G., Masdea, A., Piccari, F., Seu, R.** Marsis Inversion Approach : Geophys, 2008.
- Plaut J.J. and et al.** Subsurface radar sounding of the south polar layered deposits of Mars : Science, 2007.
- Plaut J.J. and et al.** Subsurface radar sounding of the south polar layered deposits of Mars : Science, 2007.
- Pollack et al. H.** Properties and effects of dust particles suspended in the martian atmosphere : J. Geophys. Res., 1979. - Vol. 84.

- Prieto-Ballesteros and J.S. Kargel** Thermal state and complex geology of a heterogeneous salty crust of Jupiter's satellite Europa : Icarus, 2005.
- Ratcliffe** The thermal conductivity of ice: new data on the temperature coefficient : Philosophical Magazine , 1962.
- Ross and Anderson P and Backstrom G** Effects of H and D order on the thermal conductivity of ice phases : J. Chem. Phys, 1978.
- Ross, P Anderson and G Backstrom** High Temp. High Pressures - 1977.
- Ross. and Kargel J.S.** Thermal conductivity of Solar System ices, with special reference to martian polar caps - 1998.
- Rudolph and Manga M.** Effects of anisotropic viscosity and texture development of convection in Ice Ih mantles : Journal of Geophysical Research, 2012.
- Ruff S. and P. Christensen** Bright and dark regions on mars: Particle size and mineralogical characteristics based on thermal emission spectrometer data : J. Geophys.Res, 2002. - Vol. 107(E12).
- Rust A.C. and Russell J.K., Knight, R.J.** Dielectric constant as a predictor of porosity in dry volcanic rocks : J. Volcanol. Geoth. Res. , 1999.
- Schenk and et al** - 2001.
- Schilling and et al** - 2004.
- Schorghofer N.** A physical mechanism for long-term survival of ground ice in beacon valley, antarctica : Geophys. Res. Lett, 2005. - Vol. 32.
- Schubert and et al** - 2004.
- Segatz and et al** - 1988;.
- Segatz and et al.** - 1988.
- Seu R. and et al.** SHARAD: The MRO 2005 shallow radar. : Planet. Space Sci., 2004..
- Seufert M. and J. Saur F.M. Neubauer** Multi-frequency electromagnetic sounding of the Galilean moons : Icarus, 2011.
- Shandera and Lorenz .** - 2000.
- SHARAD and Seu et al.** 2007
- Shock** - 2003.
- Shoemaker and et al** - 1982.
- Showman and et all** - 2004.
- Showman and Malhotra** - 1997.
- Slack** Thermal conductivity of ice : Phys. Rev., 1980.
- Smith B.A [et al.]** "The Jupiter system through the eyes of Voyager 1" : Science, 1979a.
- Smith BA Soderblom LA, Beebe R, Boyce J, Briggs G, Carr M, Collins SA, Cook AF 2nd, Danielson GE, Davies ME, Hunt GE, Ingersoll A, Johnson TV, Masursky H, McCauley J, Morrison D, Owen T, Sagan C, Shoemaker EM, Strom R, Suomi VE, Veverka J** "The Galilean Satellites and Jupiter: Voyager 2 Imaging Science Results" : Science, 1979b.

- Smith M.** Interannual variability in tes atmospheric observations of mars during - 2004. - 167 : Vol. Icarus.
- Smith** Thermal emission spectrometer results: Mars atmospheric thermal structure and aerosol distribution : J. Geophys. Res., 2001. - Vol. 106.
- Solomatov V.S. and Moresi, L.N.** Scaling of time-dependent stagnant lid convection: Application to small-scale convection on Earth and other terrestrial planets. : J. Geophys. Res., 2000.
- Solomatov V.S.** Scaling of temperature- and stress-dependent viscosity convection. : Phys. Fluids , 1995.
- Sotin and et al** - 1998.
- Sotin and Head J. W. and Tobie G.** Europa: Tidal heating of upwelling thermal plumes and the origin of lenticulae and chaos melting : Geophys. Res. Lett., 2002.
- Sotin and Tobie G.** Internal structure and dynamics of the large icy satellites, C. R. Physique, - 2004.
- Spohn and and Schubert** - 2003.
- Spohn and Breuer D.** Implications from Galileo observations on the interior structure and evolution of the Galilean satellites : , in: Celnikier, L.M., Tran Tanh Van, J. (Eds.), Planetary Systems: The Long View, Editions Frontieres, Gif sur-Yvette, F, 1998.
- Spohn and Schubert G.** Oceans in the icy Galilean satellites of Jupiter? : Icarus, 2003.
- Squyres and et al** - 1983.
- Steiner and Kömle** A model of the thermal conductivity of porous water ice at low gas pressures : Planet. Space Sci, 1991.
- Stewart S.T. and Nimmo F.** Surface runoff features on mars: Testing the carbon dioxide formation hypothesis : JGR, 2002. - Vols. 107(E9), doi:10.1029/2000JE001,465.
- Stillman** - 2013b.
- Stillman D.E. and Grimm R.E., Dec, S.F.** Low-frequency electrical properties of ice–silicate mixtures : J. Phys. Chem, 2010.
- Sugden and et al** Preservation of miocene glacier ice in east antarctica : Nature, 1995. - Vol. 376.
- Takei I. and N. Maeno.** Electric characteristics of point defects in HCl-doped ice : Le Journal de Physique Colloques, 1987.
- Tanaka K.L. and et al.** North polar region of Mars: Advances in stratigraphy structure and erosional modification : Icarus, 2008.
- Thomas et al. P. C.** North-south geological differences between the residual polar caps on mars : Nature, 2000. - Vol. 404.
- Titus et al. T. N.** Exposed water ice discovered near the south pole of mars : Science, 2003. - Vol. 299.
- Tobie and Choblet G. and Sotin C** Tidally heated convection: Constraints on Europa's ice shell thickness. : J. Geophys. Res., 2003.

BIBLIOGRAPHY

- Tobie and Choblet G., and Sotin C.** Tidally heated convection: Constraints on Europa's ice shell thickness. : J.Geophys. Res., 2003.
- Toon and et al.** The astronomical theory of climatic change on mars, : Icarus, 1980. - Vol. 44.
- Ulaby F.T. and Moore, R.K., Fung, A.K.;** Microwave remote sensing. Active and passive : Artech House,, 1986. - Vols. Vol. 1. Fundamentals an Radiometry. Norwood, MA..
- Vant and et al** - 1974.
- Vasavada et al.** A Surface properties of mars's polar layered deposits and polar landing sites : J. Geophys. Res, 2000. - Vol. 105.
- Veeder and al. et** - 1994,2004.
- Von Hippel Arthur Robert, and Arthur R. Hippel** Dielectrics and waves - Wiley : [s.n.], 1954.
- Watson K.** The thermal conductivity measurements of selected silicate powders in vacuum from 150 °-350 °K . - [s.l.] : Ph, D. thesis, 1964.
- Whitman W. G.** : Am. J. Sci, 1926. - 126 : Vol. 11.
- Wolff and J. G. Paren** A two-phase model of electrical conduction in polar ice sheet : Journal of Geophysical Research, 1984. - Vol. Solid Earth.
- Wolff and W.O. Miners J.e. Moore** : J Phys. Chem, 1997.
- Wolff** Electrical response of the Summit-Greenland ice core to ammoniums, sulphuric acid, and hydrochloric acid : Geophysical Research Letters, 1994.
- Wolff** Electrical stratigraphy of polar ice cores: principle, methods, and findings : British Antarctic Survey, 2000.
- Yoder and Sjogren** - 1996.
- Zahnle and et al** - 2003.
- Zhang Z. and , Hagfors, T., Nielsen, E., Picardi, G., Mesdea, A** Dielectric properties of the martian south polar layered deposits: MARSIS data inversion using Bayesian inference and genetic algorithm : J. Geophys. Res., 2008.
- Zimmer and et al** - 2000.
- Zolotov and Shock** - 2003 2004.
- Zuber M. T., Smith, D. E. and Abshire, J. B.** - 1998.
- Zuber M.T. and et al** Density of Mars' south polar layered deposits. : Science, 2007.
- Zurek R. W. [et al.]** Dynamics of the atmosphere of Mars : The University Arizona Press, 1992.